DISCLAIMER

Final Technical Report (FTR)

Cover Page

a. *Federal Agency*	Department of Energy	
b. *Award Number*	DE-EE0009514	
c. *Project Title*	Interface Engineering using Vapor Transport Deposited Perovskite Films for Solar Cells	
d. *Recipient Organization*	University of Minnesota	
e. *Project Period*	*Start:* 8/1/21	*End:* 1/31/25
f. *Principal Investigator (PI)*	Name Russell Holmes Title Professor Email address rholmes@umn.edu Phone number 612-624-9058	
g. *Business Contact (BC)*	Name Victoria Troxler Title Senior Grants and Contracts Officer Email address vtroxler@umn.edu Phone number 612-624-9567	
h. *Certifying Official (if different from the PI or BC)*	Name Title Email address Phone number	

Russell Holmes _____ *3/11/25*

Signature of Certifying Official *Date*

By signing this report, I certify to the best of my knowledge and belief that the report is true, complete, and accurate. I am aware that any false, fictitious, or fraudulent information, misrepresentations, half-truths, or the omission of any material fact, may subject me to criminal, civil or administrative penalties for fraud, false statements, false claims or otherwise. (U.S. Code Title 18, Section 1001, Section 287 and Title 31, Sections 3729-3730). I further understand and agree that the information contained in this report are material to Federal agency's funding decisions and I have any ongoing responsibility to promptly update the report within the time frames stated in the terms and conditions of the above referenced Award, to ensure that my responses remain accurate and complete.

1. **Acknowledgement:** "This material is based upon work supported by the U.S. Department of Energy's Office of Energy Efficiency and Renewable Energy (EERE) Solar Energy Technologies Office (SETO) under the DE-FOA-0002357 Award Number(s) DE-EE0009514"

2. **Disclaimer:** “This report was prepared as an account of work sponsored by an agency of the United States Government. Neither the United States Government nor any agency thereof, nor any of their employees, makes any warranty, express or implied, or assumes any legal liability or responsibility for the accuracy, completeness, or usefulness of any information, apparatus, product, or process disclosed, or represents that its use would not infringe privately owned rights. Reference herein to any specific commercial product, process, or service by trade name, trademark, manufacturer, or otherwise does not necessarily constitute or imply its endorsement, recommendation, or favoring by the United States Government or any agency thereof. The views and opinions of authors expressed herein do not necessarily state or reflect those of the United States Government or any agency thereof.”

3. Executive Summary:

Motivation and Goals: The overarching goal of this project was to demonstrate the viability of vapor transport deposition (VTD) for the fabrication of efficient and stable metal-halide perovskite solar cells. VTD is a solvent-free alternative to conventional solution-processing of the light-absorbing, perovskite active layer. Since solution-processing frequently requires the use of toxic solvents, transition to a dry-processing approach has the potential to remove an obstacle to facile and economically meaningful commercialization. Further, VTD bears similarity to existing industrially-relevant processing approaches used for the production of thin-film CdTe solar modules, suggesting the potential for rapid adoption and transition to industry. Realization of this aggressive goal requires an improved understanding of precursor and perovskite film formation as a function of VTD processing conditions, integration of perovskite thin films into solar cells and demonstration of performance that is comparable to solution-processed control devices, and an understanding of defect formation and passivation in vapor-processed films, especially if comparable performance is not realized.

Given that the field has largely focused on solution-processing methods for the formation of metal-halide perovskite thin films, project objectives have been formulated to develop essential processing-structure-property-performance relationships. These design rules will be essential in informing the industrial application of vapor-processing methods for perovskites.

Major Accomplishments: Efforts under this project have led to the development of an improved understanding of VTD processing, the key parameters that control rate and morphology, the demonstration of efficiency cells based on methylammonium lead iodide ($MAPbI_3$), and the demonstration of multiple schemes to synthesize multi-A-site perovskites like $FA_{1-x}MA_xPbI_3$. Specifically, Budget Period 1 (BP1) focused on the development of a finite-element model capable of predicting deposition rate and informing processing conditions, realization of uniform precursor and co-deposited perovskite thin films, examination of the role of underlayer and processing conditions on film morphology, integration into efficient $MAPbI_3$ solar cells (champion power conversion efficiency >12%), and the probing of composition and defects in VTD-deposited films. This performance was comparable to solution-processed devices processed in parallel, and prior to this work there had been limited examination of devices processed via controlled co-deposition a carrier gas. Indeed, over BP1 the project team realized improvement in device efficiency from <1% by better understanding the role of perovskite layer composition (i.e. the need for PbI_2-rich films) and the continued optimization of electrode and transport layer materials. After revising the SOPO through the continuation process, emphasis in BP2 was on demonstrated additional chemistries using VTD. The project successful synthesized the black phase of $FAPbI_3$ via both sequential and co-deposition, and $FA_{1-x}MA_xPbI_3$ via the sequential deposition of formamidinium iodide (FAI) on a VTD-processed film of $MAPbI_3$. These films have shown promising performance in devices with champion power conversion efficiency >10%. This project has provided previously missing insight into the design rules for VTD of perovskites, potentially de-risking this promising processing method for industrial parties to pursue.

4. Table of Contents:

5. Background:

Solar cells relying on a metal-halide perovskite absorber layer have attracted significant attention in recent years due to the defect tolerance,[1] tunable band gap,[2] and relative ease of processing.[3] Metal-halide perovskites are an organic-inorganic synthetic material with a perovskite crystal structure, as shown in Figure 1. They typically have an ABX_3 stoichiometry and are composed of earth abundant elements including carbon, nitrogen, hydrogen, lead, and halogens such as iodine, bromine, and/or chlorine. The efficiency of research-based cells incorporating a single perovskite absorber has increased dramatically in recent years and reached a record efficiency of 26.7% in 2024.[4] While the efficiency demonstrated by perovskite solar cells is promising, questions around manufacturing technique and long-term stability must also be addressed to enable commercialization. The bulk of perovskite literature has relied on perovskite layers deposited out of solution, typically using toxic solvents such as dimethylformamide to solvate the precursors.[3,5] In addition to toxicity issues, the use of solvent-based processing techniques limits options for device architecture, as solvents used for subsequent layers must be carefully selected to not re-dissolve previously deposited device layers.[6] Given these challenges, vapor-processing alternatives such as chemical vapor deposition (CVD) and physical vapor deposition (PVD) have been examined as options for depositing perovskite layers.[7] These techniques sublimate perovskite precursors by heating them under vacuum, avoiding the use of solvents. PVD in particular has been demonstrated to lead to good control over perovskite film properties such as morphology, thickness, and composition, leading to devices that approach the efficiency of their solution processed counter parts.[8] A key challenge with PVD however is translation to a manufacturing scale, as it relies on ultra-high vacuum (~10^{-6} Torr), and tends to lead to low deposition rate and poor materials usage. Moderate vacuum techniques (~1 Torr) such as CVD improve on these challenges, but thus far have not led to solar cell devices with efficiencies matching those of PVD deposited films.[9]

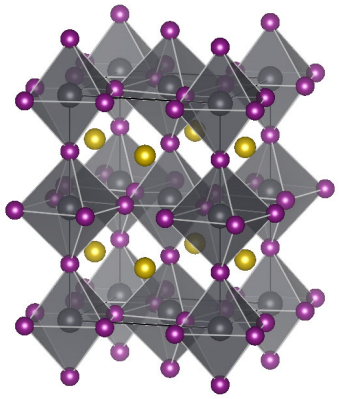

Figure 1. Crystal structure of the archetypal perovskite material, methylammonium lead iodide ($MAPbI_3$). MA^+ cations are represented by yellow spheres, Pb^{2+} cations are represented by gray spheres surrounded by translucent gray octahedra, and I^- anions are represented by purple spheres at the corners of the octahedra. Figure generated in VESTA.

The technique of interest in this work is vapor transport deposition (VTD), operating at ~1 Torr. VTD involves heating the perovskite precursors to sublimate them, then using a nitrogen carrier gas to sweep the sublimated precursor vapors to a substrate where they condense and react to form a perovskite film.[10,11] Analogs of VTD are currently used to deposit cadmium telluride (CdTe) solar cells, the dominant thin film technology currently commercialized, meaning the results of this project could have strong potential to contribute to the commercialization of perovskite solar cells. Previous work on perovskite solar cells from PI labs has demonstrated an ability to rapidly deposit a

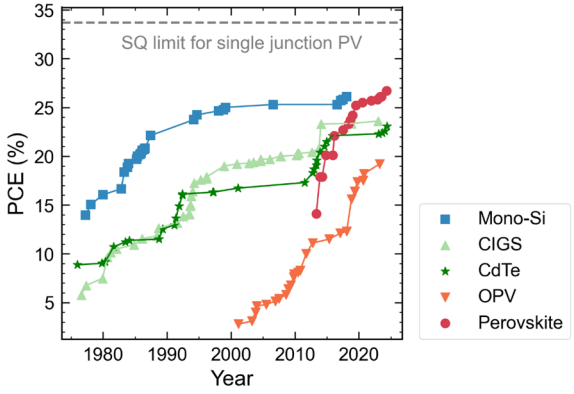

Figure 2. Plot of the champion research cell power conversion efficiencies for single crystalline silicon, copper indium gallium selenide (CIGS), cadmium telluride (CdTe), organic photovoltaics (OPV), and metal halide perovskites summarized by the national renewable energy laboratory (NREL). Adapted from Ref 4.

perovskite absorber layer (~1.3 nm/s),[10] the ability to control the morphology and composition of tin-based perovskite layers,[11] and the ability to deposit perovskite-perovskite heterojunctions with sharp interfaces via VTD.[6]

This project draws upon other perovskite vapor processing and device literature. Work from the Bolink group has highlighted the viability of high-vacuum vapor processed perovskites for solar cell devices.[8,12] They have also demonstrated control over morphology and composition for highly reproducible perovskite films,[12] and deposited films with a variety of A-site cations for devices with efficiencies over 18%.[8] Tavakoli *et al.* demonstrated the viability of moderate vacuum vapor processing using a tubular reactor inside of a furnace to sublimate methylammonium iodide (CH_3NH_3I; MAI) and lead iodide (PbI_2) and an Ar carrier gas to deposit perovskite devices, leading to devices with an efficiency of 11.1% for films incorporating a chloride halogen.[13] More recently Sahli *et al.* used a sequential deposition approach to deposit vapor processed perovskites, depositing a PbI_2 layer via PVD then using a shower head VTD geometry to incorporate MAI, leading to conversion to a perovskite film and yielding devices with an efficiency of 10.7%.[14] Leyden et al. demonstrated the incorporation of formamidinium cations ($CHN_2H_5^+$; FA^+) into a CVD deposited perovskite film, highlighting both the challenges of incorporating the FA^+ cation as opposed to the MA^+ cation as well as the benefits to long term stability of the perovskite structure.[15] Moser *et al.* similarly studied FA^+ incorporation via VTD, highlighting the narrow parameter space required to optimize incorporation.[16]

This project leverages existing studies of vapor processed perovskite films to deposit lead-based VTD processed perovskite devices incorporating both MA^+ and FA^+ cations. This work expands upon existing studies by closely studying the impact of deposition parameters on the controlling film composition for device efficiency in VTD processed films, studying the impact of vapor processing parameters on the impurities present in formed perovskite films, and examining a variety of different processing approaches as options for forming a perovskite film that shows good performance in a device. Processing parameters impact on film uniformity and reproducibility are of particular interest to this project and are examined both computationally and experimentally as they relate to system design. Incorporation of impurities, alternative processing approaches, and specific limitations are explored in detail.

6. Project Objectives:

Metal-halide perovskite solar cells offer an attractive combination of high efficiency and the potential for low-cost processing. To date, the community has focused largely on solution-processing methods to synthesize the light-absorbing, metal-halide perovskite thin film. Solution-processing could encounter challenges for scale-up due to the use of often toxic-solvents during processing. This project seeks has sought to develop relevant design rules for the processing of metal-halide perovskites via an alternative vapor-processing approach known as vapor transport deposition (VTD). The tasks and sub-tasks associated with the project as described in the SOPO are as follows:

Budget Period 1
Task 1.0: Develop process model to guide thin film, interface, and device design
Task Summary: Develop models to understand how deposition parameters in vapor transport deposition influence film growth rate and uniformity. Models will be compared to experimental data including thickness and film uniformity.

Subtask 1.1: Establish processing-structure design rules for each precursor (e.g. MAI, PbI_2)
Subtask Summary: Thin films of each perovskite precursor will be deposited using vapor transport deposition systems at Minnesota and MIT. Process variables of interest include substrate temperature, deposition rate, chamber pressure. Film uniformity will be characterized using ellipsometry and/or profilometry, and where needed atomic force and scanning electron microscopies.

Subtask 1.2: Establish processing-structure design rules for films of $MAPbI_3$
Subtask Summary: Using co-deposition, $MAPbI_3$ thin films will be deposited based on processing conditions informed from Subtask 1.1. Of interest is film composition, morphology, and uniformity, and the role of substrate. Composition and morphology will be probed using X-ray diffraction, scanning electron microscopy, and X-ray photoelectron spectroscopy and/or Rutherford Backscattering. The goal is to establish processing conditions capable of yielding phase pure films with tunable grain size over 1 inch x 1 inch substrates.

Subtask 1.3: Construct and validate model for process parameter selection, precursor and perovskite film growth rate, uniformity, and composition
Subtask Summary: Numerical methods will be used to develop transport models to interpret data in Subtask 1.1 and 1.2, identifying the regime of deposition and permitting optimization of processing parameters to ensure deposition rate is controlled by carrier gas flow rate. These models will also be adapted to predict actual deposition rate for a given set of processing conditions, allowing for the inclusion of substrate temperature as a controlling parameter.

Task 2.0: Establish the dependence of solar cell performance on perovskite film morphology by varying perovskite process conditions
Task Summary: This task will apply the processing understanding developed in Task 1 to characterize the dependence of perovskite optoelectronic performance on processing

conditions. This insight will be used to design initial solar cells, while also informing the optimization of the back charge transport layer-perovskite interface to control layer morphology.

Subtask 2.1: Characterize the optoelectronic behavior of $MAPbI_3$ thin films as a function of processing conditions.
Subtask Summary: The films constructed in Subtask 1.2 will be characterized for their charge carrier mobility and density (Hall Effect), and carrier lifetime (transient photoluminescence).

Subtask 2.2: Construct and characterize solar cells as a function of perovskite layer processing conditions.
Subtask Summary: Using the results of Subtask 1.2 and 2.1, solar cells will be constructed to identify baseline level of optimization and performance. Characterization will include stabilized power output current-voltage measurements (SPO JV), external quantum efficiency (EQE), and T80 maximum power point tracked (MPPT) lifetimes. Several architectures and transport layers will be considered in preparation for Subtask 2.3.

Subtask 2.3: Engineer the transport layer/perovskite interface to optimize perovskite morphology and minimize defects.
Subtask Summary: Building off activities of Subtask 2.2, the back interface between the transport layer and perovskite will be optimized for improved efficiency and stability. This may include the addition of interlayers or vapor-based treatments to affect favorable control over grain growth in the subsequent perovskite layer. In addition to probing changes in morphology for the perovskite layer, solar cells will be constructed and characterize as described in Subtask 2.2.

Task 3.0: Engineer perovskite-perovskite interfaces for interface stability and inclusion in devices
Task Summary: This task will exploit the unique processing advantages of vapor transport deposition to engineer perovskite-perovskite heterojunctions for application in solar cells. This task will include the processing of heterojunctions, examination of interface stability, and application in devices.

Subtask 3.1: Construct all vapor-deposited perovskite heterojunctions and probe interface stability and mixing.
Subtask Summary: Heterojunctions will be constructed by varying the A-site or B-site cation across the interface. Junction formation will be verified using a combination of optical absorption, X-ray diffraction, depth profile X-ray photoelectron spectroscopy, and Rutherford Backscattering. Stability will be probed as a function of time.

Subtask 3.2: Construct a solar cell with a perovskite charge transport layer using vapor transport deposition.
Subtask Summary: The charge transport behavior of heterojunctions will be examined to determine how best to incorporate a perovskite charge transport layer into a solar cell.

Once an architecture is selected, solar cells will be characterized according to the metrics Subtask 2.2.

Task 4.0: Enhancing device stability by targeting defects in vapor transport deposited films
Task Summary: Device stability will be engineered by more thoroughly considering the unique slate of defects common to vapor-deposited perovskite thin films, and engineering the perovskite-top charge transport layer interface for optimized device stability.

Subtask 4.1: Identify defects in vapor transport deposition films
Subtask Summary: The most common surface and bulk defects in vapor-processed films will be identified. Due to the thermal stress during deposition, there is likely ion migration specifically of the MA+ cation or degradation product pairs CH3I/NH3 and HI/CH3NH2. The presence of degradation products within the film can be confirmed using gas chromatography mass spectrometry (GCMS) or Fourier Transform – infrared (FTIR). Using techniques such as transient absorption or impedance measurements and comparing those to likely defects as calculated by the formation energy found in density functional theory we will track the influence these defects have on trap states and device performance/stability. These results will be used to inform further device engineering. From there we will optimize processing conditions or use targeted Lewis acid or base treatments to mend the defect.

Subtask 4.2: Translate current top solution-based passivation techniques to vapor-processing.
Subtask Summary: Focus will be on converting top solution-processed passivation techniques into vapor-processed, scalable deposition methods. Treatment material groups will include (but not limited to) ammonium salts, Lewis acids/bases, and zwitterions. Characterization of films would determine if solution-based passivation treatments are appropriate and/or effective for vapor-deposited perovskite films. The films in this task will be re-characterized according to techniques developed in Subtask 4.1.

Subtask 4.3: Engineer post-deposition passivation techniques to improve device stability
Subtask Summary: The final selection of device architecture and processing will be influenced by the results of Subtask 2.3 and Subtask 4.2. The devices in this task will be compared on the same characterization metrics as Task 2. Care will be given to thoroughly testing all layer combinations to find the device with the best efficiency and stability.

Budget Period 2
Task 5.0: Demonstration of efficient solution-processed architecture to validate transport layers.
Task Summary: In moving beyond BP1 efficiency goals, demonstrate a solution-processed architecture capable of high efficiency to confirm viability of transport layers and transport layer-electrode interfaces for testing of VTD perovskite absorber layer toward EOP-A efficiency goals.

Subtask 5.1: Optimize solution-processed devices based on multiple A- and/or X- site cations to realize >20% power conversion efficiency (PCE) for champion devices and >15% mean PCE over >20 devices.
Subtask Summary: Engineer solution-processed absorber and transport layers to maximize PCE. Emphasis will be on the inclusion of additional cations and anions beyond $MAPbI_3$ and the use of transport layers developed at MIT. Completion of this subtask and task will provide the team with an architecture whose solution-processed absorber layer can switched with one processed via VTD for performance comparison.

Task 6.0: Expanding perovskite composition in VTD-processed films for increased efficiency and stability.
Task Summary: Expand on BP1 efforts using MAPbI3 by including additional A- and/or X-site ions into the structure to enhance device efficiency and stability. Emphasis is on the use of FA-majority A-site perovskites.

Subtask 6.1: Apply post-deposition treatments to introduce additional ions into VTD-deposited MAPbI3 and enhance device efficiency and stability.
Subtask Summary: Translation of top solution-processed passivation techniques into vapor-processed MAPbI3 films. Initial efforts will involve use of transient PL to screen potential improvement from different treatment and passivation schemes. Films with promising lifetime improvement will be integrated into devices and characterized.

Subtask 6.2: Demonstrate the ability for VTD to deposit black phase FA-rich perovskites.
Subtask Summary: Efforts to date have focused on the use of co-deposition in VTD to produce MAPbI3. This will introduce an additional FA source into the VTD system at UMN to create films of FAxMA1-xPbI3 (majority FA) and characterize uniformity of morphology and composition. Different deposition schemes will be considered including triple source co-deposition and a sequential deposition of MAPbI3 and FAI.

Subtask 6.3: Engineer FA-containing perovskite composition to optimize device efficiency and lifetime.
Subtask Summary: The films of Subtask 6.2 will be integrated into the device architectures of Subtask 5.1 to characterize both efficiency and lifetime as a function of absorber layer composition.
The associated milestones and go/no-go points are as follows:

#	Anticipated Month of completion	Performance Metric	Success Value	Assessment Tool / Method of Measuring Success Value	Verification Process
1.1.1	6	Process Model	Model to guide deposition parameters towards manufacturing compatibility.	Experimental verification throughout deposition parameters. Film uniformity across substrate via ellipsometry and profilometry. Composition confirmed through absorbance, XRD, and depth-profiled XPS.	Experiments verify model to within 20% of expected value across multiple parameters.
1.2.1	12	Precursor Film Uniformity	<10% variation in precursor	Measurement of thickness maps for precursor films (MAI	Spatial mapping of film thickness

#	Anticipated Month of completion	Performance Metric	Success Value	Assessment Tool / Method of Measuring Success Value	Verification Process
			film thickness over 1 cm^2 with thickness maps reproducible across 3 process runs.	and PbI_2) films. Repeated for 3 separate depositions to also assess reproducibility for a given set of process conditions. Thickness maps and histograms will be compared between runs.	using spectroscopic ellipsometry.
1.2.2	12	Film Morphology	Establish role of substrate and deposition conditions on perovskite film morphology – 3 substrate types, 3 sets of processing conditions, reproducible grain size (<10%) across 3 depositions	Measurement of perovskite film morphology on 3 unique substrates/underlayers (e.g. metal oxides, TCOs, organics) and for 3 unique sets of processing conditions by SEM and XRD.	Contrast morphology on different substrates and using different processing conditions with SEM and XRD. Realize <10% variation in grain size for films on a given substrate type for 3 runs with the same process parameters.
1.2.3	12	Film Morphology – Impact on Cell Efficiency	Establish role of substrate on cell efficiency for 3 substrate types, reproducible device performance (<10%) across 3 depositions	Measurement of cell performance for 3 unique substrates/underlayers (e.g. metal oxides, TCOs, organics) by SPO JV and EQE.	Contrast device performance on different substrates. Realize <10% variation in device efficiency for a given substrate across 3 runs with identical process parameters.
1.2.4	18	Device Efficiency	Solar cells (>1mm^2) with power conversion efficiency ≥9%.	SPO JV with initial hysteresis resulting in <1% change in efficiency.	Raw data sent to DOE.
1.2.5	24	Device Stability	Solar cells (>1mm^2) with T80 lifetime of 750 hours.	Table of T80 lifetimes measured under inert conditions with at least one device reaching 750 hours.	Raw data with accompanying report sent to DOE.
1.3.1	24	Interface Stability	Identify mobile ions across perovskite-perovskite heterojunctions for 3 unique samples (deposition conditions and composition).	Deposit perovskite bilayers by VTD and probe layer segregation by absorption, XRD, and/or depth-profiled XPS.	Transition from double onset to single onset in optical absorption, transition to alloy characteristic XRD scattering peaks, graded or mixed composition in XPS profiles.
1.4.1	24	Bulk Ion Mobility	Identify mobile ions in perovskite films for 3 unique sets of	Use targeted Lewis acid/base treatments to identify mobile ions and compare via FTIR, depth-profiled XPS, and impedance spectroscopy.	See consistent results across samples deposited via the same parameters.

#	Anticipated Month of completion	Performance Metric	Success Value	Assessment Tool / Method of Measuring Success Value	Verification Process
			deposition conditions.		
1.4.2	24	Perovskite Film Uniformity	<10% variation in perovskite film thickness over 1 cm^2 with the thickness map reproducible (<10%) across 3 process runs.	Measurement of thickness maps for perovskite films. Repeated for 3 separate depositions to also assess reproducibility for a given set of process conditions. Thickness maps and histograms will be compared between runs.	Spatial mapping of film thickness using spectroscopic ellipsometry.
GNG – 1A	24	Solar Cell Efficiency	Solar cells (>1mm^2) with power conversion efficiency ≥14%.	SPO JV with initial hysteresis resulting in <1% change in efficiency.	Raw data sent to DOE.
GNG-1B	24	Process Modeling for Scale-Up	Experimental agreement with process model predictions, Predictions for scale-up	Verification of model by ability to predict deposition rate for perovskite thin films. Utilization of model to predict upper limits for deposition rate, film uniformity.	Experiments verify model to within 20% of expected value across multiple parameters. Prediction of deposition and film thickness as a function of process parameters.
GNG – 1C	24	Stakeholder Engagement	New Findings to Relevant Companies	Disseminate published information to at least First Solar and Swift Solar	Link and slides sent to DOE before meeting.
GNG-1D	24	Dissemination of Results	Presentation/Publication of DOE-funded results	Presentation at national conference and/or publication in peer-reviewed journal	Presentations and publications provided to DOE.
2.5.1	30	Device Efficiency, Validation of device architecture on material stack	>20% PCE champion, >15% PCE mean over ≥20 devices with active layers solution deposited on two different days.	SPO JV, EQE to validate achieved Jsc for >5% of device set	Data sent to DOE with statistical analysis, process conditions, and material stack details.
2.6.1	30	Compositional uniformity	Black phase FA-rich perovskite is dominant composition in film; <30% variation in minority phase composition	Thin film is partitioned into no fewer than 6 sections, XRD taken on each section. Compositional uniformity is quantified by either minority phase peak height or integrated peak area. Sections must include the entire film and sample both the middle and corners of the film. FA on films must be deposited by VTD	Raw data sent to DOE, with photos of how the film was partitioned/sectioned

#	Anticipated Month of completion	Performance Metric	Success Value	Assessment Tool / Method of Measuring Success Value	Verification Process
2.6.2	30	Device Efficiency	Solar cells (>1mm^2) with >50% FA composition (mole basis) achieve mean power conversion efficiency ≥15% for devices with perovskite layers deposited across three distinct VTD runs.	SPO JV, FA composition validated by a compositional analysis such as NMR or XPS, Jsc validated by EQE for >5% of sample set including champion device	Raw data sent to DOE.
2.6.3	33	Device Stability	Solar cells (>1mm^2) that pass 2.6.2 achieve >12.5% PCE mean after 500 hours at ISOS-D-2	SPO JV after aging, Jsc validated by EQE for >5% of sample set	Raw data with accompanying report sent to DOE.
EOP - A	36	Solar Cell Efficiency	Average device PCE >19% on a stabilized power output (SPO) basis	Average device PCE >19% for 2 devices across three process runs, with four pixels per run, Jsc validated by EQE for >20% of device set including the champion device	Measured at UMN and/or MIT
EOP - B	36	Solar Cell Stability	Solar cells achieve >14% PCE (SPO basis) after 500 hours at ISOS-D-2	Average lifetime for encapsulated devices across three process runs, with four pixels per run, Jsc validated by EQE for >20% of device set including the champion device.	Raw data with accompanying report sent to DOE.
EOP -C	36	Stakeholder Engagement	New Findings to Relevant Companies	Disseminate published information to at least one company pursuing vacuum deposited perovskite manufacturing and/or tool development	Link and slides sent to DOE before meeting.
EOP -D	36	Dissemination of Results	Presentation/Publication of DOE-funded results	At least one presentation at a conference and one publication in peer-reviewed journal not included in GNG-1D requirement.	Presentations and publications provided to DOE. Milestone is complete upon proof of journal submission (not acceptance) and conference abstract acceptance.

7. Project Results and Discussion:

7.1 Reactor Designs

In terms of deposition systems, the project initially utilized two deposition systems, one at UMN and one at MIT, shown in Figure 1. Over time, emphasis was placed on material deposited in the VTD system at UMN while the system at MIT was redesigned and replaced. The VTD system at UMN consists of a hot-wall reaction chamber consisting of a three-zone furnace, with a quartz tube of having an inner diameter of 7.5 cm inserted inside. For the deposition of $MAPbI_3$, the first and second zones are typically set at ~360˚C, to sublime precursor powders and prevent condensation on the chamber wall. The third zone is typically set at ~268˚C to improve control over substrate temperature, which again for $MAPbI_3$ is set at 44˚C. Precursor powders are loaded into a coarse porosity gas dispersion tube, fixed on a linear feedthrough, and inserted into separate 1 cm diameter quartz source tubes. A N_2 carrier gas flows through each source tube to transport material vapor towards the substrate. An additional N_2 dilution gas inlet is located around the source tubes and used to realize additional control over the uniformity and deposition pressure. The new MIT system is designed similarly to the UMN system, see description and schematic under Task 6. The throw distance is defined as the lateral distance between the source tube opening and the substrate and is 15.9 cm.[11,17]

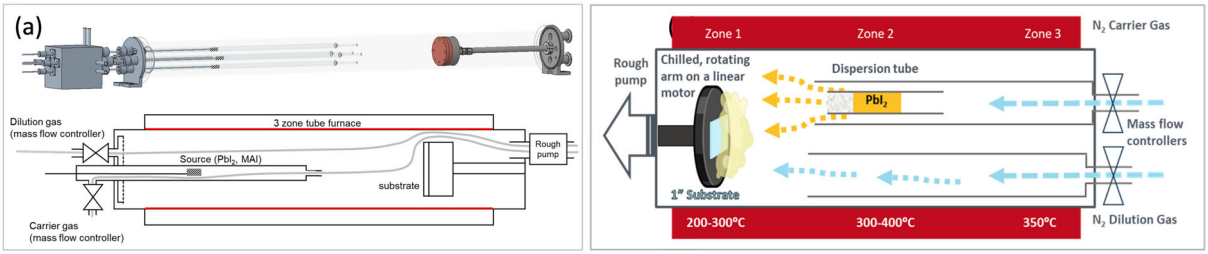

(c)

	PbI_2 Source T	PbI_2 Flow Rate	MAI Source T	MAI Flow Rate	Chamber Pressure	Dep. Zone T	Substrate T	throw distance	substrate holder size
UMN	330~355°C	3~50 sccm	140°C	5~10 sccm	0.1~10 Torr	200~360°C	20-121°C (calc)	15.24 cm	Ø 6.35 cm
MIT	325~400˚C	10~100 sccm	150~180°C	2~20 sccm	0.1~10 Torr	200-300°C	60-200°C (calc)	10 cm	Ø 4 cm

Figure 1: *Schematic of VTD systems at (a) UMN and (b) MIT with (c) table summarizing typical operating parameters for deposition of both precursor films and perovskite films. Not that the schematic describing the UMN system is simplified, the actual system consists of multiple separate sources for each precursor.*

7.2 Results and Discussion - Budget Period 1 Tasks

Task 1.0: Develop process model to guide thin film, interface, and device design
Task Summary: Develop models to understand how deposition parameters in vapor transport deposition influence film growth rate and uniformity. Models will be compared to experimental data including thickness and film uniformity.

One of the initial goals of this work was to determine precursor deposition rates and the quality of precursor films as a function of VTD processing conditions including carrier gas flow rate, source temperature, and chamber pressure. Previous work on varying carrier gas flow rate had shown that the precursor deposition rate and carrier gas flow rate are

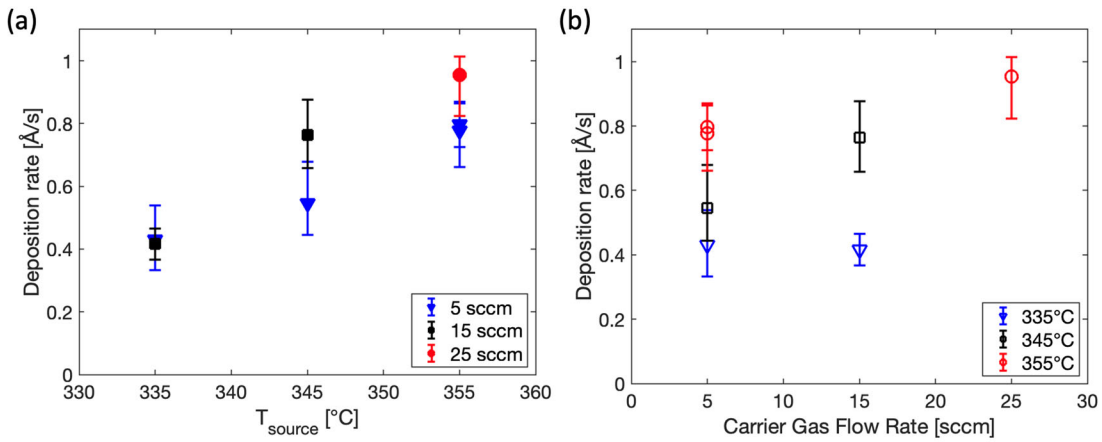

Figure 2: *(a) Deposition rate vs. source temperature for PbI_2 in the UMN system. (b) Deposition rate vs carrier gas flow rate for PbI_2 in the UMN system.*

proportional (for Sn-perovskites in the UMN system).[11] Under the operating conditions used for the films studied in this work, this correlation was found not to be as strong for PbI_2 (perovskite precursor) as compared to the tin halide precursors. Initial work found some inconsistency in the precursor deposition rate dependence on carrier gas flow rate, possibly reflecting a difference in operating regime, as under certain deposition conditions the precursor deposition rate will be in the kinetic regime, where deposition rate is no longer well controlled by carrier gas flow rate. We instead found that the PbI_2 precursor deposition rate is more strongly dependent on source temperature than carrier gas flow rate (Fig. 2).

To further analyze the parameter space and routes to higher deposition rates, additional modeling of the UMN system was performed in COMSOL. The model for the UMN system is shown in Figure 3. The model includes two source tubes based on the symmetry of the system. The N_2 carrier gas flows through each source tube to transport material vapor towards the substrate. An additional N_2 dilution gas inlet is located around the source tubes and used to realize additional control over the fluid flow field and pressure.[11,18,19] For simplicity, three dilution gas inlets were used to mimic the shower head feature in the 2D model. As noted previously, the throw distance is defined as the lateral distance between the source tube opening and the substrate and is 15.9 cm for the VTD system considered in our prior work.[11]

In the simulation, the source evaporation rate is derived from the Hertz-Knudsen equation and the Clausius-Clapeyron equation, while assuming ideal gas behavior.[10,18,19] After building the model and setting boundary and initial conditions, the fluid velocity field, temperature and concentration profile in the system are obtained. Our interest was in investigating the deposition process by adjusting four independent processing parameters: source material temperature (T_{PbI2}), carrier gas ($\dot{V}_{cg}$) and dilution gas ($\dot{V}_{dil}$) flow rates, and deposition pressure (P). Two metrics, deposition rate (r_{dep}) and nonuniformity were used to evaluate the impact of these parameters. The deposition rate was calculated as:

$$\mathrm{r_{dep}}\left(\frac{\text{Å}}{\mathrm{s}}\right) = \frac{\text{total flux, x}\left(\frac{\mathrm{mol}}{\mathrm{m^2 \cdot s}}\right) \times \mathrm{M}\left(\frac{\mathrm{kg}}{\mathrm{mol}}\right)}{\rho\left(\frac{\mathrm{kg}}{\mathrm{m^3}}\right)} \times 10^{10}\left(\frac{\text{Å}}{\mathrm{m}}\right) \quad (1)$$

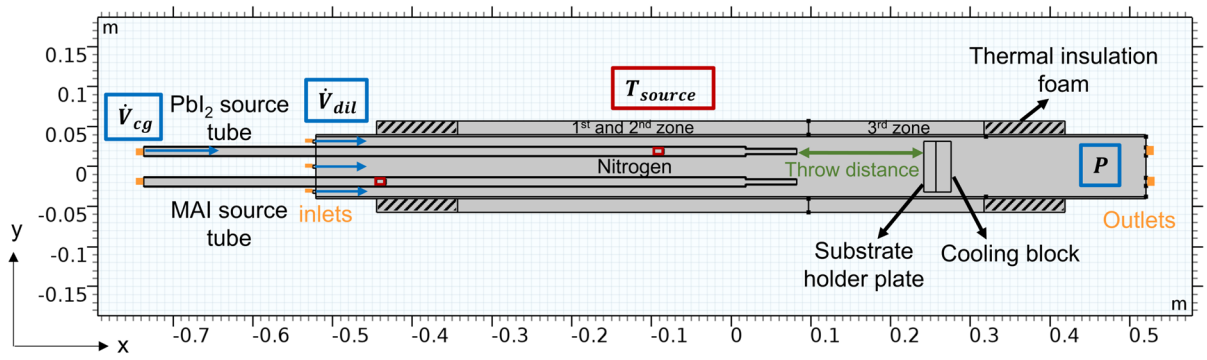

Figure 3. *Illustration of model used to simulate deposition rate and uniformity in a VTD system. The four adjustable parameters of interest are source material temperature (T_{source}), carrier gas flow rate ($\dot{V}_{cg}$), dilution gas flow rate ($\dot{V}_{dil}$) and pressure (P).*

including the total material flux in the x-direction on the substrate holder, where *M* is the molecular weight and *ρ* is the density. The molecular sticking coefficient is assumed to be unity as the substrate temperature is low compared to the precursor sublimation temperature. When not explicitly stated, r_{dep} is calculated at the center point on the substrate. The spatial nonuniformity of the deposition rate is defined as the standard deviation across the center 5 cm width of the substrate holder (total substrate holder width is 6.35 cm) divided by the average deposition rate. The parameter space of interest is T_{PbI2} = 330°C - 410°C, $\dot{V}_{cg}$ = 5 - 200 sccm, $\dot{V}_{dil}$ = 0 - 500 sccm, and *P* = 0.01 - 100 Torr. Finally, the impact of source-to-substrate throw distance is also considered.

As shown in Figure 4, source material temperature controls the evaporation rate while the carrier gas flow facilitates vapor transport to the substrate. A deposition rate of 10 - 1000 nm/s could potentially be reached when processing MHP precursor by VTD. In the limit of large gas flow rates, the convective flux is increased, bypassing the substrate holder, and reducing the deposition rate. Under some conditions, an additional dilution gas flow is found to help with the development of a uniform flow pattern and concentration distribution at the substrate. However, consideration of additional geometrical design considerations, such as the number

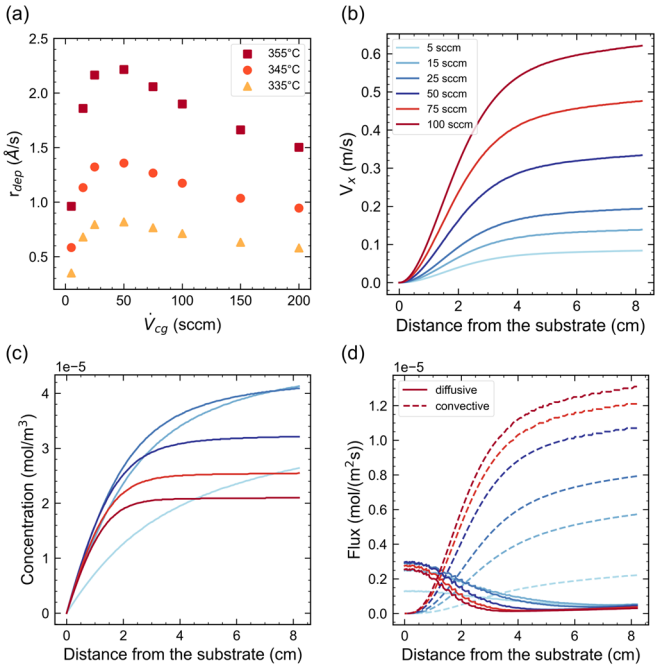

Figure 4. *(a) Simulated PbI_2 deposition rate as a function of $\dot{V}_{cg}$ and T_{PbI2}. Deposition pressure and $\dot{V}_{dil}$ were fixed at 2.6 Torr and 25 sccm. (b) PbI_2 fluid velocity in the x-direction (V_x), (c) concentration, and (d) flux along the central axis of the substrate as a function of $\dot{V}_{cg}$. For (b), (c), and (d), T_{PbI2} was fixed at 355°C.*

of gas inlets, the inlet position and the shape of shower head, must be made. The deposition pressure is found to be an important parameter to further increase the deposition rate with only a weak impact on film uniformity. Maximizing deposition rate and uniformity can be achieved by using a high $\dot{V}_{dil}$ combined with high source material temperature, while additional fine-optimization of the rate can be accomplished by adjusting P and $\dot{V}_{cg}$. While the source-to-substrate throw distance can also impact deposition rate and uniformity, its role can be reduced in reactors with length-to-width aspect ratio greater than unity.[20] This study led to source temperature being a major focus for increasing deposition rate in future work and helped meet Milestone 1.1.1.

To assess the uniformity of precursor films to meet Milestone 1.2.1, precursor films from the UMN system were examined using thickness mapping by variable-angle

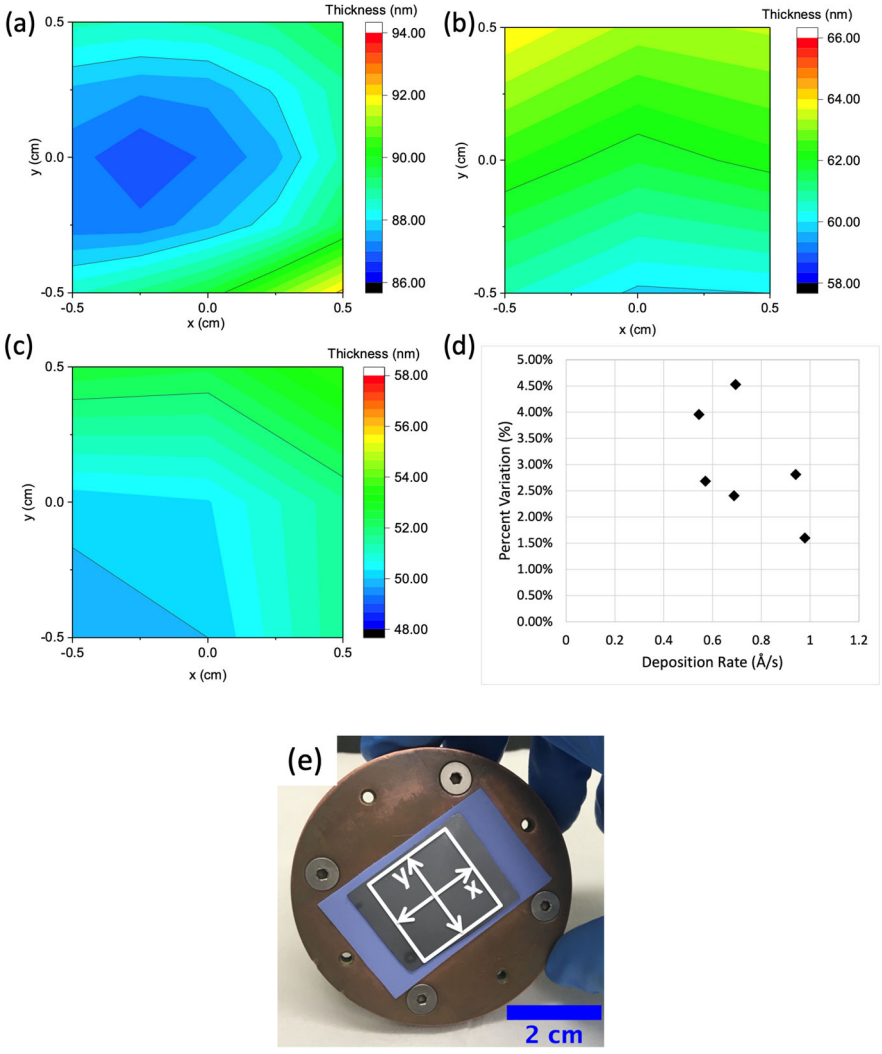

Figure 5: *(a)-(c) Thickness maps of MAI depositions. Average thickness based on central 1x1 cm^2 region of substrate. Thickness measured on a spectroscopic ellipsometer. Deposition conditions were (a) Carrier gas flow rate = 3 sccm; source temperature = 140˚C; P = 2.6 Torr; deposition time = 15 min (b) Carrier gas flow rate = 5 sccm; source temperature = 140˚C; P = 2.6 Torr; deposition time = 15 min (c) Carrier gas flow rate = 5 sccm; source temperature = 140˚C; P = 2.6 Torr; deposition time = 15 min. (d) Scatter plot of percent variation vs. deposition rate for MAI depositions in the UMN VTD system. (e) Image of silicon substrate mounted on substrate holder to demonstrate axis orientation.*

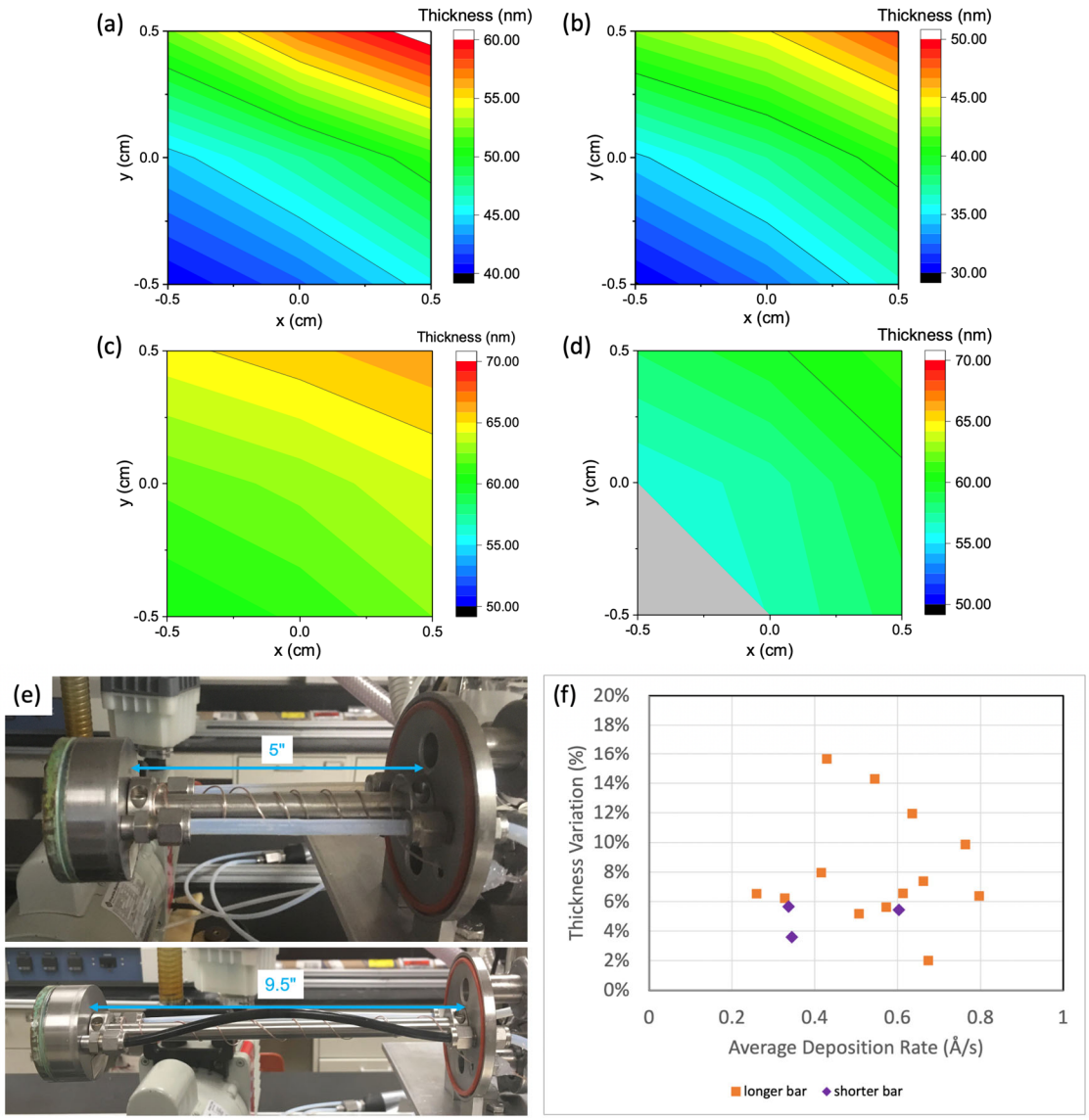

Figure 6: *(a)-(b) Thickness maps of PbI_2 films prior to shortening the substrate holder bar. Average thickness based on central 1x1 cm^2 region in center of substrate. (c)-(d) Thickness maps of PbI_2 films after shortening the substrate holder bar. Average thickness based on central 1x1 cm^2 region in center of silicon substrate. Gray region in (d) represents are of high MSE (>10). Deposition conditions were (a) Carrier gas flow rate = 5 sccm; source temperature = 355˚C; P = 2.6 Torr; deposition time = 15 minutes. (b) Carrier gas flow rate = 5 sccm; source temperature = 335˚C; P = 2.6 Torr; deposition time = 30 minutes. (c) Carrier gas flow rate = 5 sccm; source temperature = 355˚C; P = 2.6 Torr; deposition time = 15 minutes. (d) Carrier gas flow rate = 5 sccm; source temperature = 355˚C; P = 2.6 Torr; deposition time = 15 minutes. (e) Images showing adjustments made to the substrate holder bar. (f) Scatter plot of percent variation vs. deposition rate for PbI_2 deposition in the UMN VTD system.*

spectroscopic ellipsometry (VASE). As shown in Figs. 5 and 6, films based on both MAI and PbI_2 were realized with average percent variations in thickness <10%, completing Milestone 1.2.1. Average percent variation in thickness across a 1x1 cm^2 region in the center of the silicon substrate was 3.0% for MAI across 6 depositions.

In considering the uniformity of PbI_2 thin films, some modification to the VTD system was required to maximize uniformity. Looking at Figs. 6a and 6b, it was clear that

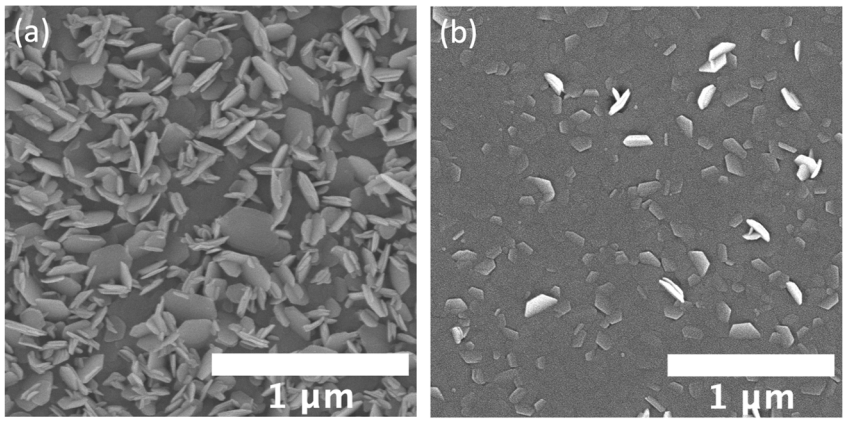

Figure 7: *SEM images of PbI_2 films grown on silicon substrates with carrier gas flow rates of (a) 100 sccm and (b) 5 sccm. All other deposition conditions were consistent across the two depositions. Source temperature = 355˚C; chamber pressure = 2.6 Torr; deposition time = 15*

PbI_2 films had a systematic thickness gradient across the film. To reduce substrate temperature and any flow non-uniformities, the bar that supports the substrate (Fig. 6e) was shortened, increasing the throw distance for PbI_2. Prior to increasing the throw distance for PbI_2, an average percent variation in thickness was 8.1% across 13 depositions, though with a distinct gradient (Fig. 6a and 6b). After increasing the throw distance, an average percent variation in thickness of 4.9% was observed across 3 depositions, with a less pronounced gradient. No noticeable difference in percent variation in MAI thickness was observed after shortening the substrate holder. Examples of thickness maps of select precursor growths and scatter plots of deposition rate vs. percent variation (Figs. 5 and 6) illustrate this further. The need to optimize throw distance for film uniformity is a system feature that should be considered more closely in transitioning VTD from lab-scale to a commercial scale.

In addition to considering deposition uniformity, films at UMN were also assessed via SEM for continuity as a framework for the eventual deposition of $MAPbI_3$ films. Of particular interest were differences in PbI_2 morphology observed with changes in processing conditions. Both carrier gas flow rate and substrate had a noticeable impact on PbI_2 platelet orientation, as shown in Figs. 7 and 8. PbI_2 films grown at higher carrier gas flow rates show a more random grain orientation relative to the substrate, while those grown at lower carrier gas flow rates tend to be oriented parallel to the silicon substrate. For rougher substrate surfaces, such as ITO/TiO_2 and ITO/SnO_2 which serve as ETLs for UMN device growths, the PbI_2 platelets were oriented randomly relative to the substrate surface regardless of the carrier gas flow rate, as illustrated by the top view SEM images and 2D XRD patterns shown in Fig. 8.[21]

Improvements in precursor uniformity and an improved understanding of the impact of substrate and carrier gas flow rate on precursor morphology later helped inform deposition conditions and chamber design decisions, such as shortening our substrate holder bar, that led to improved efficiency and film uniformity for $MAPbI_3$ devices. As noted, PbI_2 films grown on rougher substrates like ITO/SnO_2 and ITO/TiO_2 had more randomly oriented platelets relative to the substrate, while those grown on smoother substrates like glass and ITO/PEDOT typically had platelets oriented parallel to the substrate surface. Perhaps as a result of this, PbI_2 excess was more likely to be present in films grown on smoother substrates compared to those grown on rougher substrates, as discussed further under Task 2.

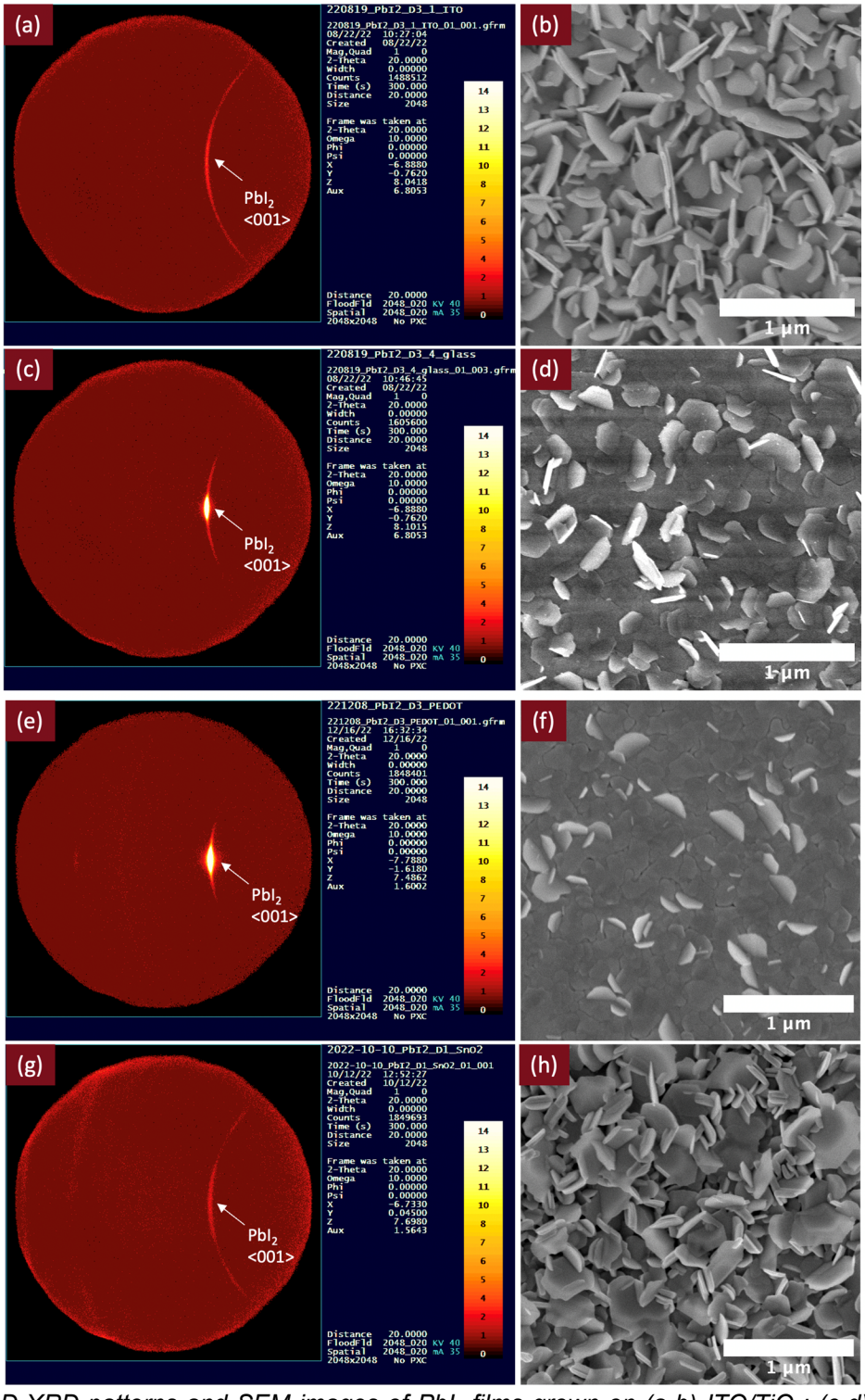

Figure 8: *2D XRD patterns and SEM images of PbI_2 films grown on (a-b) ITO/TiO_2; (c-d) glass; (e-f) ITO/PEDOT:PSS; (g-h) ITO/SnO_2. XRD patterns obtained using Co-Ka source. Deposition conditions were identical for all films.*

In the MIT system, initial non-uniformities were observed for the deposition of MAI thin films. These non-uniformities reflected ineffective cooling across the substrate (Fig. 9). Indeed, MAI films on silicon substrates were found to be uniform while those on glass substrates varied in thickness. Upon further investigation, it was found that the increased bending radius and decreased thermal conductivity of glass prevented uniform cooling of the substrate which translates into MAI thickness varying from substrate center to edge. Through engineering of the thermal pad between the substrate and the copper cooling block, MAI films on glass also became uniform.

The MIT system also realized uniform films of PbI_2. Figure 10 shows thickness mapping of three films from different runs, all present thicknesses within 5% of each other. For each individual film, we identified an area of 1cm x 1 cm or larger, with thickness variation lower than 10%.

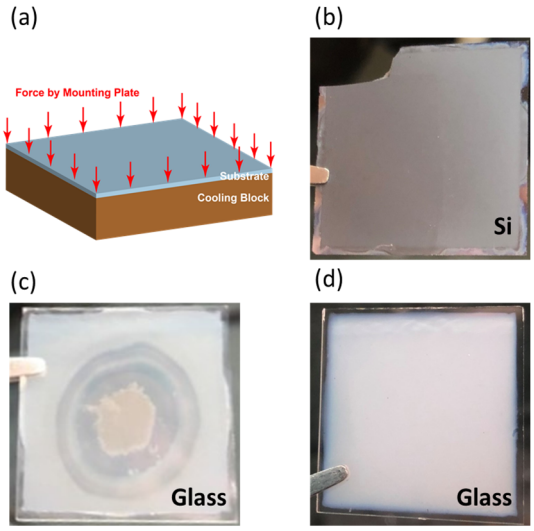

Figure 9: *Importance of substrate mounting on MAI film uniformity in the MIT system. (a) The substrate is held to the cooling block by applying even pressure to all four sides of the substrate. Depending on the flexibility of the substrate there may be upward bending in the middle of the substrate. (b) Uniform deposition on a silicon substrate. (c) Non-uniform deposition on a glass substrate due to a gap between the substrate and cooling block in the middle. (d) Uniform MAI deposition on glass after engineering a thermal pad to conform to the glass bending.*

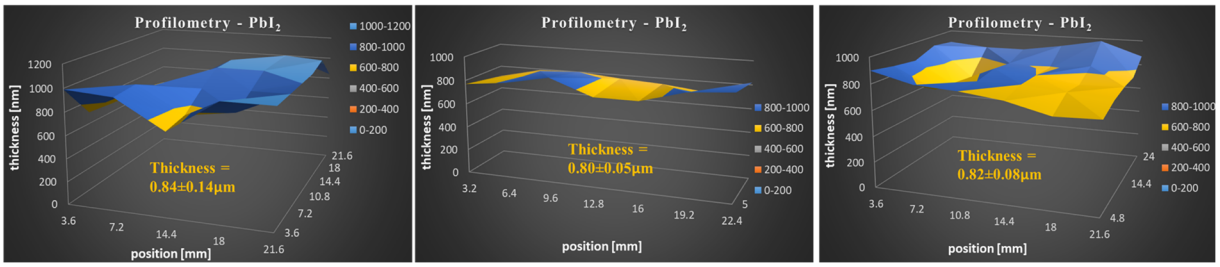

Figure 10: *Profilometry results for 3 lead iodide films deposited in different days, with the same deposition conditions, (source temp of 340˚C; carrier gas flow rate of 100 sccm; chamber pressure of 0.6 Torr; substrate temperature of 70˚C, deposition time of 15 minutes) exhibit thickness uniformity across each film individually as well as thickness reproducibility (~0.8 µm) over different runs.*

In addition to improving film uniformity, we also aimed to establish processing design rules to control morphological and compositional features of $MAPbI_3$ via VTD. As noted in previous literature on vapor deposition systems,[14,22] substrate temperature was seen to be an important factor in MAI sticking and therefore in $MAPbI_3$ formation, as shown by Fig. 11. The XRD patterns shown in this figure indicate an increasing relative intensity of the PbI_2 peak at $2\theta = 12.6^{\circ}$ relative to the $MAPbI_3$ peak with increasing

substrate temperature. These early experiments on substrate temperature allowed us to select a substrate temperature range appropriate for device growths and identified a handle to control perovskite film composition.

In addition to substrate temperature, underlayer was also observed to have an impact on film composition. As seen in the XRD patterns shown in Fig. 12, stoichiometric $MAPbI_3$ seems to form more easily on rougher underlayers such as ITO/TiO_2 compared to smoother underlayers such as glass. This observed composition difference illustrates a limitation with comparing VTD films grown on glass to films grown simultaneously on device underlayers and presents a challenge for obtaining meaningful time-resolved photoluminescence measurements on $MAPbI_3$ films grown on glass via VTD. Interestingly, a difference in PbI_2 morphology was also observed with different underlayers as highlighted in Fig. 8, potentially pointing to a connection between $MAPbI_3$ composition and PbI_2 orientation.

Previous work by UMN on Sn-based perovskites showed that film grain size can be controlled by system parameters such as chamber pressure and substrate temperature.[11] Additionally, there is evidence, both by UMN and in literature, that the relative ratio of the organic to the metal halide precursor can impact on grain size, with higher flux of organic precursor relative to metal halide

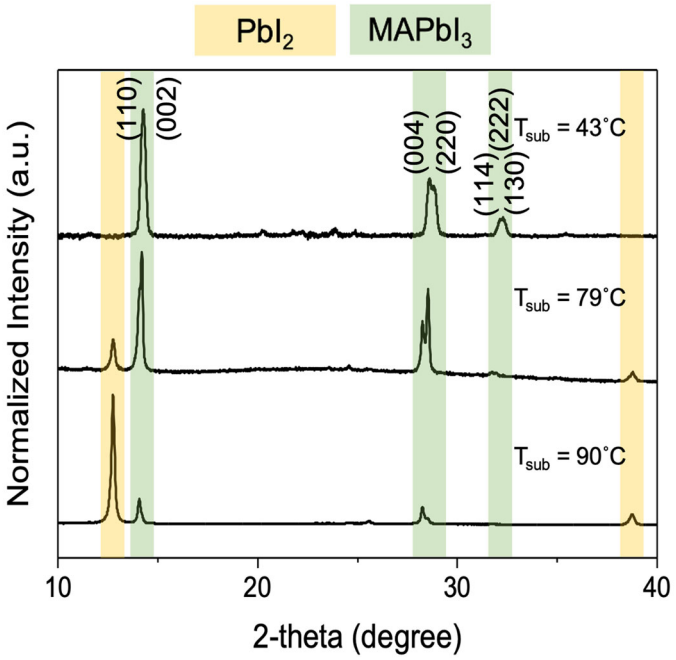

Figure 11: *XRD patterns for $MAPbI_3$ films grown on glass substrates at varying substrate temperatures. XRD patterns were taken using a Co-Ka source then adjusted to be relative to a Cu-Ka source. Patterns are normalized and offset for clarity.*

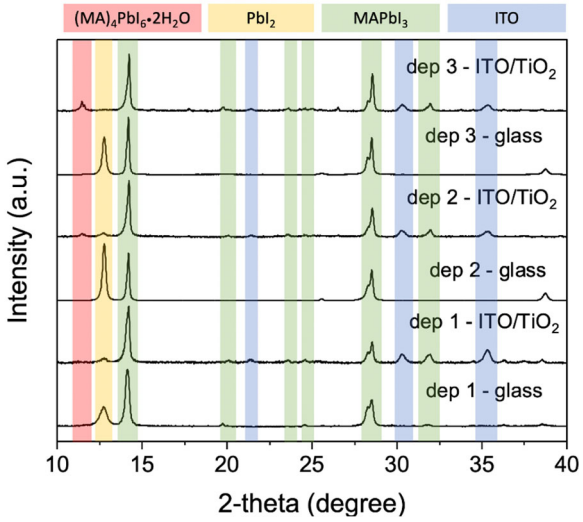

Figure 12: *XRD patterns for $MAPbI_3$ films grown via VTD on glass and ITO/TiO_2 substrates. XRD patterns were taken using a Co-Ka source then adjusted to be relative to a Cu-Ka source. Patterns are normalized and offset for clarity. Processing conditions for these films were chamber pressure = 2.6 Torr; deposition time = 30 minutes; MAI source temperature = 140˚C; PbI_2 source temperature = 355˚C; MAI carrier gas flow rate = 5 sccm; PbI_2 carrier gas flow rate = 5 sccm.*

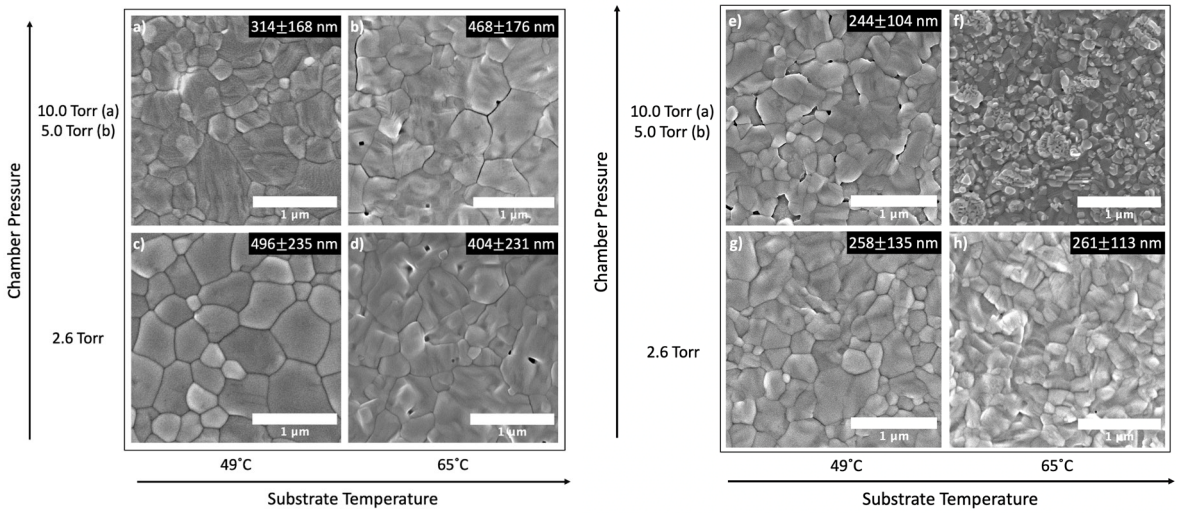

Figure 13: *(a-d) SEM images taken of $MAPbI_3$ films grown on glass substrates under varied chamber pressure and substrate temperature. Carrier gas flow rate and source temperature were kept constants for all 4 depositions. (e-h) SEM images taken of $MAPbI_3$ films grown on ITO/TiO_2 substrates under varied chamber pressure and substrate temperature. Carrier gas flow rate and source temperature were kept constant for all 4 depositions.*

precursor leading to larger grains. [22] Therefore, examining the morphology of $MAPbI_3$ films grown under varied operating conditions is of interest for identifying operating conditions for growth of $MAPbI_3$ films that lead to high power conversion efficiency in devices.

Film morphology and surface characteristics were examined via SEM for $MAPbI_3$ films grown on glass and ITO/TiO_2 under varied deposition conditions, as shown in Fig. 13. Overall, the trends indicate very little impact of processing conditions on grain size for $MAPbI_3$ films over the range examined, as indicated by Fig. 14. Films grown on ITO/TiO_2 substrates showed slightly smaller maximum grain sizes than those grown on glass, but the difference in average grain size caused by processing conditions was minimal, unlike previous results in the UMN system for Sn-based perovskites.[11] Three identical depositions were performed for each of the 6 processing conditions shown in Figures 13 & 14. These films showed consistent grain size across three identical runs, completing Milestone 1.2.2.

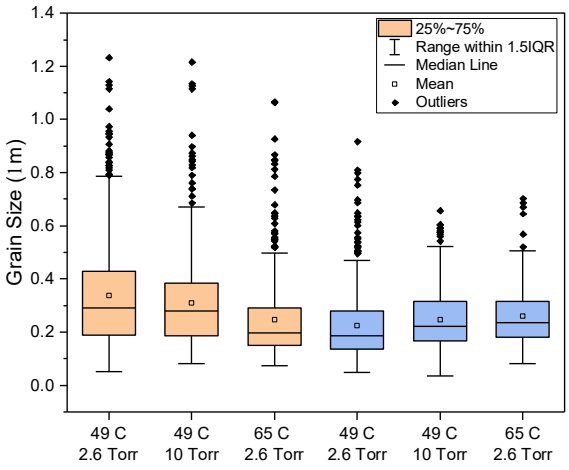

Figure 14: *Box and whisker plots showing estimated average in-plane grain size for films grown on glass and ITO/TiO_2 substrates under varied deposition conditions for the conditions shown in Fig. 11. Three runs were performed for each condition presented. Representative SEM images for each set of conditions are shown in Figure 12.*

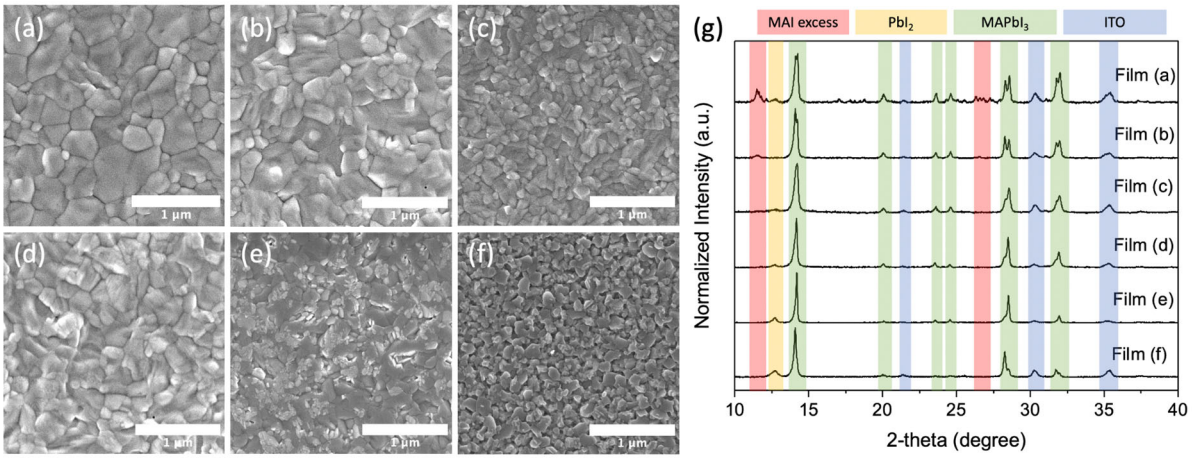

Figure 15: *(a)-(f) Top view SEM images of $MAPbI_3$ films grown on ITO/TiO_2 underlayers. (g) XRD patterns corresponding to the films shown in the SEM images. Films (a)-(c) were grown with a substrate temperature of 49˚C, and films (d)-(e) were grown with a substrate temperature of 65˚C.*

While processing conditions appeared to have minimal impact on film morphology for films with comparable stoichiometry, such as the ones shown in Fig. 13, film morphology was observed to change with changing stoichiometry. Figure 15 illustrates that films showing excess MAI (a & b) generally seem to have a larger grain size compared to those showing excess PbI_2 based on XRD patterns. In particular, Films e & f, which have the highest intensity of the PbI_2 peak at 2θ = 12.6˚ relative to the (002) $MAPbI_3$ peak at 2θ = 14.6˚, show a platelet like morphology at the film surface morphology, similar to the morphology of the pure PbI_2 films shown in Fig. 7 & 8.

The impact of processing conditions on composition and morphology shown in Fig. 15 was used to inform device depositions and was also shown to impact films on ITO/SnO_2 underlayers. The ability to control film composition, primarily via substrate temperature, was used to grow the films incorporated into devices under Task 2, and both morphology and film composition were observed to be linked to device performance.

In the MIT system, the deposition parameters used for the deposition of $MAPbI_3$ led to a higher growth rate, likely reflecting a reduced chamber pressure, of ~80 nm/min, with a linear dependence of thickness on deposition time (Fig. 16). This result indicates that thickness scales proportionally with temperature, making this an easy experimental knob to turn for varying thickness of $MAPbI_3$ films grown via VTD. The role of chamber pressure was also investigated in the MIT VTD system (Fig. 17). Similar to low pressure chemical vapor deposition[23] and to the results shown in COMSOL simulations discussed previously, we found that chamber pressure has a reciprocal relation to deposition rate, thus lower thickness was obtained under a higher pressure, for a fixed

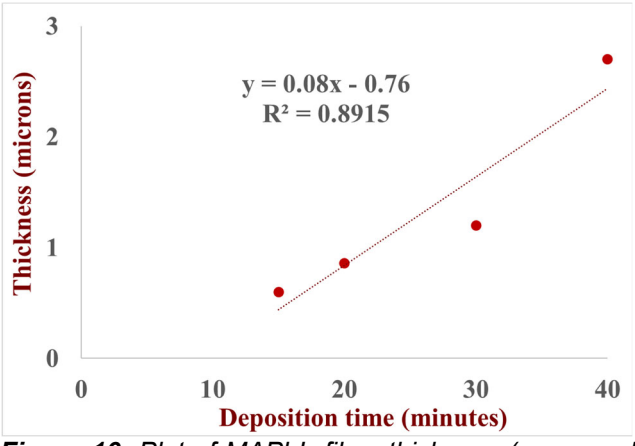

Figure 16: *Plot of $MAPbI_3$ films thickness (measured by profilometry) vs. deposition time.*

deposition time of 30 minutes. A potential explanation for this observation is related to the kinetic theory of gases: under low pressures, gas molecules have a lower tendency for collisions, their mean free path is higher which allows more time for acceleration, increasing their velocity. Hence, gas molecules under lower pressures diffuse and reach the substrate faster to form a thicker film in a shorter time. An alternative explanation could be related to the fact that under pressures lower than the standard atmospheric pressure, the sublimation temperature of a solid is reduced, as exemplified in the Clausius-Clapeyron equation. That can lead to higher precursor partial pressure at the source, leading to higher deposition rate on the substrate. Grain size for films grown in the MIT system is shown to have a weak dependence on chamber pressure. However, at the highest pressure tested, grains were in the sub-micron scale. Previous studies on hybrid halide perovskites have demonstrated that grain growth is equiaxial, and therefore can be limited by film thickness. Sub-micron grains are therefore expected for the ~100 nm film formed under a chamber pressure of 3 Torr.

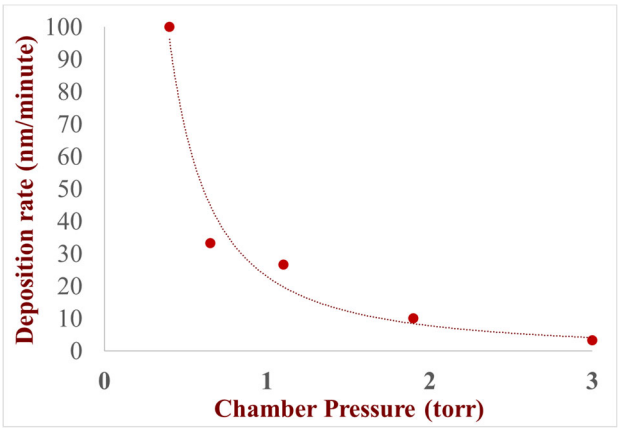

Figure 17: *$MAPbI_3$ deposition rate as a function of chamber pressure.*

The final consideration was to characterize $MAPbI_3$ film thickness uniformity within a given run and in terms of run-to-run thickness variations to facilitate device integration and address Milestone 1.4.2. Films grown on Si substrates in the UMN system were mapped using ellipsometry, with results for thickness variations between runs probed using profilometry for films grown on glass. We note that the films measured for thickness via profilometry had a deposition time of 60 minutes, while those shown in measured using ellipsometry were deposited in 30 minutes. The percent variation in thickness of these $MAPbI_3$ films across a 1x1 cm^2 region is <10% based on both profilometry and

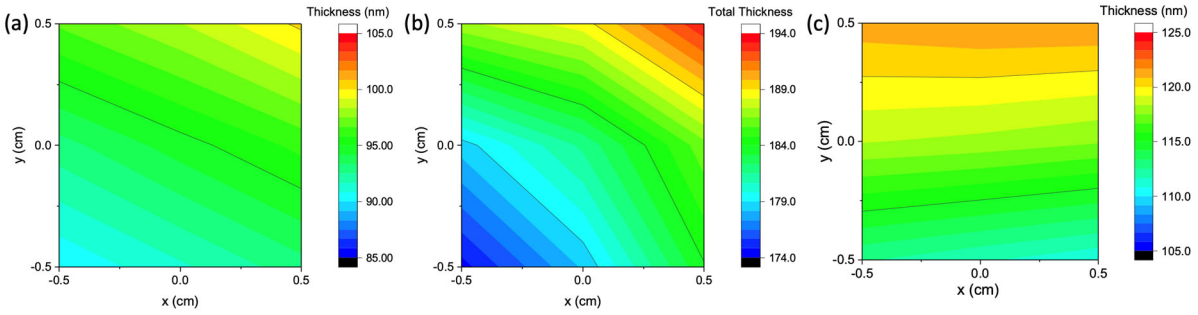

Figure 18: *Examples of thickness maps of $MAPbI_3$ films grown on silicon substrates. Thickness data was obtained using ellipsometry. Film (a) has an average thickness of 95 nm and a percent variation in thickness of 3.5%. Film (b) has an average thickness of 184 nm and a percent variation in thickness of 3.2%. Film (c) has an average thickness of 117 nm and a percent variation in thickness of 3.7%.*

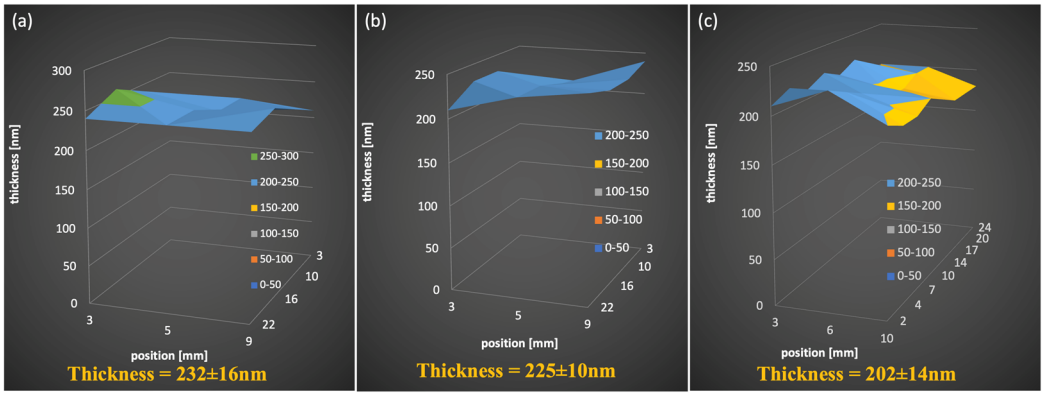

Figure 19: *Thickness maps for $MAPbI_3$ films grown on glass in the UMN system. Thickness data was obtained using profilometry at MIT. Film (a) has an average thickness of 232 nm and a percent variation in thickness of 6.8%. Film (b) has an average thickness of 225 nm and a percent variation in thickness of 4.4%. Film (c) has an average thickness of 202 nm and a percent variation in thickness of 6.9%.*

ellipsometry, and the run-to-run percent variation of the film thickness across three separate runs (Fig. 19) is 7.1% for the films measured via profilometry, completing Milestone 1.4.2 (see Fig. 18 and 19). The design rules developed for VTD processing of perovskites under this task supported our work in later developing VTD processed perovskite devices under Task 2.

Task 2.0: Establish the dependence of solar cell performance on perovskite film morphology by varying perovskite process conditions
Task Summary: This task will apply the processing understanding developed in Task 1 to characterize the dependence of perovskite optoelectronic performance on processing conditions. This insight will be used to design initial solar cells, while also informing the optimization of the back charge transport layer-perovskite interface to control layer morphology.

After improving our understanding of how to deposit MAPbI3 films with varying morphological and composition characteristics, we aimed to examine how these features impacted the electronic properties of our films. Figure 20a shows transient photoluminescence decays for perovskite films deposited using VTD on ITO/SnO2 substrates. These results suggest a longer carrier lifetime with increased PbI2 excess compared to stoichiometric films. Figure 20b shows the corresponding X-ray diffraction data for the films of Fig. 20a, confirming the variation in composition. The lifetime was measured under pulsed illumination at λ=405 nm, pumping from the air/perovskite interface, resulting in most of the measured photoluminescence originating at the top of the film. These films were processed on device relevant substrates, allowing for these results to provide further evidence that excess PbI2 processing conditions are improving optoelectronic properties.

After examination of the optoelectronic properties of films deposited via VTD, work focused on translating the films of Task 1 into vapor-deposited MAPbI3 solar cells. After examining very preliminary devices on unpatterned ITO and FTO substrates, UMN integrated a co-deposited VTD-processed MAPbI3 film into a solar cell with the

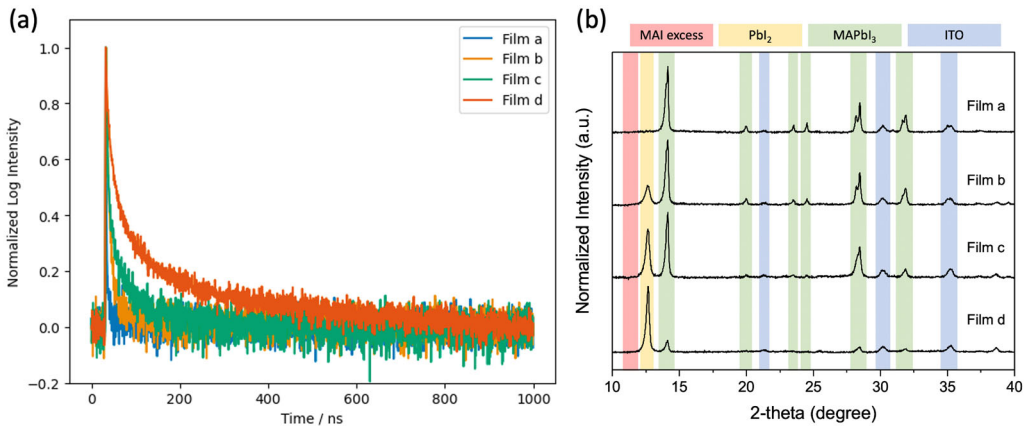

Figure 20: *(a) Time-resolved photoluminescence lifetimes for vapor-deposition perovskite films grown on ITO/SnO_2 with varying PbI_2 fractions. (b) XRD patterns for VTD perovskite films with varying PbI_2 fractions. XRD patterns were taken using a Co-Ka source then adjusted to be relative to a Cu-Ka source. Patterns are normalized and offset for clarity.*

architecture shown in Fig. 21a. In this device, patterned ITO was used as the transparent conductive oxide substrate followed by a ~40 nm thick electron-transport layer (ETL) of TiO2 that was spin coated on top of the ITO and then sintered at 500°C for 30 mins. MAPbI3 was VTD-processed on top of TiO2 layer, followed by a spin-coated hole-transport layer of Spiro-OMeTAD and a thermally evaporated electrode of Au.

The first attempt aimed to make a stoichiometric $MAPbI_3$ device (Device 1 in Fig. 21b). However, the external quantum efficiency (EQE) spectrum of the stoichiometric $MAPbI_3$ device was lower than 10% (Fig. 21c). To determine if this was due to the unoptimized transport layers or perovskite layer composition, $MAPbI_3$ with excess of PbI_2 was targeted since this composition is a widely used to passivate defects and improve device efficiency.[24,25] $MAPbI_3$ films with excess PbI_2 were made with the same processing

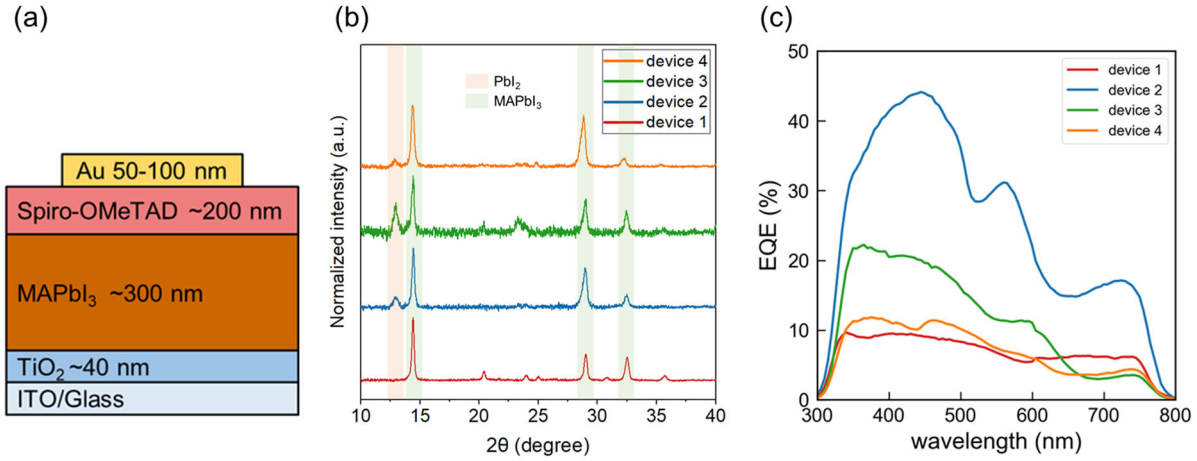

Figure 21: *(a) Device architecture of first trial VTD-processed perovskite solar cell. (b) X-ray diffraction (XRD) patterns and (c) External quantum efficiency (EQE) spectra of devices. The perovskite layer in Device 1 is stoichiometric $MAPbI_3$* and *PbI_2 excessive for Device 2~4. Processing conditions for these devices were chamber pressure = 2.6 Torr; deposition time = 30 minutes; MAI source temperature = 140˚C; PbI_2 source temperature = 355˚C; MAI carrier gas flow rate = 5 sccm; PbI2 carrier gas flow rate = 5 sccm. Chiller temperature for Device 1 was 20˚C and 5 ˚C for Device 2-4.*

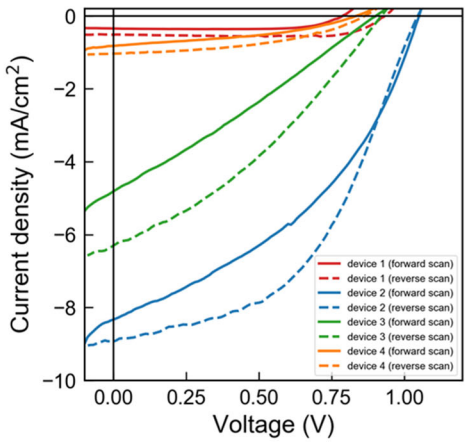

	$J_{sc,\ from\ EQE}$ (mA/cm²)	$J_{sc,\ from\ JV}$ (mA/cm²)	V_{oc} (V)	FF	PCE (%)
device 1	1.75	0.35 / 0.51	0.79 / 0.93	0.75 / 0.85	0.19 / 0.37
device 2	6.49	8.33 / 8.93	1.05 / 1.05	0.40 / 0.48	3.22 / 4.09
device 3	2.65	4.81 / 6.30	0.90 / 0.92	0.27 / 0.33	1.08 / 1.75
device 4	1.71	0.82 / 1.03	0.84 / 0.86	0.39 / 0.44	0.24 / 0.36

Figure 22: *Current density–voltage (J-V) curves of devices and operating parameters extracted from J-V curves and EQE spectra in Fig. 21. Two values separated by slash represent the resulting parameters from forward direction of J-V scan/reverse direction of J-V scan.*

conditions in three separate runs (Fig. 21b). Their EQE spectra (Fig. 21c) all show an onset at a wavelength of ~770 nm, corresponding to the bandgap (1.61 eV) of $MAPbI_3$. However, Devices 2 and 3 have two features at ~500 nm and 550-650 nm range in their EQE spectra. The feature at ~500 nm is attributed to the onset of PbI_2 absorption[25] and the other feature associated with the significant drop in EQE at around 570 nm is likely due to the thinness of the $MAPbI_3$ layer, [26] which means that the $MAPbI_3$ layer cannot efficiently absorb the light in this wavelength range. Therefore, Device 2 and 3 likely have thinner $MAPbI_3$ layers with excess PbI_2. Current density–voltage (J-V) curves of these devices under 1 Sun simulated illumination (AM1.5G) are shown in Fig. 22a (scan rate is ~260 mV/s). The stoichiometric $MAPbI_3$ device (Device 1) showed less than 1% power conversion efficiency (PCE) (Fig. 22b). The devices with excess PbI_2 showed improved EQE, open-circuit voltage (V_{OC}) and short-circuit current density (J_{SC}) compared to stoichiometric devices. The best device (Device 2 in Fig 21 and 22) had a PCE of 3.22% / 4.09% in the forward/ reverse sweep direction. It has been shown that excess PbI_2 can passivate defects, resulting in a higher V_{OC} and/or J_{SC}.[27] However, the impact of excess PbI_2 on device stability is still under debate and most of these works were based on solution processed perovskites.[27,28]

Although Devices 1 and 4 differ in composition (Fig 21c, stoichiometric vs. slightly PbI_2 excess), they showed comparable EQE and PCE (Fig 21b and 22). The unreasonably high fill factor ($J_{max} < J_{SC}$) for Device 1 is likely due to an unoptimized dopant concentration in the ETL and HTL. The series resistance (R_s), of device 1 and 4 is ~200-300 Ω cm^2. These R_s values are one order of magnitude larger than typical solution-processed $MAPbI_3$ devices and were later reduced.[29] This high series resistance likely reflects increased ITO electrode resistance due to the high temperature annealing required for TiO_2.

In this initial attempt to make VTD-processed perovskite devices, the stoichiometric $MAPbI_3$ device barely functioned (<1% PCE) however improved performance was realized by increasing the PbI_2 content in the perovskite thin film. Run-to-run variation of perovskite composition was also observed. Further improvements to the device performance required transport layer optimization, and better control of the $MAPbI_3$ film thickness, morphology, and composition in the VTD system.

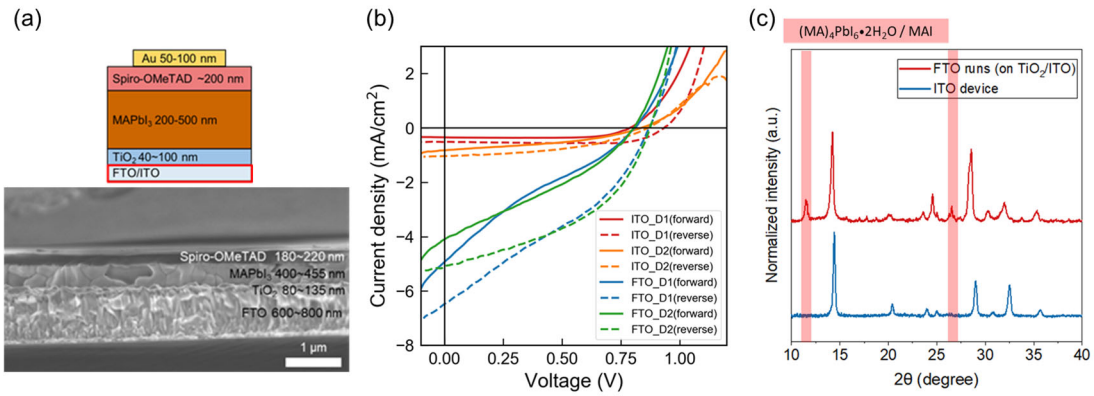

Figure 23: *(a) Device architecture of VTD-processed perovskite solar cell with ITO or FTO transparent conductive oxide (TCO) and cross section SEM image of FTO based device. (b) Current density–voltage (J-V) curves of ITO or FTO-based devices and (c) X-ray diffraction (XRD) patterns of ITO-based device and the perovskite film deposited on a separate TiO_2/ITO substrate alongside the FTO-based device. Processing conditions for FTO-based devices were chamber pressure = 2.6 Torr; deposition time = 60 minutes; MAI source temperature = 140˚C; PbI_2 source temperature = 355˚C; MAI carrier gas flow rate = 5 sccm; PbI_2 carrier gas flow rate = 5 sccm; chiller temperature = 5˚C*

To begin to address these issues, we considered different transparent conductive oxides (TCOs) and electron transport layers (ETLs). FTO was investigated as an alternative TCO material to avoid the potential increase in ITO resistance with TiO_2 annealing. It has been shown that the resistivity of FTO barely changes with annealing at <500°C.[30] Since EQE spectra from previous device runs suggested that the perovskite layers may also have been too thin, the deposition time was also extended to allow for a thicker device layer. Here, the deposition time was doubled compared to the ITO device results shown in Fig. 23b. The sticking of perovskite on different substrates is different and will result in different composition.[11] Since the FTO substrate is rougher than ITO, deposition parameters should be adjusted to make a similar composition and morphology film. A cross-sectional SEM image of an FTO-based device is shown in Fig. 23a, where the perovskite layer is 400~450 nm thick, dense, and without voids. The J-V curves are shown in Fig. 23b for the FTO device and compared to the ITO device previously described. The FTO-based device showed a significant J_{SC} increase, and a slightly lower V_{OC} compared to the ITO-based device. We also noted that the characteristic S-shape of the J-V curve of the FTO-based devices, potentially reflecting charge transport barriers at the absorber/contact interface.[31] Further characterizing the composition of the perovskite film deposited alongside the device by XRD (Fig 23c) showed that the perovskite layer incorporated into the device is slightly MAI excessive. Since MAI is an insulating material, the S-shaped J-V curve could be expected. Device efficiency over 3 runs (2 device pixels for each run) for both ITO and FTO is consistent and less than 10% variation, with the performance of FTO/TiO_2 devices exceeding the performance of ITO/TiO_2 for phase pure perovskite films, meeting Milestone 1.2.3. This is mainly due to the J_{SC} enhancement however, the FTO-based perovskite device efficiencies were still lower than 2%. As well as modifications to the device layer and architecture, UMN also upgraded the VTD system by installing a new chiller and shortening the substrate holder bar as part of an ongoing attempt to improve system control and film uniformity. As noted in Task 1, these improvements have improved control of perovskite film composition, uniformity, and reproducibility.

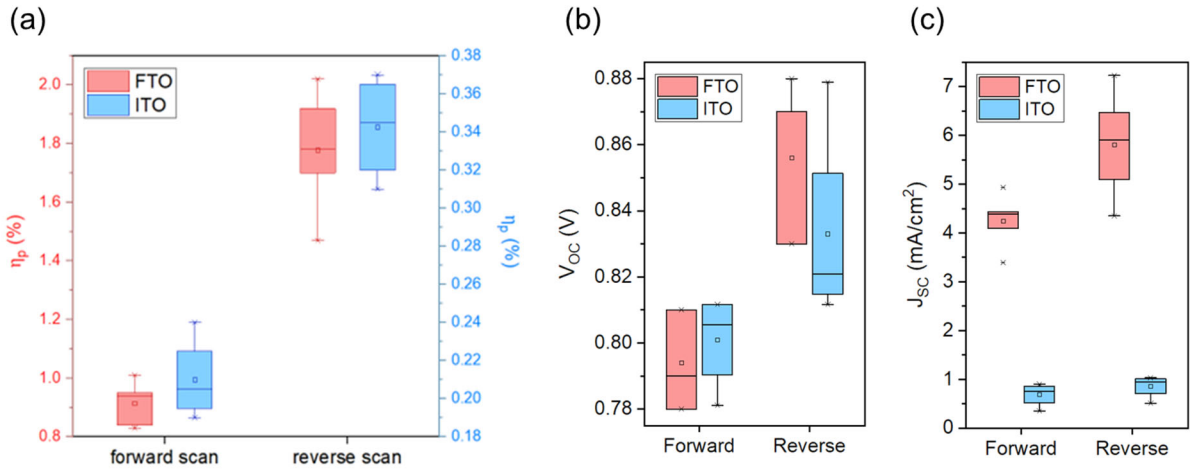

Figure 24: *(a) Power conversion efficiencies, (b) V_{OC} and (b) J_{SC} over 3 separate VTD runs (2 device pixels for each run) of ITO or FTO-based devices with the architecture in Fig. 23a.*

One of the key changes that ultimately led to improvements in VTD device performance was changing the ETL material from TiO_2 to SnO_2 with a small doping of TiO_2 nanoparticles. Incorporation of SnO_2 in the ETL layer contributes to high electrical conductivity and suitable band-level alignment at the electron transport layer (ETL)/perovskite interface, which has already been shown in the improvement of planar perovskite solar cell performance.[32] Therefore, UMN started to use a SnO_2/TiO_2 nanocomposite as the ETL based on a recipe developed at MIT. This change in ETL material allowed us to return to using the smoother ITO underlayer as our TCO in place of rougher FTO since SnO_2 only requires an annealing temperature of 150˚C.

In the UMN system, that substrate temperature strongly impacts MAI sticking and therefore the relative ratios of the MAI and PbI_2 precursors incorporated into the final perovskite film. Using this ability to manipulate PbI_2 excess via VTD, $MAPbI_3$ films with variable ratios of MAI to PbI_2 were grown for incorporation into devices. Film composition was probed using XRD. In considering device applications, composition was generally probed for films deposited on small ITO/SnO_2:TiO_x substrates mounted alongside the larger device substrates. The XRD patterns in Fig. 25a indicate a progression from a film that is MAI excessive, to a nearly stoichiometric $MAPbI_3$ film, to a PbI_2 excessive film.

To examine film continuity and suitability for integration into a device, top view film morphology (on ITO/SnO_2:TiO_x) was examined via SEM (Fig. 25b-e). As the relative ratio of PbI_2 to MAI increases, the morphology shifts from compact grains to a platelet-like morphology at the film surface, further suggesting PbI_2 excess in the film. In general as substrate temperature was increased, leading to films with more significant PbI_2 excess, an increasingly open platelet-like morphology developed at the top surface. Interestingly, this morphology does not closely resemble the morphology of the slightly lead iodide excessive solution processed $MAPbI_3$ film shown in Fig. 25e, nor does it resemble the morphology of other PbI_2 excessive films reported in the literature for both vapor and solution processing techniques. The platelets that appear at the surface of these films resemble those seen in pure PbI_2 films. This unique morphology motivates further study of the role of PbI_2 in VTD-processed films.

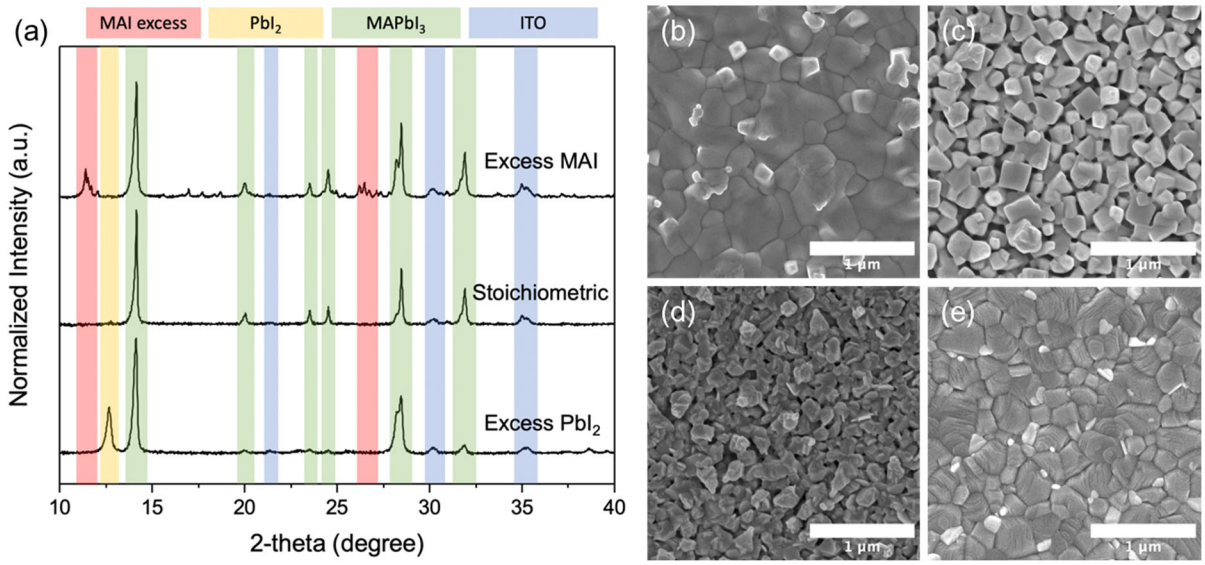

Figure 25: *XRD patterns and top view SEM images for films grown alongside a device growth on an ITO/SnO_2:TiO_x underlayer. (a) XRD patterns for $MAPbI_3$ films grown on an ITO/ SnO2:TiOx substrate. Top view SEM images of (b) MAI excessive film (c) stoichiometric film and (d) PbI_2 excessive film. (e) Top view SEM image of a solution processed $MAPbI_3$ film on an ITO/SnO_2:TiO_x underlayer.*

To fabricate the corresponding devices, the compositionally varying perovskite films were either VTD- or solution-processed on the SnO_2:TiO_x coated ITO substrate Devices had a total active area of 0.04 cm^2, and were tested with an illumination area of 0.018 cm^2. Fig 26a shows a device with perovskite layer (~240 nm) that is VTD-processed $MAPbI_3$ with excessive PbI_2 and Fig. 26b is one with a spin-coated perovskite layer (~330 nm). No visible voids pass through the electron- and hole-transport layer. Fig. 26c shows the J-V curves of the champion device for each composition in Fig. 26 as well as a spin-coated comparison device, measured under 1 sun illumination. For each device, a reverse sweep (1.2 to -0.1V) was collected before the forward sweep

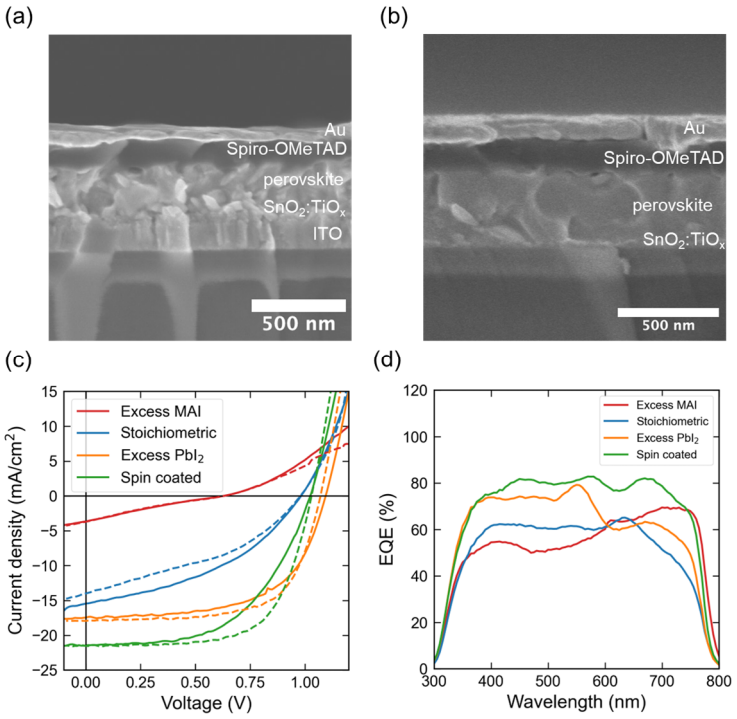

Figure 26: *Cross section SEM image of planar device architecture with (a) VTD-processed $MAPbI_3$ with excess PbI_2 and (b) spin-coated $MAPbI_3$ active layer. (c) J–V characteristics under 1-sun illumination and (d) external quantum efficiency (EQE) spectrum of the best stoichiometric, excess PbI_2 and spin coated $MAPbI_3$ devices. Solid lines and dash lines refer to forward sweep (-0.1 to 1.2 V) and reverse sweep (1.2 to -0.1 V) direction, respectively.*

direction (-0.1 to 1.2V) with a scan rate of 0.26 V/s. Table 1 summarizes device operating parameters including the J_{SC}, V_{OC}, FF and PCE for the champion devices. The best device incorporating a VTD-processed stoichiometric film, VTD-processed excess PbI2 film, and spin coated $MAPbI_3$ film yield PCEs of 4.86%, 11.53%, and 13.19% under reverse sweep, meeting Milestone 1.2.4. From these three different perovskite compositions fabricated by VTD, we clearly find that all the operating parameters improve with increasing PbI_2 content. A ~10% increase in V_{OC} was observed in excess PbI_2 devices compared to stoichiometric ones fabricated by VTD. It has been widely investigated in solution processed $MAPbI_3$-based solar cells that excess PbI_2 in the precursor solution can enhance the solar cell performance due to self-passivation at interfaces and between crystal grains of the perovskite, resulting in enhanced V_{OC}.[33,34] This result, taken with the time-resolved photoluminescence data of Figure 20 may suggest a role for PbI_2 in defect passivation for VTD films. Excess PbI_2 also results in higher J_{SC} as compared to the stoichiometric device.

Device EQE was measured to understand the difference in J_{SC} observed in these devices (Fig. 26d). While the EQE spectra for all devices show an onset at a wavelength of ~770 nm, corresponding to the bandgap of $MAPbI_3$, the EQE of the excess PbI_2 device is significantly reduced in 550-700 nm range, likely because the perovskite active layer is not sufficiently thick. In comparison, the spin-coated device has a ~330 nm thick perovskite layer, which is thicker than the VTD-processed PbI_2 rich film (~240 nm). This further suggests that the reduced EQE of the excess PbI_2 device in the near infrared is due to the thinner perovskite layer.

The operating parameters of additional excess MAI, stoichiometric, excess PbI_2 VTD-processed and spin coated devices are summarized in Fig. 27. The average efficiency over 10 excess PbI_2 VTD-processed devices across 3 separate depositions is 9.1±1.3% / 9.5±1.6% (forward sweep / reverse sweep), which is comparable to the spin coated devices (10.5±0.3 / 12.9±0.2) and less hysteretic.

To further examine the physical mechanism limiting efficiency, dark J-V characteristics were also assessed (Fig. 28a). The dark reverse sweep (1.2 to -0.1V) was collected before the dark

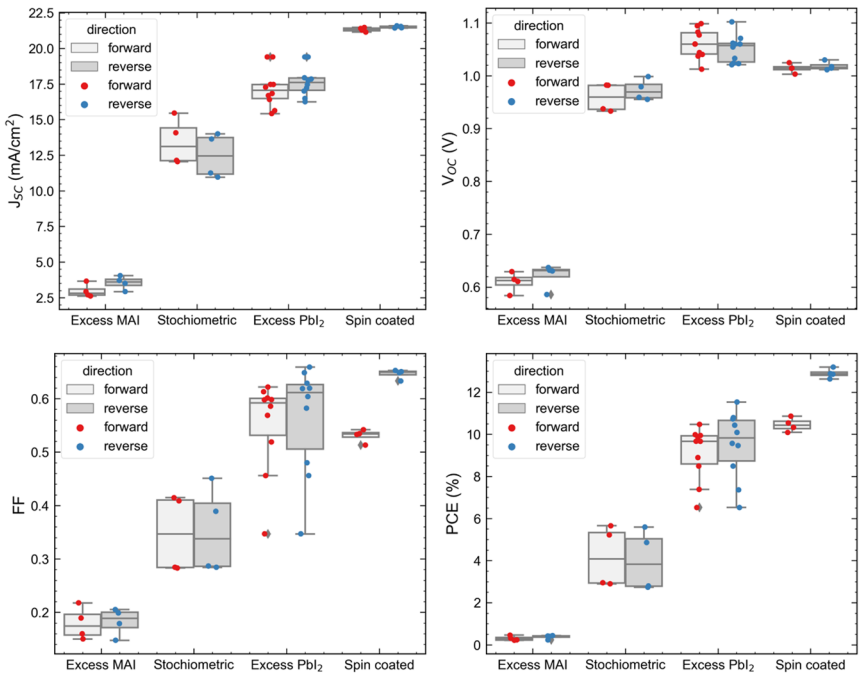

Figure 27: *Photovoltaic parameters for $MAPbI_3$ solar cell devices with different stoichiometry. There were 4 MAI rich devices, 4 stoichiometric and 10 PbI_2 rich VTD-processed and 4 spin coated MAPbI3 devices tested.*

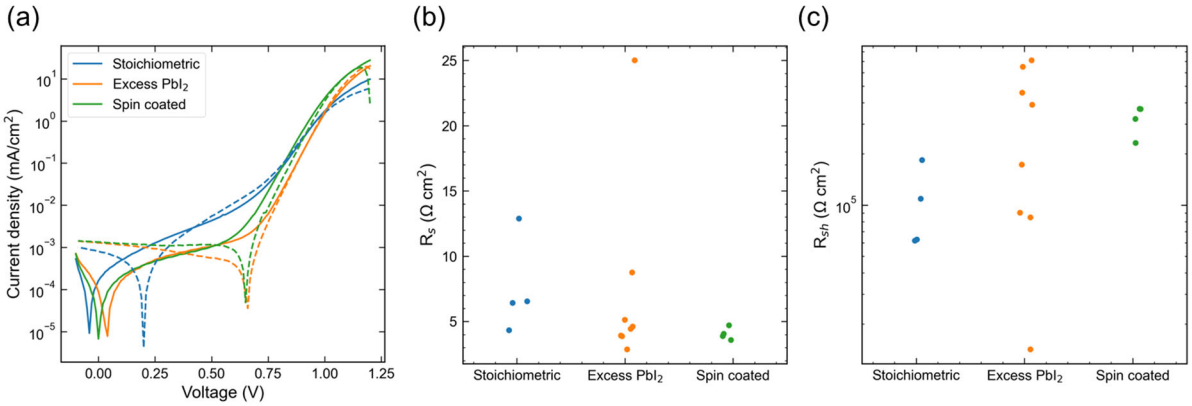

Figure 28: *(a) Dark J–V characteristics of the best stoichiometric, excess PbI_2 and spin coated $MAPbI_3$ devices. Solid lines and dash lines refer to forward sweep (-0.1 to1.2 V) and reverse sweep (1.2 to -0.1 V) direction, respectively. (b) series resistance (R_s) and (c) shunt resistance (R_{sh}) from the dark J-Vs under forward sweep fitted with the generalized Shockley equation. Dark J-Vs were collected from 4 stoichiometric and 8 excess PbI_2 VTD-processed and 4 spin coated $MAPbI_3$ devices.*

forward sweep (-0.1 to 1.2V). All devices showed some hysteresis in the dark. Series resistance (R_s) and shunt resistance (R_{sh}) were extracted by fitting the dark J-V curves under forward bias using the generalized Shockley equation (Fig. 28b and c). On average, the stoichiometric, PbI_2 rich, and spin coated devices have similar values of R_s of 7.55, 7.33, and 4.06 Ω cm^2 respectively. The average R_{sh} of stochiometric, excess PbI_2, and spin coated devices are 1.04×10^5, 3.21×10^5 and 3.22×10^5 Ω cm^2 respectively. The spin coated device showed the highest R_{sh}, which might be due to the larger, compact grains in the perovskite layer (Fig 25e) and the thicker perovskite layer, potentially reducing recombination or improving charge extraction. Excess PbI_2 VTD devices have a comparable R_{sh} to spin coated devices, but their grain size is much smaller and the perovskite layer is thinner. Stoichiometric VTD devices have a comparable grain size and thickness to PbI_2 excess VTD devices but show almost 1/3 shunt resistance of the excess PbI_2 VTD device.

The device performance as a function of illumination intensity was also probed on PbI_2-rich devices. This experiment was carried out several days after an initial J-V testing under 1 Sun illumination. The operating parameters extracted from J-V curves over 4 devices of illumination are summarized in Figure 29. Note that J_{SC} is nearly proportional to the illumination intensity and V_{OC} is linear with the logarithmic illumination intensity. The FF and PCE decrease with illumination intensity, likely

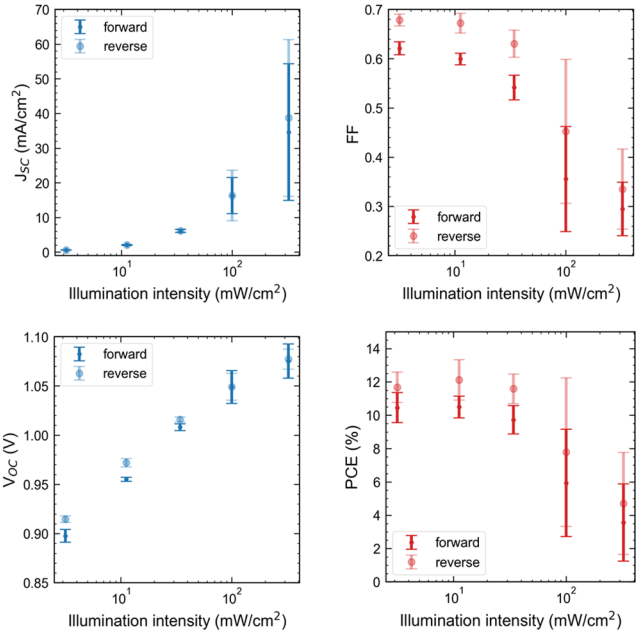

Figure 29: *Operating parameters as a function of illumination intensity for PbI_2 rich devices.*

reflecting increased recombination under higher illumination. Since the FF and PCE increase at lower illumination intensity, future work should include tracking this dependence as a function of perovskite film thickness.

Preliminary investigations of device shelf life and degradation under continuous illumination were also performed for champion devices. These results indicate that the devices degrade very little over a month in a glovebox and with periodic testing, indicating that current encapsulation is sufficient to prevent significant exposure to ambient conditions. Preliminary assessments of degradation under continuous illumination suggest that the champion devices degrade rapidly.

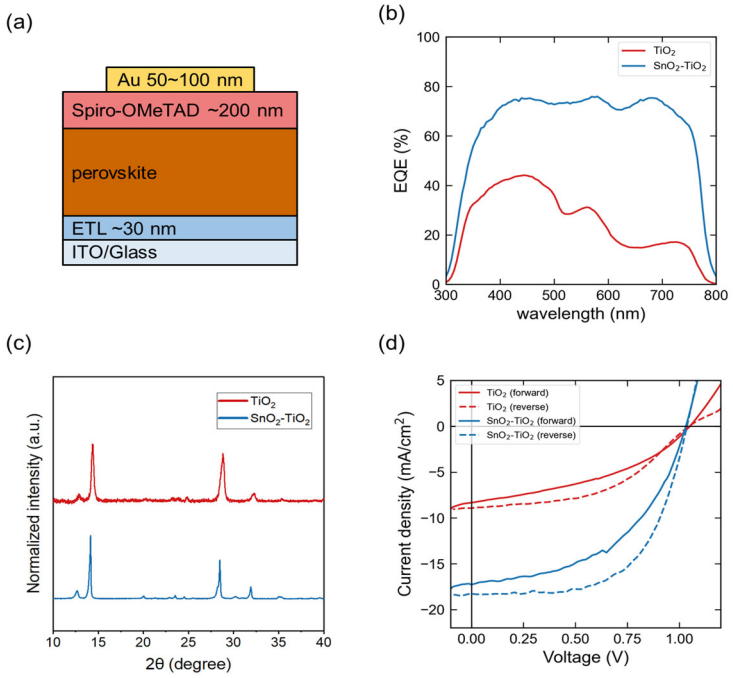

Figure 30: *(a) Device architecture, (b) EQE, (c) J-V curves under 1 sun illumination and (d) XRD of TiO_2 and SnO_2:TiO_x ETL devices.*

High efficiency structures were realized by switching from an electron transport layer of TiO_2 to one of SnO_2:TiO_x. We have previously showed that device efficiencies with ITO/TiO_2 were only 0.2-4%. A switch was made to SnO_2:TiO_x as the ETL (Fig. 30a) and the EQE and J-V comparison with TiO_2 ETL device are shown in Fig. 30b and 30c. Note that device with SnO_2:TiO_x shows increased EQE in the 500-700 nm range. In addition, the short-circuit current density (J_{SC}) has increased by nearly 50%, while the open-circuit voltage (V_{OC}) has not significantly changed. Given similar active layer compositions (Fig. 30d), the reason for increased EQE and J_{SC} may be due to the more optimized thickness, morphology or the surface roughness of the perovskite layer in SnO_2:TiO_x ETL device. While this result showed an excellent increase in efficiency, ultimately preliminary testing on these devices showed rapid drops in efficiency under MPPT testing, limiting our ability to meet Milestone 1.2.5.

To expand the range of transport layers available to the project, the MIT team worked to developed solution processed architectures that might be less prone to hysteresis. Here we compare three different device architectures, where the perovskite layer was spun cast, to achieve maximal reproducibility (Fig. 31). Different features come into play in different architectures: both n-i-p architectures are more hysteretic than the p-i-n architecture, whereas the last has the highest series resistance as well as shunt resistance. However, the devices based on Spiro-OMeTAD show the best performance with V_{OC} ~1.1 V and J_{SC} ~17 mA/cm^2, minimal series resistance and efficiencies of 12-14%. Keeping in mind that Spiro-OMeTAD is commonly deposited to a higher thickness

compared to other transport layers, one potential explanation for the better performance of devices based on Spiro-OMeTAD is that the thicker layer can accommodate more surface roughness in the underlaying perovskite film. These solution-processed devices fabricated at MIT were planned to be used to screen new transport layers and possible post-treatments to further optimize the device performance.

One approach to make further improvements in device performance is to employ transport layers already proven to yield high efficiencies in solution processed devices. To this end, specially formulated FTO/SnO_2 substrates were prepared at MIT and shipped to UMN. At UMN, a PbI2-rich perovskite layer was deposited and then shipped back to MIT. At MIT, devices were covered with Spiro-OMeTAD and capped with an Au top electrode and tested. J-V curves and the extracted operating parameters are summarized in Fig. 32. The efficiency of spin coating device with MIT's architecture is enhanced from 10-13% (obtained by UMN) to >16%. This result confirms the improved character of the transport layers. UMN's VTD device based on MIT's TLs also realized over 10% efficiency despite the transit delay when transporting UMN's perovskite layer to MIT and also the testing delay on a different characterization system.

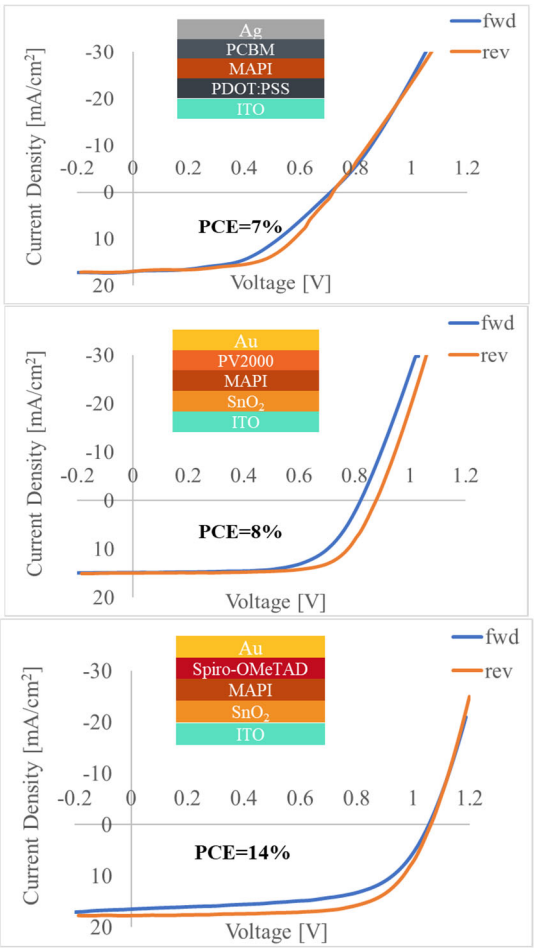

Figure 31: *J-V Curves for solution processed ITO/PEDOT:PSS/MAPbI₃/PCBM/Ag (top), ITO/SnO_2/MAPbI₃/PV2000/Au (middle), and ITO/SnO_2 /MAPbI₃/Spiro/Au (bottom) devices.*

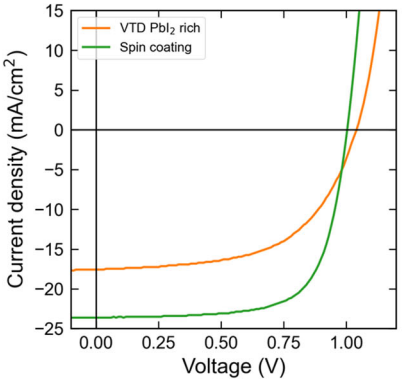

	VTD PbI_2 rich	Spin coating
J_{SC} (mA/cm²)	17.56	23.49
V_{OC} (V)	1.041	0.996
FF	0.57	0.69
PCE (%)	10.5	16.2

Figure 32: *J-V curves under 1 sun illumination and operating parameters of a solar cell with PbI_2 rich perovskite active layer deposited at UMN and transport layers processed at MIT.*

Task 3.0: Engineer perovskite-perovskite interfaces for interface stability and inclusion in devices
Task Summary: This task will exploit the unique processing advantages of vapor transport deposition to engineer perovskite-perovskite heterojunctions for application in solar cells. This task will include the processing of heterojunctions, examination of interface stability, and application in devices.

As efforts in BP1 evolved, it was clear that additional throughput was needed to control $MAPbI_3$ deposition via VTD and integrate these films into photovoltaic devices. As such, more effort was directed at realizing efficient devices based on $MAPbI_3$ to address project milestones tied to performance. This shift meant that there was insufficient effort to address Task 3.0 during BP1. This said, the use of dry-processing methods like VTD to integrate perovskite-perovskite interfaces into devices still holds promise, especially as more complicated multilayer, multijunction devices are considered. Perovskite transport layers could potentially offer increased stability compared to organic counterparts. While the use of VTD could remove solvent-use from processing and also overcome issues related to re-dissolving. As a result of this shift in effort, Milestone 1.3.1 was not completed.

Task 4.0: Enhancing device stability by targeting defects in vapor transport deposited films
Task Summary: Device stability will be engineered by more thoroughly considering the unique slate of defects common to vapor-deposited perovskite thin films, and engineering the perovskite-top charge transport layer interface for optimized device stability.

Work under this task focused on understanding the role of VTD in degrading MAI and the usefulness of solution-based passivation techniques to enhance film quality and device performance. One currently understudied aspect of vapor-based depositions is how depositional stresses integrate into the surface and bulk properties of films. In VTD, thermal stresses are likely to be the dominant factor creating defects. Thermal stress can be broken down into two unique processes as shown in Fig. 33, sublimation temperature and transfer zone temperature.

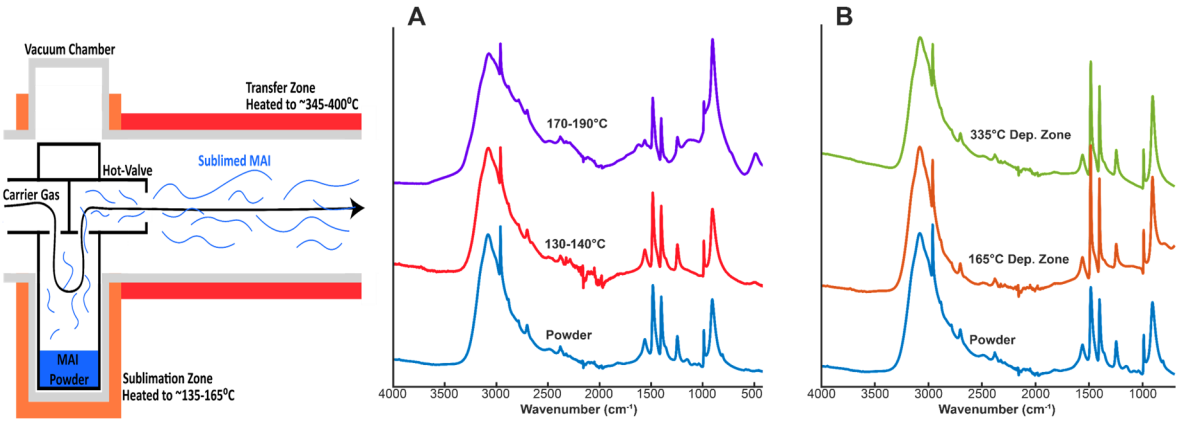

Figure 33: *Schematic of mass transport of MAI into the transfer zone of the MIT system. (a) Evolution of MAI FTIR powder signal as a function of sublimation temperature. (b) MAI FTIR powder signal if it is sublimed at the lower temperature but then experiences a brief period in a transfer zone at a variety of temperatures.*

Sublimation zone temperature corresponds to the thermal stresses the MAI powder experiences during sublimation. Building up a partial pressure of sublimed material is a balance between using a high enough temperature to get a high rate of sublimation with MAI degradation. In contrast, the transfer zone temperature is set by the temperature needed to keep PbI_2 in the vapor phase, and MAI only needs to survive a brief period of transit through the zone. To determine the impact of thermal stress on MAI used Fourier-Transform Infrared Spectroscopy (FTIR) on powders heated in the system and films of MAI that have passed through the heated zone.

Figure 33a shows the evolution of MAI powder as it experiences a variety of sublimation temperatures. Measured via powder FTIR-Attenuated Total Reflection (ATR), the bottom blue line corresponds to a fresh precursor powder before any sublimation treatments. The next two lines represent powders from sublimation boats after experiencing two different zones of sublimation temperatures. The red, lower 130-140°C FTIR-ATR curve is relatively similar to the baseline powder curve. The only dramatic appearance/disappearance of a peak is at 1153 cm^{-1} which appears in the baseline powder but not in the 130-140°C sublimation curve. Although further investigation is needed, the current hypothesis is that this is an organic contaminant that is being removed from the powder. In contrast, the 170-190°C sublimation curve shows significant changes, especially to the 1244 cm^{-1} and 1559 cm^{-1} peaks, which correspond to the C-N rock and asymmetric NH bend bonds respectively. The asymmetric NH bend especially shows the growth of two shoulders on either side of the bond. This likely corresponds to the increase in asymmetric variations to that bond structure.

Figure 33b shows how a powder evolves if it is sublimed at the lower temperature but then experiences a brief period in a transfer zone at a variety of temperatures. Here, we see no significant peak appearances/disappearances in any of the films or powders other than the previously mentioned 1153 cm^{-1} peak. This may indicate that the degradation experienced by MAI is more significant during the sublimation zone than the transfer zone. This work went towards addressing Milestone 1.4.1, however ultimately the milestone was not completed due to a shift in focus of the project.

The proposal in Subtask 4.2 to translate current solution-based passivation techniques to vapor processing was not explored. Given the large parameter space already intrinsic to VTD processing of $MAPbI_3$, the team chose to limit the introduction of additional process modifications and a further expansion in the parameter space. In the future, vapor-based passivation schemes might be best explored in VTD on solution-processed films with highly reproducible properties and performance. This would allow some vetting of the viability of VTD based passivation schemes and also enable a narrowing of the process parameter space before applying the same methods to perovskite films processed via VTD.

Post-deposition treatments of VTD perovskite films (Subtask 4.3) offer an avenue to possibly introduce additional ions into the perovskite and stabilize surface defect sites. The effectiveness of post-deposition treatments can be evaluated by probing the lifetime of excited carriers in the film through time-resolved photoluminescence experiments. Long carrier lifetimes indicate defect passivation, which can lead to improved charge-extraction in a solar cell device. Post-deposition treatments were performed on solution and VTD perovskite ($MAPbI_3$) films on glass by spin-coating dilute methylammonium chloride (MACl) or formamidinium iodide (FAI) solutions in isopropyl alcohol (IPA). Control lifetimes were taken for each film before the deposition to eliminate film to film variations in carrier lifetime. Control experiments of post-deposition treatments of pure IPA as well as post-deposition annealing were performed to deconvolute their effects on excited carrier lifetimes. Pure IPA with and without 100°C annealing for 10 minutes showed decreased average carrier lifetimes (Fig. 34), indicating that the treatment increased the density of defect sites. Treatments with 2 mg/mL of MACl in IPA without annealing resulted in improvements to the average carrier lifetimes, increasing from 5 ns before the treatment to 95 ns after treatment. An MACl post-treatment with annealing resulted in a decrease to the average carrier lifetime, from 28 ns to 12 ns. Similar concentrations of FAI in IPA with and without annealing showed no improvement to average carrier lifetimes. Clearly, annealing, pure IPA, and FAI are all poor post-deposition treatments that do not passivate defect sites in the perovskite film while MACl drastically increases carrier lifetimes.

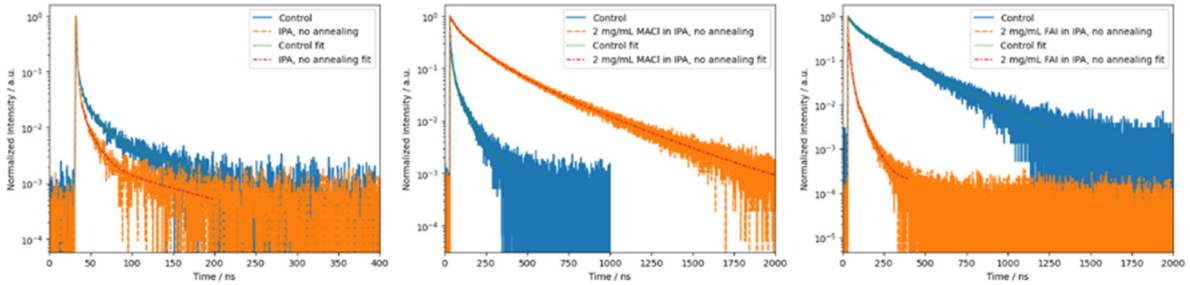

Figure 34. *Time-resolved photoluminescence traces of VTD MAPbI3 films with (a) an IPA wash without annealing (b) an MACl wash without annealing (c) and an FAI wash without annealing.*

To validate if MACl washing in IPA will lead to actual device performance improvements, the post-deposition treatment was performed on VTD and solution processed perovskite films on ITO with spincoated SnO_2 which were subsequently completed with Spiro-OMeTAD hole transport layers and a top Au electrode (Fig. 35). For the spin-coated (SC) devices, an increase in V_{OC} was observed after the MACl wash without annealing. No change in the Jsc was observed with only a marginal increase in power conversion efficiency. The increase in V_{OC} is further indicative of defect passivation from the MACl wash. No improvement was observed for VTD films treated with the MACl wash but the lack of a strict control device for comparison limits the conclusions that can be drawn. Post-deposition treatment may still be a viable path forward towards improving the carrier lifetimes of vapor-deposited perovskite thin films, especially since this work was carried out in an early stage of project device activities. Further device improvements have been made without the use of post-deposition washes, by further tuning the morphology and stoichiometry of the vapor-deposited perovskite or by moving towards a hybrid VTD/solution two-step process where the organic component is introduced by a solvent and the inorganic component is vapor deposited, as discussed in Task 6 .

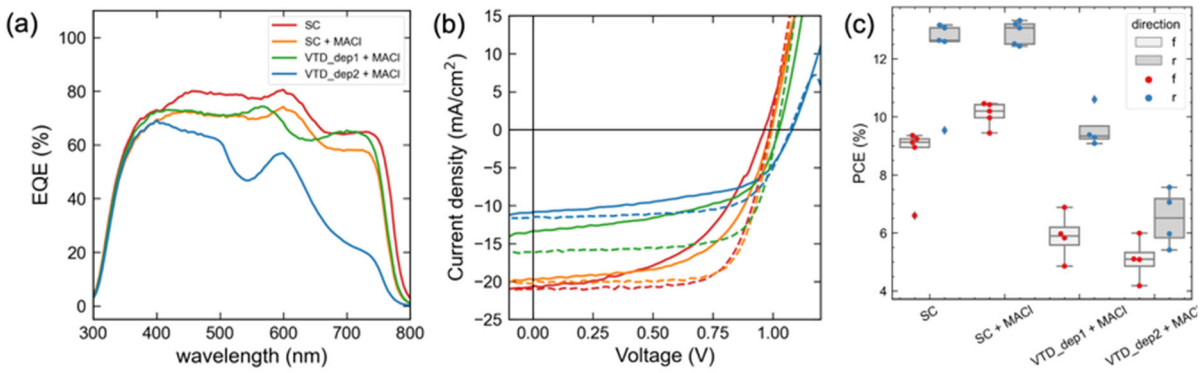

Figure 35. *(a) External quantum efficiency (EQE), (b) current-voltage (JV) curves, and (c) power conversion efficiency boxplots showing distributions of photovoltaic parameters for VTD and spin coated devices with and without an MACl wash without annealing.*

7.3 Results and Discussion - Budget Period 2 Tasks

Task 5.0: Demonstration of efficient solution-processed architecture to validate transport layers.

Task Summary: In moving beyond BP1 efficiency goals, demonstrate a solution-processed architecture capable of high efficiency to confirm viability of transport layers

and transport layer-electrode interfaces for testing of VTD perovskite absorber layer toward EOP-A efficiency goals.

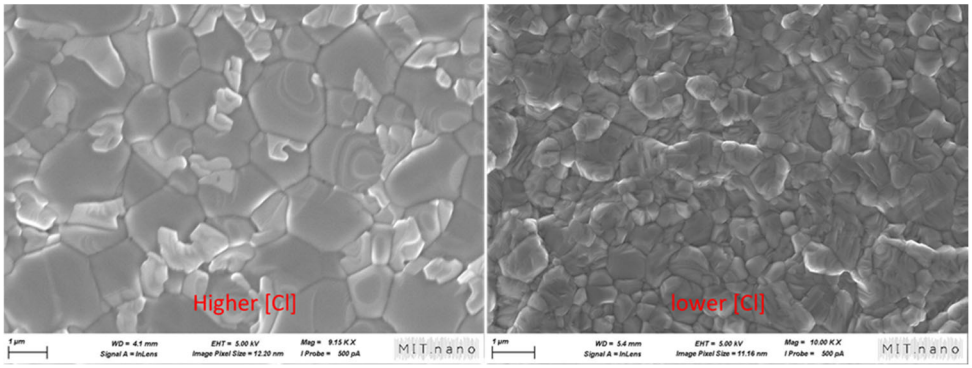

Figure 36: SEM imaging of 2-step processed FA1-XMAXPbI3(Cl) films, with high vs. low MACl concentration.

In order to support efforts to develop VTD based solar cells based, it was important to first demonstrate the ability to realize efficient solar processed architectures. Focused was on solution-based devices with an active layer of $FA_{1-x}MA_xPbI_3(Cl)$ in an architecture that has demonstrated applicability for the validation of devices with a VTD active layer. Specifically, perovskite precursor solutions were prepared in two separate vials: PbI_2 powder was dissolved in a mixture DMSO and DMF in a ratio of 1:9, to form a solution of 1.5 M. The organic precursors FAI and MACl (27mol%) were dissolved in IPA, to form a solution of 0.75M (calculated based on A-site cation concentration). The PbI_2 solution was spun first, followed by 1 minute anneal at 70˚C. Then, the organics solution was dropped dynamically (@2000rpm / 30s) and the film was annealed for 10 minutes at 150˚C. The entire procedure was performed in N_2 environment. Figure 36 presents a comparison of the microstructure yielded by the high (27 mol%) vs. low (9 mol%) MACl concentration in the organics solutions. It appears that higher Cl concentration contributes to grain growth, in agreement with other reports.

With successful incorporation of the organics into the PbI_2 film to form α-$FAPbI_3$, devices were constructed with an ITO cathode, SnO_2 electron transport layer, a spiro-OMeTAD hole transport layer, and a gold anode. Device performance was probed as a function of MACl concentration in the organics solution and compared to devices processed in the single step-processed devices, the results of which are summarized in Figures 37 and 38. Devices processed via the 1-step technique or 2-step technique (Figure 51) with a higher content of MACl exhibit good electronic

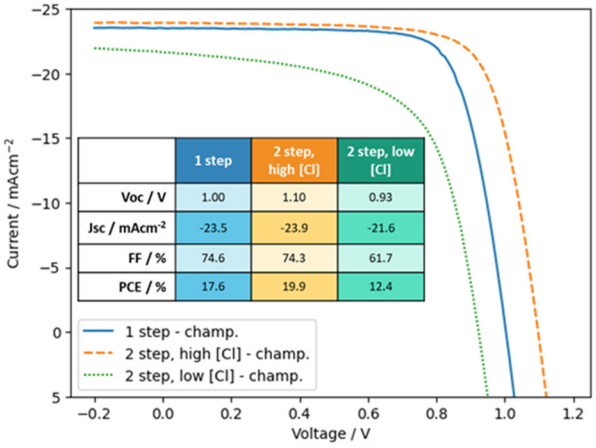

Figure 37: *JV curves of champion devices based on solution-processed $FA_{1-x}MA_xPbI_3(Cl)$.*

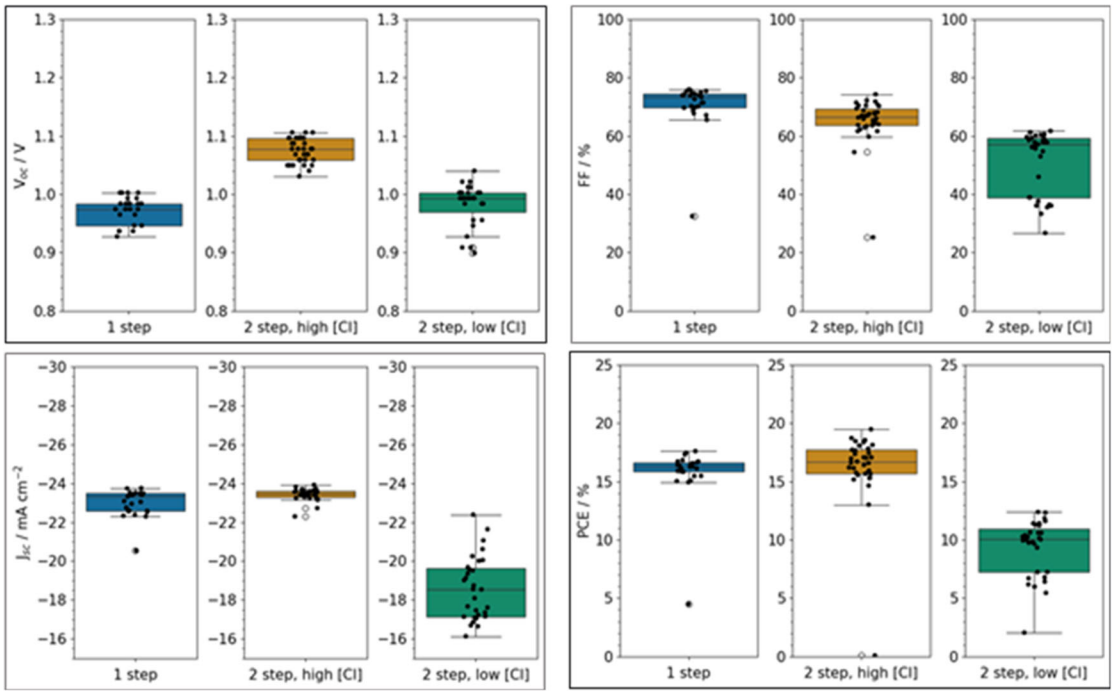

Figure 38: *(a) V_{OC} (b) FF (c) J_{SC} and (d) power conversion efficiency (PCE). Distributions collected on 12-24 devices of each group.*

characteristics, while those processed with a lower content of MACl gave poor performance. The first two (1-step and 2-step High [MACl]) demonstrated similar values of FF and JSC, with the devices processed via 1-step showing slightly lower V_{OC}. Devices based on the 2-step approach, with higher MACl concentration showed a champion efficiency of 19.9% under 1 Sun illumination, completing Milestone 2.5.1. However, 1-step devices showed the least variation from device-to-device in most parameters.

Task 6.0: Expanding perovskite composition in VTD-processed films for increased efficiency and stability.

Task Summary: Expand on BP1 efforts using MAPbI3 by including additional A- and/or X-site ions into the structure to enhance device efficiency and stability. Emphasis is on the use of FA-majority A-site perovskites.

This task has focused on how best to use VTD to deposit FA^+ cation-based perovskites. This ultimately required a rethinking of processing conditions as well as deposition approach (co-deposition versus sequential deposition). Here we discuss refining our ability to control film uniformity and composition with FA^+ cations, as well as measurements of film stability and degradation. Changes to the UMN VTD system and operating conditions significantly improved our ability to incorporate FA^+ cations into the perovskite. These included increasing the substrate temperature from ~75˚C for $MAPbI_3$ to around 121˚C for $FAPbI_3$, decreasing the dilution gas flow rate from around 220 sccm for $MAPbI_3$ to 150 sccm for $FAPbI_3$, and simultaneously increasing the FAI carrier gas flow rate from 5 sccm to 50 sccm. To better control the dilution gas flow rate, we also installed a mass flow controller on the line. Previously, the dilution gas flow had been controlled by a valve.

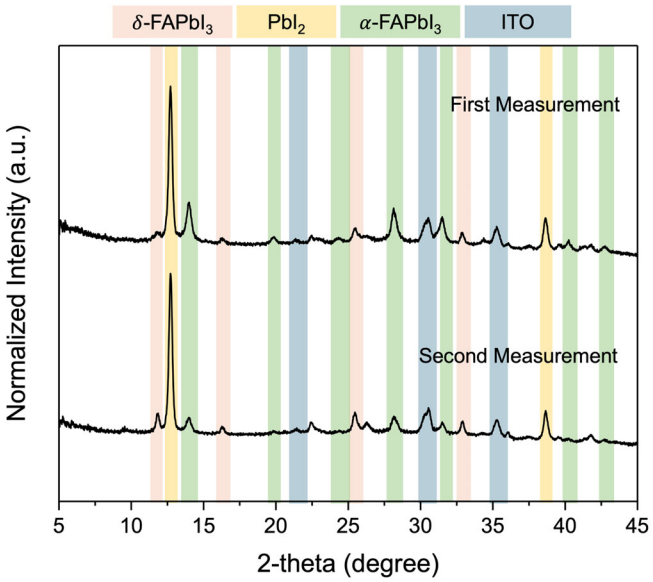

Figure 39. *XRD patterns for a co-deposited $FAPbI_3$ film. The top pattern was the first measurement taken on the film, while the lower pattern was a new measurement on the same film after roughly 15 minutes of exposure to ambient. The films show a significant PbI_2 excess and increased intensity of the undesired delta phase after exposure to the environment.*

In addition to these modifications, we also updated the processing scheme we were using. For the vast majority of our $MAPbI_3$ films, including all of those that were incorporated into devices, we used a co-deposition scheme. Co-deposition refers to simultaneously depositing the MAI and PbI_2 precursors to form our film. For $FAPbI_3$, we initially tried co-deposition but found that our films were highly PbI_2 rich. Because of this, we shifted to a sequential deposition scheme where we first deposited PbI_2 and then deposited FAI on top of it to form our final film. This technique seemed to work better and allowed for easier characterization of the FA^+ inclusion. We then further modified this technique to deposit FAI onto a film on $MAPbI_3$, to include MA^+ A-sites and maintain our desired cubic perovskite phase while working with $FAPbI_3$.

After modifying processing conditions such as substrate temperature, dilution gas flow rate, and carrier gas flow rate, the co-deposition option was revisited. The results shown in Figure 39**.** highlight that a sequential deposition scheme leads to better formation of α-$FAPbI_3$ compared to a co-deposition of FAI and PbI_2, even with more

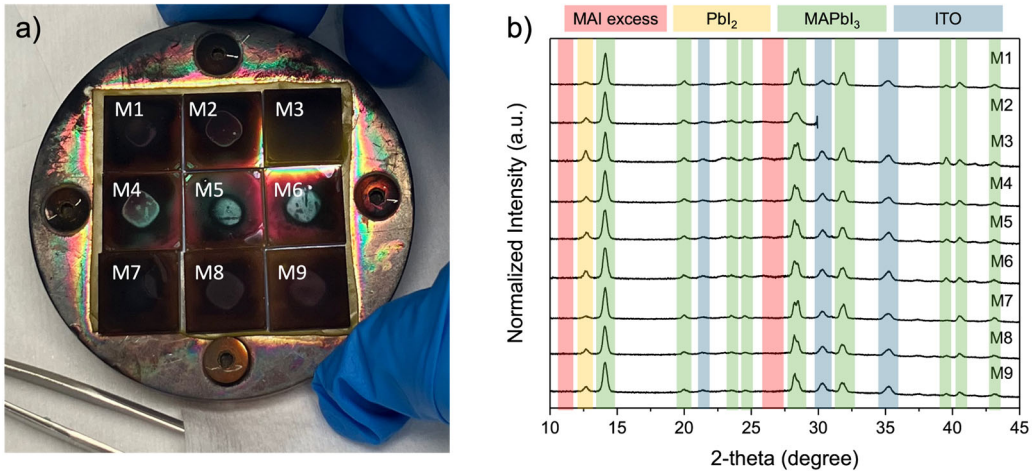

Figure 40. *a) Image of 9 $MAPbI_3$ deposited via VTD in the UMN system. All films were deposited on an ITO/SnO_2 underlayer. b) XRD patterns for the 9 $MAPbI_3$ films shown in a).*

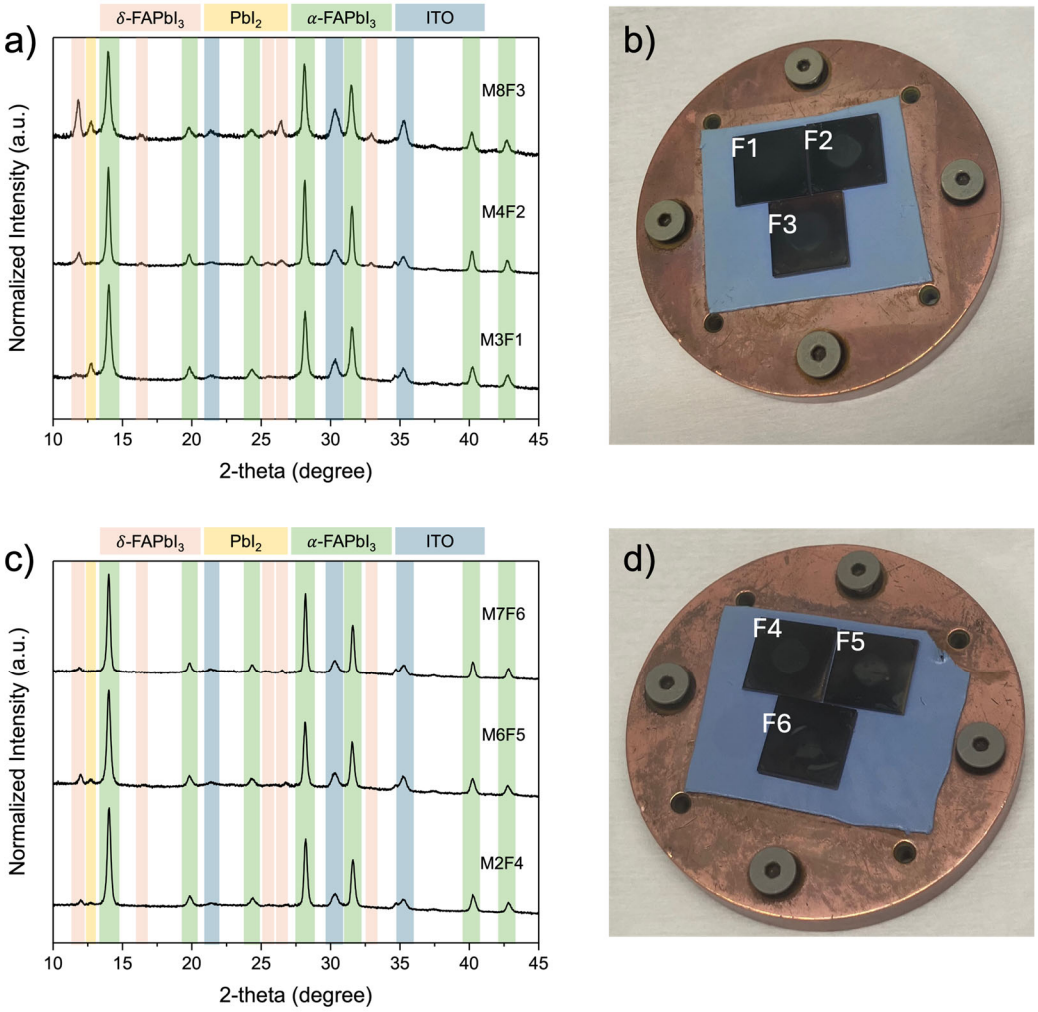

Figure 41. *a) XRD patterns for $FA_{1-x}MA_xPbI_3$ films grown using $MAPbI_3$ from Figure 8 and in the first FAI deposition. b) Image of VTD deposited $FA_{1-x}MA_xPbI_3$ films grown using $MAPbI_3$ from Figure 8 and in the first FAI deposition. c) XRD patterns for $FA_{1-x}MA_xPbI_3$ films grown using $MAPbI_3$ from Figure 8 and in the second FAI deposition. b) Image of VTD deposited $FA_{1-x}MA_xPbI_3$ films grown using $MAPbI_3$ from Figure 8 and in the second FAI deposition.*

optimized processing conditions. The film formed by co-deposition is highly PbI_2 rich and shifted relatively quickly to δ-$FAPbI_3$ after exposure to air during the roughly 15-minute measuring time for XRD. The two patterns are for the same film, taken 15 minutes apart. By comparison, sequential deposited films shown later in the report in Figures 40, 41, 43, and 24 showed a much higher intensity of the desired α-$FA_{1-x}MA_xPbI_3$

In addition to the co-deposition scheme, the issue of lateral and run-to-run variation was further probed. We first grew 9 $MAPbI_3$ films via VTD, as shown in Figure 40a. These films were then characterized by XRD, as shown in Figure 40b. The XRD patterns indicated mild variation in lead iodide content between the different films, but all films were observed to be PbI_2 rich. We also note that there is visible non-uniformity in the films. This is caused by the SnO_2 underlayer deposition method, where the films were first filtered

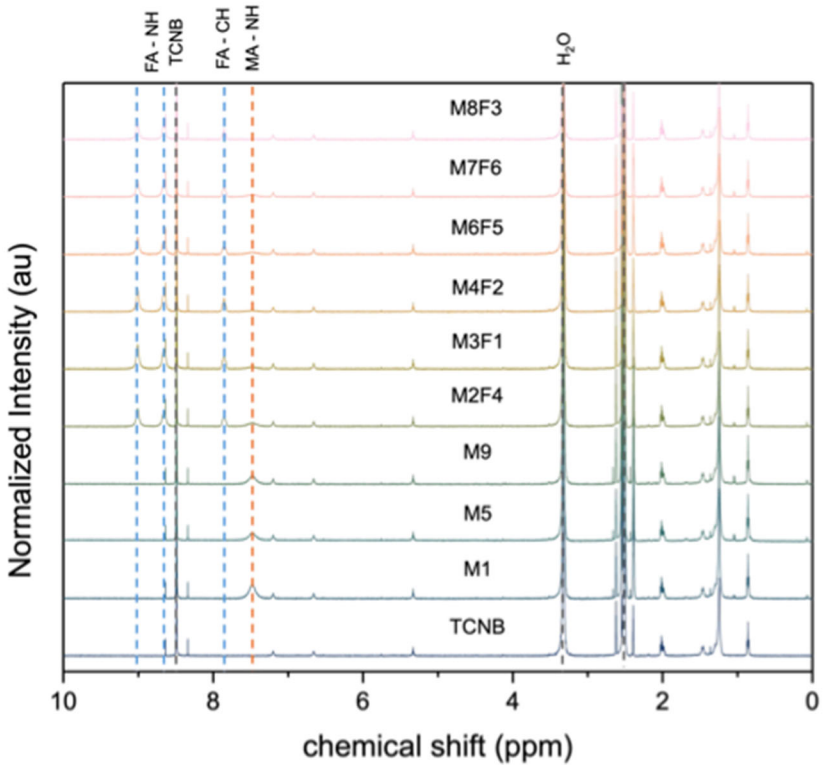

Figure 42. *NMR spectra of films the films shown in Figures 40 & 41. Films were dissolved in DMSO-d6 with TCNB. A-site proton peaks are integrated relative to the TCNB Reference peak. Peaks are labeled with their corresponding protons.*

Table 1. Integration data for NMR spectra shown in Figure 42.

Peak Location (ppm)	Peak Identity	M3F1	M4F2	M8F3	M2F4	M6F5	M7F6	M1	M5	M9
8.83	N-H (FAI)	0.579	0.631	0.474	0.489	0.404	0.472	NA	NA	NA
8.49	TCNB	1.00	1.00	1.00	1.00	1.00	1.00	1.00	1.00	1.00
7.86	C-H (FAI)	0.146	0.155	0.115	0.127	0.104	0.123	NA	NA	NA
7.43	N-H (MAI)	0.0614	0.0432	0.0071	0.118	0.0602	0.0819	0.403	0.283	0.263
2.39	C-H (MAI)	NA	NA	NA	NA	NA	NA	0.361(?)	NA	NA
3.35	H_2O	20.7	21.0	21.0	21.5	21.4	21.3	21.3	20.9	21.1
2.50	DMSO-d6	12.9	13.0	12.8	13.0	13.1	12.6	13.0	12.7	13.2
N-H / C-H in FAI integrals		3.96	4.07	4.13	4.13	3.87	3.85	NA	NA	NA
FA^+ / MA^+ ratio based on N-H		7.07	11.0	50.1	3.10	5.03	4.32	NA	NA	NA

then deposited using a pipette. For future depositions, the films were deposited directly through the filter, which eliminated this non-uniformity.

Three of these films (M1, M5, and M9) were set aside for characterization of the $MAPbI_3$ films. The other 6 films were used in two separate FAI depositions. The first FAI deposition used films M3, M4, and M8, as shown in Figure 41b. The second used films M2, M6, and M7. The deposition conditions between the two FAI runs were identical. XRD

patterns of both sets of films show evidence of some δ-$FAPbI_3$ formation, although the δ-$FAPbI_3$ peak appears stronger on the films grown in the first FAI deposition.

After XRD characterization, the films were dissolved in DMSO-d6 for characterization via NMR. The remaining $MAPbI_3$ films were also characterized via NMR. These results are shown in Figure 42 and summarized in Table 1. Films grown in FAI deposition 1 had 87.6%, 91.6%, and 98% FA in the A-site relative to MA. Films grown in

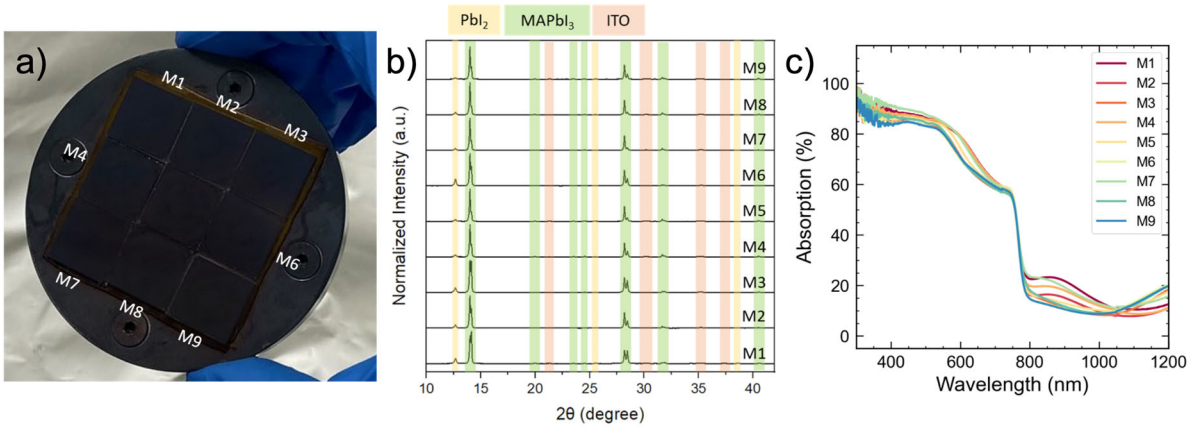

Figure 43. *a) Image of $MAPbI_3$ films grown on ITO/SnO_2 with the intention of producing higher thickness $MAPbI_3$. b) XRD patterns for the 9 $MAPbI_3$ films shown in a. c) UV-Vis absorption data for the 9 films shown in a.*

FAI deposition 2 had 75.6%, 83.4%, and 81.2% FA in the A-site relative to MA. Additionally, film M1 had a higher MA signal relative to the TCNB standard than films M5 and M9, suggesting that there is some variation in sticking of MAI in the initial $MAPbI_3$ deposition. This result helped us realize that the variation in A-site ratio was in a large part due to the underlying $MAPbI_3$ films. However, these results also demonstrated quantitatively the ability to form mixed A-site films meeting Milestone 2.6.1.

To obtain films with a better controlled FA/MA ratio in the A-site, we decided to target slightly thicker $MAPbI_3$ films for our underlayers, with the idea that having more MA^+ initially deposited would cause less variation in the amount of MA burned out and allow us to obtain a more consistent FA/MA ratio. Additionally, the NMR results shown in Table 1 did not indicate that the amount of FA in the film relative to TCNB was varying dramatically. We also observed from the XRD data in Figure 41a and c that the films that contained some degree of PbI_2 excess seemed to remain in the alpha phase longer and showed less evidence of shifting to the undesired delta phase. With this in mind, we targeted a thicker $MAPbI_3$ growth with PbI_2 excess for our next sequential deposition. An image of these $MAPbI_3$ films, XRD data, and UV-Vis data for these thicker films is shown in Figure 43.

FAI was then deposited on 6 of these films in two separate depositions with the goal of converting the films to mixed A-site $FA_{1-x}MA_xPbI_3$ perovskite. XRD and UV-Vis data for these 6 films is shown in Figure 43. Overall, these films showed a slight red-shift in absorption onset in UV-Vis, disappearance of the peak at 23˚ 2-theta in XRD, and

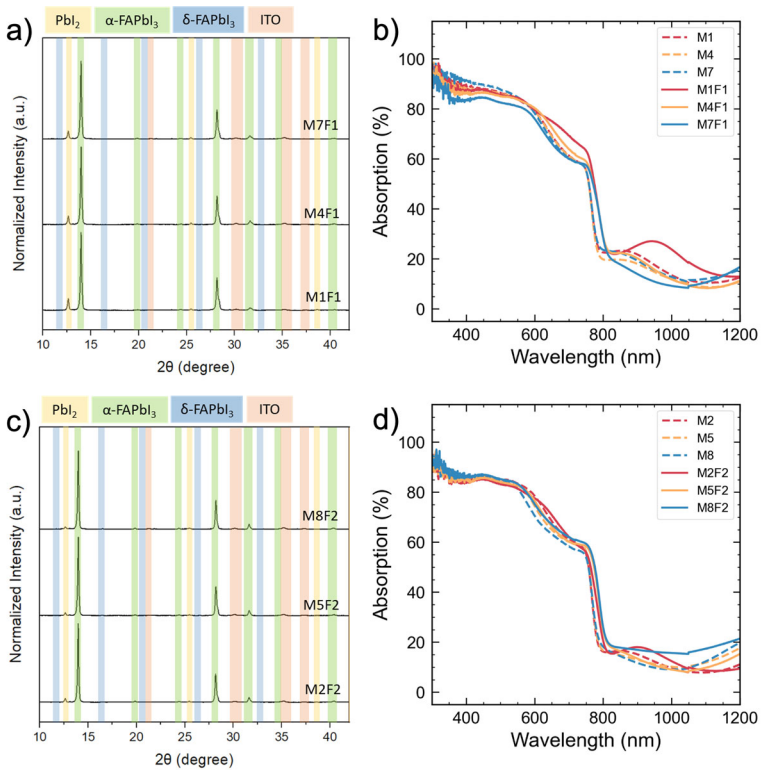

Figure 44. a) XRD patterns for $FA_{1-x}MA_xPbI_3$ films grown in the first FAI deposition. b) UV-Vis data for $MAPbI_3$ films before and after conversion with FAI deposition 1. c) XRD patterns for $FA_{1-x}MA_xPbI_3$ films grown in the second FAI deposition. d) UV-Vis data for $MAPbI_3$ films before and after conversion with FAI deposition 2.

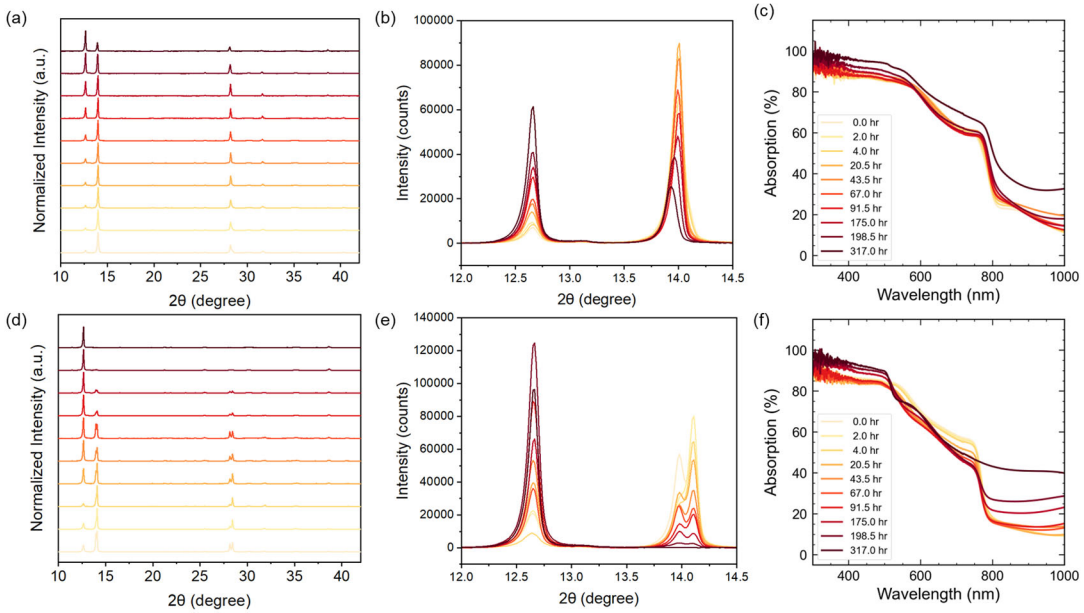

Figure 45. (a) Normalized XRD patterns, (b) zoomed in XRD patterns and (c) UV–vis absorption spectra of the $FA_xMA_{(1-x)}PbI_3$ film on SnO_2:TiO_x/ITO as a function of aging time on 85˚C hot plate. (c) Normalized XRD patterns, (d) zoomed in XRD patterns and (e) UV–vis absorption spectra of the $MAPbI_3$ film on SnO_2:TiO_x/ITO as a function of aging time on 85˚C hot plate.

change from a split peak at 28˚ 2-theta to a single peak at that angle. All of this was

evidence that FA^+ was incorporated. Additionally, the films showed a peak indicating PbI_2 excess which is promising for their stability based on the data in Figure 41. Because of this, we stability tested these films on a hot plate, and used these deposition conditions to deposit films for VTD based devices.

Initial thermal stability of vapor-deposited $FA_xMA_{(1-x)}PbI_3$ (converted from $MAPbI_3$) and $MAPbI_3$ film was investigated at controlled elevated temperatures of 85°C. This assessment is to mimic ISOS-D-2 protocol, but to learn more fundamentally on the perovskite composition before completing the full device stack. XRD patterns and absorption spectra were collected periodically, otherwise films were aged on the hotplate in a N_2-filled glovebox for the rest of the time. As-synthesized $FA_xMA_{(1-x)}PbI_3$ and $MAPbI_3$ films were both slightly PbI_2 excessive (Figure 44a and d), but $MAPbI_3$ film turned into PbI_2 dominated after 43.5 hours aging and 198.5 hours for $FA_xMA_{(1-x)}PbI3$ film. The (001) peak at 14° 2θ in $FA_xMA_{(1-x)}PbI_3$ film gradually shifted to 13.94° 2θ during the aging and the intensity decreased, with PbI_2 peak (12.7° 2θ) intensity increased (Figure 45b). Absorption onset of $FA_xMA_{(1-x)}PbI_3$ film also shifted to longer wavelength (Figure 45c). These results both suggest that MA might be gradually burned out during the aging process. NMR will be used to quantify the MA:FA ratio by the end of this assessment. As

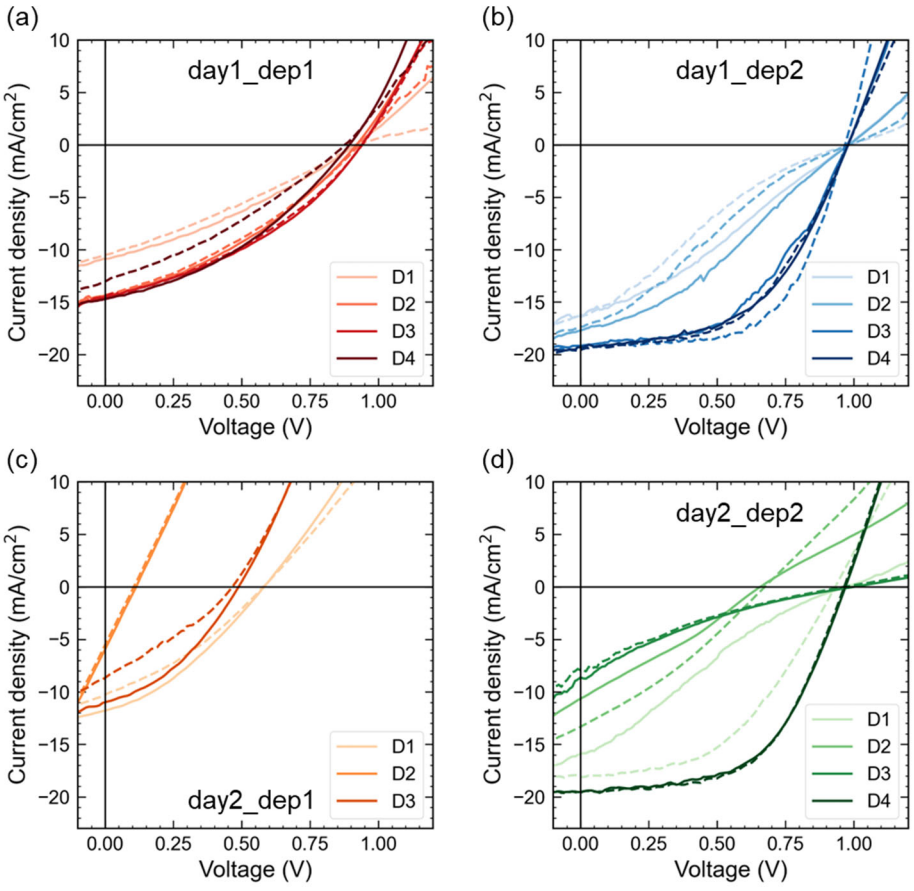

Figure 46. Current density–voltage characteristics under 1 sun illumination for $FA_{1-x}MA_xPbI_3$ devices for 4 separate VTD runs from (a) day1_dep1, (b) day1_dep2, (c) day2_dep1, (d) day2_dep2. Solid lines and dash lines refer to forward sweep (-0.1→1.2 V) and reverse sweep (1.2→ -0.1 V) direction, respectively.

for $MAPbI_3$ film, there is a peak splitting at ~14° 2θ, indicating the tetragonal phase (Figure 45e). Similarly, the perovskite phase peak intensity decreased with the PbI_2 peak intensity increased. After ~300 hours aging the film turned into pure PbI_2 film, which is confirmed by XRD and absorption spectrum (Figure 45e and f). From these preliminary results, the degree of PbI_2 excess seemed to impact the kinetics of phase transition and degradation differently if the MA:FA ratio is different.

Devices based on $FA_{1-x}MA_xPbI_3$ films were deposited on pre-patterned ITO substrates coated with a ~40 nm thick electron-transport layer (ETL) of SnO_2:TiO_x. A PbI_2 excessive layer of $MAPbI_3$ was formed via co-deposition, followed by FAI deposition. A hole-transport layer of Spiro-OMeTAD (100~150 nm) was spun-cast onto device substrates followed by a thermally evaporated electrode of Au (100 nm). Devices had a square geometry defining an active area of 4 mm^2. Four separate VTD runs were conducted on two different days, and two VTD runs were performed on each day. The naming nomenclature is as follows, the first deposition on day 1 was denoted as day1_dep1. Each deposition has 4 device pixels, and they are denoted as D1-D4 from top to bottom. Current density–voltage (J-V) characteristics of these devices under 1 Sun simulated illumination (AM1.5G) are shown in Figure 46. The operating parameters of these devices extracted from Figure 46 are summarized in Figure 47. Dep1 devices from each day showed poorer performance as compared to devices from dep2, especially in short-circuit current (J_{SC}) and fill factor (FF). This might be due to the fact that

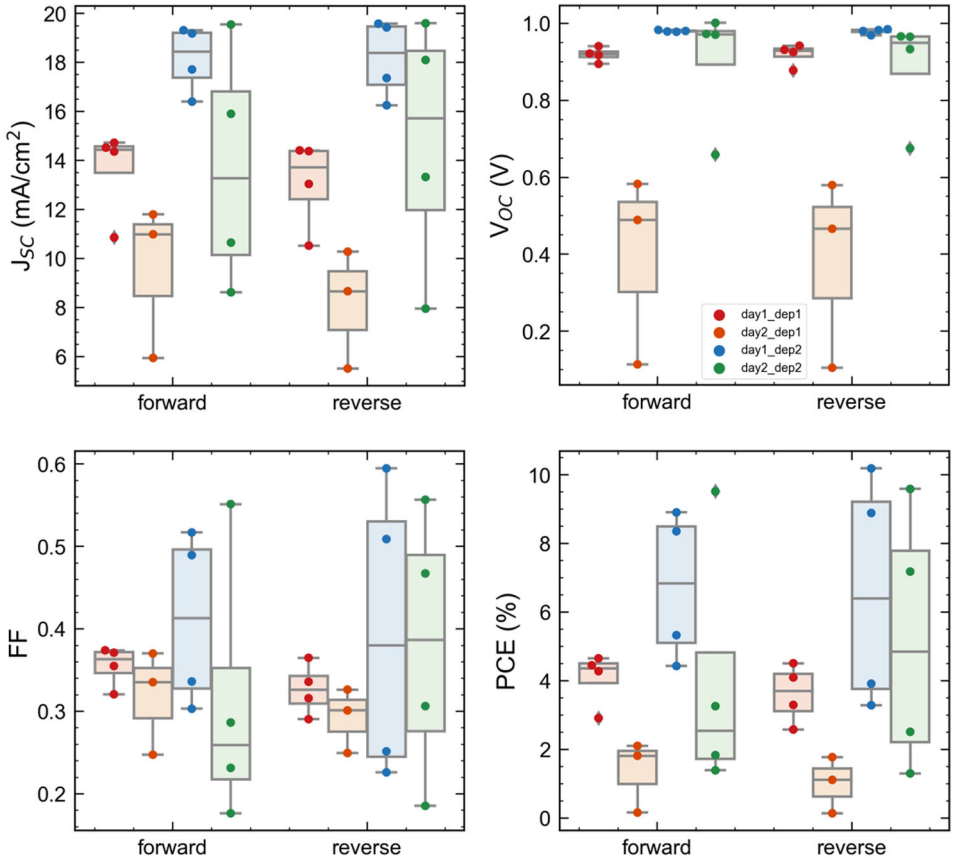

Figure 47. Boxplots showing distributions of photovoltaic parameters (J_{SC}, V_{OC}, FF and PCE) extracted from Figure 18.

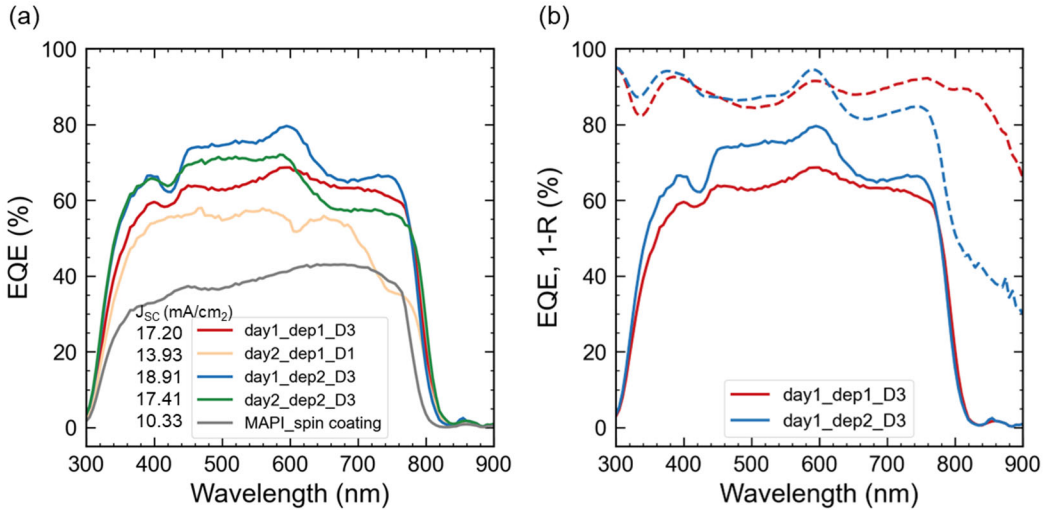

Figure 48. (a) External quantum efficiency (EQE) spectra for $FA_{1-x}MA_xPbI_3$ and solution processed $MAPbI_3$ devices. (b) Comparison of EQE spectra and reflection spectra (denoted as 1-R, broken lines).

stoichiometric VTD-processed perovskites tend to have cubic-like crystals with many gaps in between grains on the top surface.[17] Champion devices from day1_dep2 showed J_{SC} of 19.17/19.42 mA/cm^2 (forward/reverse sweep), open-circuit voltage (V_{OC}) of 0.98/0.97 V, FF of 0.49/0.59 and power conversion efficiency (PCE) of 8.35/10.18%. The series resistance (R_s) and shunt resistance (R_{sh}) extracted at J_{SC} and V_{OC} are 17.3/10.7 and 356.2/212.1 (forward/reverse sweep) Ω cm^2, respectively. Champion devices from day2_dep2 showed J_{SC} of 19.54/19.59 mA/cm^2 (forward/reverse sweep), V_{OC} of 0.97/0.97 V, FF of 0.55/0.56 and PCE of 9.51/9.58%. R_s and R_{sh} extracted at J_{SC} and V_{OC} are 13.9/14.0 and 424.7/1067.5 Ω cm^2, respectively. Although some devices from dep2 showed reproducible results, there is a larger spread from pixel to pixel. While this data began to address Milestone 2.6.2, ultimately this milestone was not met.

Device external quantum efficiency (EQE) was also probed on one device pixel from each run. A solution-processed $MAPbI_3$ device was also fabricated using the same

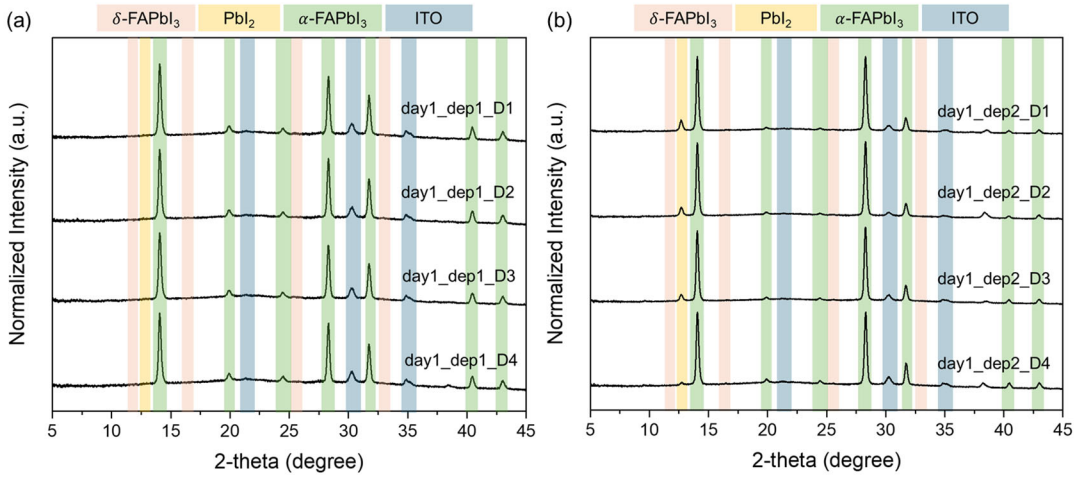

Figure 49. XRD patterns of $FA_{1-x}MA_xPbI_3$ devices from (a) day1_dep1 and (b) day1_dep2. Data were acquired using a point source XRD and focused on actual device pixels after peeling off gold electrode.

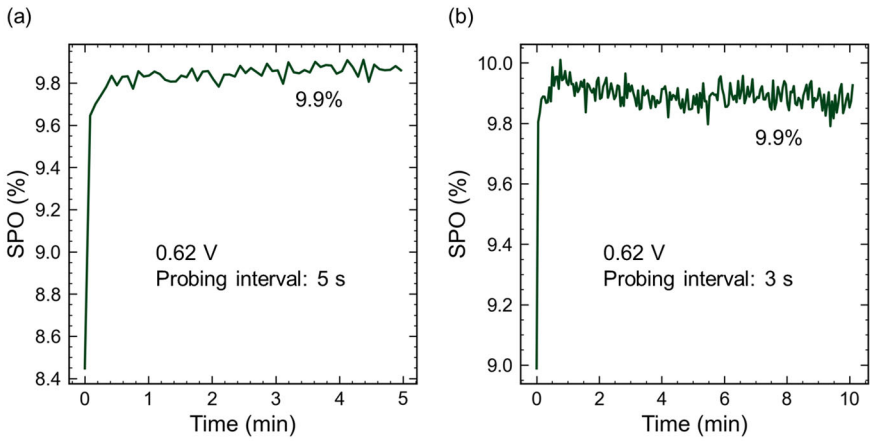

Figure 50. Stabilized power output (SPO) of $FA_{1-x}MA_xPbI_3$ devices from dep2_dep2_D4, with (a) 5 minutes current probing time and 5 seconds interval and (b) 10 minutes current probing time and 3 seconds interval. The applied voltage is 0.62 V, determined by the maximum power point (MPP) from current density–voltage characteristics under 1 sun illumination.

batch of transport layers and gold electrode as used in day1. For all $FA_{1-x}MA_xPbI_3$ devices, EQE onsets are all red-shift to ~820 nm as compared to the $MAPbI_3$ device (~800 nm) as shown in Figure 48a, consistent with FA incorporation. To further understand the current loss in the device, reflection (R) of the device (from the ITO substrate side) was measured (Figure 48b). In 600~800 nm range, the shape of EQE spectra follows the tread of (1-R). The decrease in this range can be improved by increasing perovskite layer thickness and is mainly due to the interference of perovskite layer.[35] The composition of $FA_{1-x}MA_xPbI_3$ devices from day1 is also characterized by XRD after the device testing is finished (Figure 49). The gold electrode was peeled off before doing the XRD. A point source XRD was used and focused on the actual device pixels. Dep1 is stoichiometric $FA_{1-x}MA_xPbI_3$ without any PbI_2 excess and dep2 is $FA_{1-x}MA_xPbI_3$ with some PbI_2 excess. Not much difference is observed from pixel-to-pixel based on the composition. This result also suggests that some degree of excess PbI_2 is needed to get better performance devices, similar to what we found with $MAPbI_3$.

Stabilized power output (SPO) was performed on day2_dep2_D4 device. The applied voltage is 0.62 V, determined by the maximum power point (MPP) from J-V characteristics under 1 sun illumination. This device demonstrated a stable PCE of 9.9%, regardless of total scan time and probing interval differences (Figure 50). This result is promising for future work in this area on VTD device stability, but ultimately does not complete Milestone 2.6.3.

As noted in Section 7.1, the original VTD system in MIT was re-designed. Figure 1b shows a schematic of the new system, and the results presented in Figures 51-53 were obtained using this new design. As a complementary approach to all-vapor perovskite deposition, we also explored a hybrid-two-step technique outlined in Figure 51. The first step of the process – the PbI_2 film – is deposited by VTD, to avoid use of hazardous solvents. Similar to all-solution-two-step, a 0.3M organics solution in IPA (lower concentration compared to all-solution-2-step process) is dropped on top of the PbI_2 layer. Incorporation of these films into devices resulted in a few working pixels with a champion device of 6.9% efficiency (Figure 52a). Similar to the film phase analysis, the

XRD data of the devices shown in Figure 52b suggest that the hybrid film has the perovskite phase, but no excess of PbI_2.

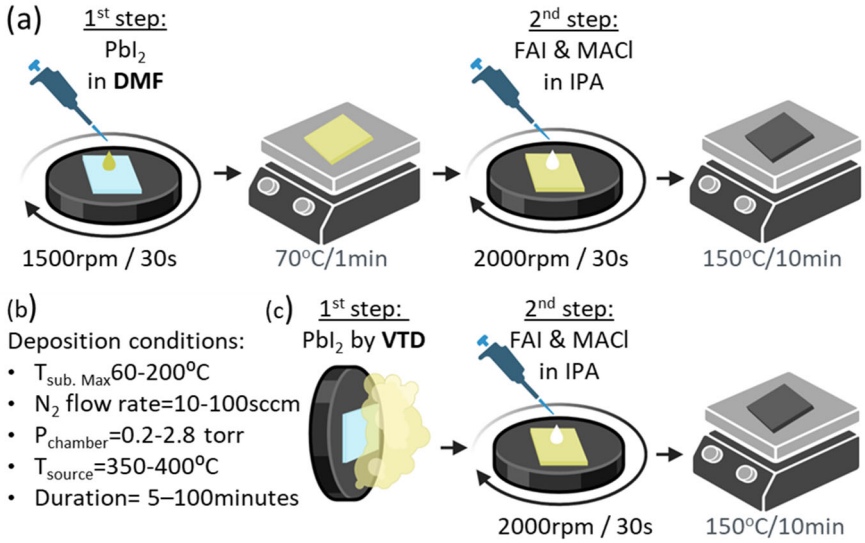

Figure 51: *a) Two-step-all-solution process, to fabricate $FAPbI_3$ films. Lead iodide solution in DMF/DMSO is dropped on the substrate, to form a yellow film. The film is dried in 70°C for 1 minute. Then, the film is treated with a solution of the organic salts formamidinium iodide and methylammonium chloride in IPA. The solution is dropped on the spinning substrate and reacts with the PbI_2 under-layer to form the dark (alpha) perovskite phase. b) Deposition conditions of the first step of the hybrid process. c) Two-step-hybrid process, for $FAPbI_3$ films fabrication. Lead iodide powder is sublimed in a tube furnace and carried by nitrogen towards a cooled substrate in mild vacuum. A lead iodide film is formed. Then, the film is treated with a solution of the organic salts formamidinium iodide and methylammonium chloride in IPA. The solution is dropped on the spinning substrate and reacts with the PbI_2 under-layer to form the dark (alpha) perovskite phase.*

We studied also the effect of A-site solution concentration on the formed phase and found that the solution required to convert the VTD-PbI_2 layer to the perovskite phase is significantly more dilute than the one used on solution processed PbI_2 film. Figure 53

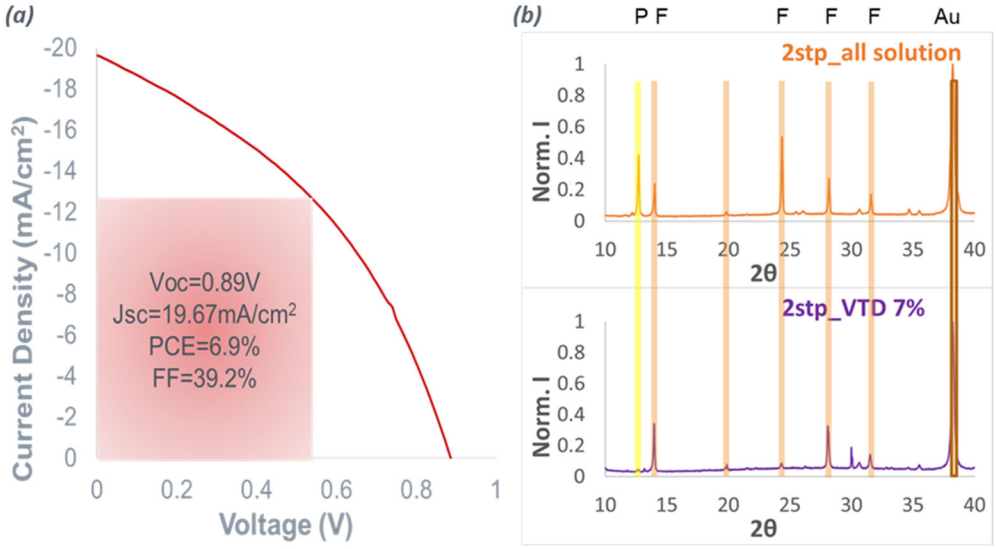

Figure 52: *a) JV plot of the first working hybrid- two-step device. b) XRD patterns of two-step devices, processed by all-solution (top) and hybrid (bottom) techniques.*

depicts two XRD patterns taken on hybrid films, processed with vapor deposited lead iodide layer and different A-site solution concentrations. A typical perovskite (α-$FAPbI_3$) pattern was acquired from the film treated by an A-site solution of 0.3M (similar patterns were demonstrated before for solution-processed perovskite films). However, the concentrated (0.8M) solution yields a different pattern. The peak at 2theta~9.9 is indicative of the presence of the byproducts ammonium lead iodide and ammonium lead iodide dihydrate (NH_4PbI_3 and $NH_4PbI_3•H_2O$). This can be the result of "over-treating" the lead iodide underlayer and shifting the stoichiometry such that the perovskite phase is no longer stable.[36]

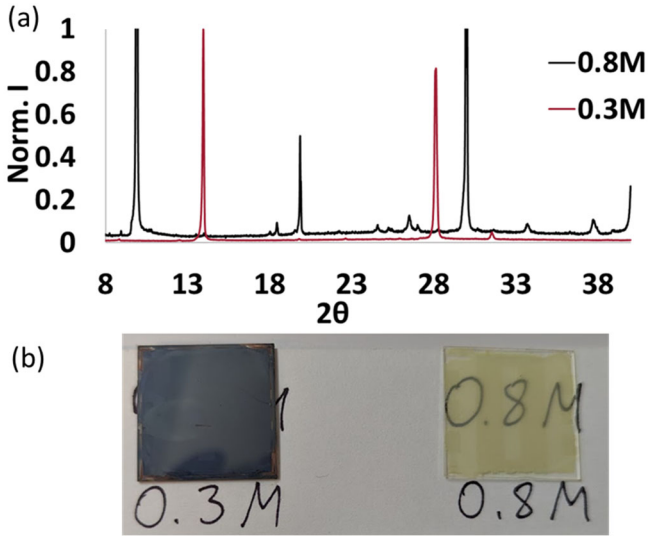

Figure 53: *a) X-ray diffraction patterns of two VTD-PbI_2 films after treatment with different concentrations of organic salts solutions. b) Solution concentration of 0.8M yields a translucent-yellow phase. Too high A-site cation concentration "over-treats" the lead iodide layer, pushing it to a non-perovskite phase.*

SEM images of both lead iodide films shed light on the source of this difference, revealing that the solution-processed film is denser, whereas the vapor-processed film has a significantly higher surface area. The A-site solution reacts more easily on the surface and the reaction is not limited by diffusion through the dense lead iodide grains. After A-site treatment with the optimal concentration to each processing technique (0.8M for solution based and 0.3M for vapor-based), both PbI_2 films react to for the perovskite phase with a similar microstructure.

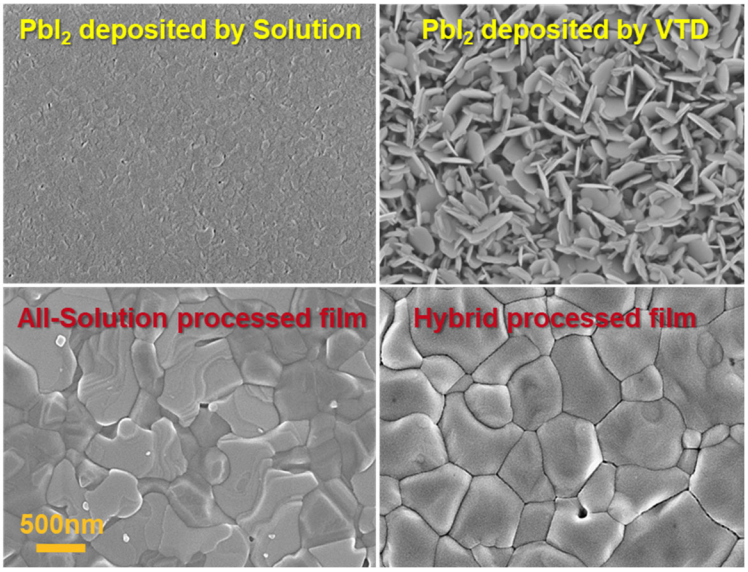

Figure 54: *SEM images of lead iodide films on FTO. PbI_2 films by VTD are composed of crystallites; Hybrid Perovskite films have pores inside the grains; All-solution Perovskite films are PbI_2 excessive, have more faceted grain structure and porosity along grain boundaries.*

Improvements to the deposition system enabled cooling and rotating the substrate for a faster and more uniform deposition. With these new improvements we reached deposition rates of up to 250 nm/minute, when the substrate is kept under 60°C, source temperature is 355°C, nitrogen

flow rate through the source is 50 sccm, chamber pressure is 0.45 torr and the deposition zone is kept at 300°C. Under these conditions, we obtained consistently 7% to 12% efficient devices (Figure 55), still significantly lower than all-solution-two-step processed devices, which show efficiencies between 15 and 19% with a champion device of 19.9%.

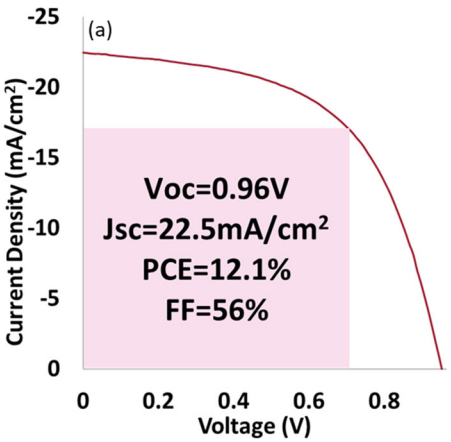

Figure 55: *JV plot of the champion hybrid processed device under 1 sun illumination.*

7.4 References

(1) Das, B.; Liu, Z.; Aguilera, I.; Rau, U.; Kirchartz, T. Defect Tolerant Device Geometries for Lead-Halide Perovskites. *Mater. Adv.* **2021**, *2* (11), 3655–3670. https://doi.org/10.1039/D0MA00902D.
(2) Sutherland, B. R.; Sargent, E. H. Perovskite Photonic Sources. *Nat. Photonics* **2016**, *10* (5), 295–302. https://doi.org/10.1038/nphoton.2016.62.
(3) Swartwout, R.; Hoerantner, M. T.; Bulović, V. Scalable Deposition Methods for Large-area Production of Perovskite Thin Films. *ENERGY Environ. Mater.* **2019**, *2* (2), 119–145. https://doi.org/10.1002/eem2.12043.
(4) NREL. Best Research Cell Efficiency Chart. https://www.nrel.gov/pv/cell-efficiency.html.
(5) Swartwout, R.; Patidar, R.; Belliveau, E.; Dou, B.; Beynon, D.; Greenwood, P.; Moody, N.; deQuilettes, D.; Bawendi, M.; Watson, T.; Bulovic, V. Predicting Low Toxicity and Scalable Solvent Systems for High-Speed Roll-to-Roll Perovskite Manufacturing. *Sol. RRL* **2022**, *6* (3), 2100567. https://doi.org/10.1002/solr.202100567.
(6) Clark, C. P.; Mann, J. E.; Bangsund, J. S.; Hsu, W.-J.; Aydil, E. S.; Holmes, R. J. Formation of Stable Metal Halide Perovskite/Perovskite Heterojunctions. *ACS Energy Lett.* **2020**, *5* (11), 3443–3451. https://doi.org/10.1021/acsenergylett.0c01609.
(7) Ávila, J.; Momblona, C.; Boix, P. P.; Sessolo, M.; Bolink, H. J. Vapor-Deposited Perovskites: The Route to High-Performance Solar Cell Production? *Joule* **2017**, *1* (3), 431–442. https://doi.org/10.1016/j.joule.2017.07.014.
(8) Gil-Escrig, L.; Dreessen, C.; Kaya, I. C.; Kim, B.-S.; Palazon, F.; Sessolo, M.; Bolink, H. J. Efficient Vacuum-Deposited Perovskite Solar Cells with Stable Cubic $FA_{1-x}MA_xPbI_3$. *ACS Energy Lett.* **2020**, *5* (9), 3053–3061. https://doi.org/10.1021/acsenergylett.0c01473.
(9) Guesnay, Q.; Sahli, F.; Ballif, C.; Jeangros, Q. Vapor Deposition of Metal Halide Perovskite Thin Films: Process Control Strategies to Shape Layer Properties. *APL Mater.* **2021**, *9* (10), 100703. https://doi.org/10.1063/5.0060642.
(10) Hoerantner, M. T.; Wassweiler, E. L.; Zhang, H.; Panda, A.; Nasilowski, M.; Osherov, A.; Swartwout, R.; Driscoll, A. E.; Moody, N. S.; Bawendi, M. G.; Jensen, K. F.; Bulović, V. High-Speed Vapor Transport Deposition of Perovskite Thin Films. *ACS Appl. Mater. Interfaces* **2019**, *11* (36), 32928–32936. https://doi.org/10.1021/acsami.9b07651.
(11) Clark, C. P.; Voigt, B.; Aydil, E. S.; Holmes, R. J. Carrier-Gas Assisted Vapor Deposition for Highly Tunable Morphology of Halide Perovskite Thin Films. *Sustain. Energy Fuels* **2019**, *3* (9), 2447–2455. https://doi.org/10.1039/C9SE00200F.
(12) Kim, B.-S.; Gil-Escrig, L.; Sessolo, M.; Bolink, H. J. Deposition Kinetics and Compositional Control of Vacuum-Processed $CH_3NH_3PbI_3$ Perovskite. *J. Phys. Chem. Lett.* **2020**, *11* (16), 6852–6859. https://doi.org/10.1021/acs.jpclett.0c01995.
(13) Tavakoli, M. M.; Gu, L.; Gao, Y.; Reckmeier, C.; He, J.; Rogach, A. L.; Yao, Y.; Fan, Z. Fabrication of Efficient Planar Perovskite Solar Cells Using a One-Step Chemical Vapor Deposition Method. *Sci. Rep.* **2015**, *5* (1), 14083. https://doi.org/10.1038/srep14083.

(14) Sahli, F.; Miaz, N.; Salsi, N.; Bucher, C.; Schafflützel, A.; Guesnay, Q.; Duchêne, L.; Niesen, B.; Ballif, C.; Jeangros, Q. Vapor Transport Deposition of Methylammonium Iodide for Perovskite Solar Cells. *ACS Appl. Energy Mater.* **2021**, *4* (5), 4333–4343. https://doi.org/10.1021/acsaem.0c02999.
(15) Leyden, M. R.; Lee, M. V.; Raga, S. R.; Qi, Y. Large Formamidinium Lead Trihalide Perovskite Solar Cells Using Chemical Vapor Deposition with High Reproducibility and Tunable Chlorine Concentrations. *J. Mater. Chem. A* **2015**, *3* (31), 16097–16103. https://doi.org/10.1039/C5TA03577E.
(16) Moser, T.; Artuk, K.; Jiang, Y.; Feurer, T.; Gilshtein, E.; Tiwari, A. N.; Fu, F. Revealing the Perovskite Formation Kinetics during Chemical Vapour Deposition. *J. Mater. Chem. A* **2020**, *8* (42), 21973–21982. https://doi.org/10.1039/D0TA04501B.
(17) Hsu, W.-J.; Pettit, E. C.; Swartwout, R.; Kadosh, T. Z.; Srinivasan, S.; Wassweiler, E. L.; Haugstad, G.; Bulović, V.; Holmes, R. J. Efficient Metal-Halide Perovskite Photovoltaic Cells Deposited via Vapor Transport Deposition. *Sol. RRL* **2023**, 2300758. https://doi.org/10.1002/solr.202300758.
(18) Wassweiler, E.; Panda, A.; Kadosh, T.; Nguyen, T.; Hsu, W.-J.; Pettit, E.; Holmes, R. J.; Tuller, H.; Bulovic, V. Design of a Custom Vapor Transport Co-Deposition System for Scalable Production of Perovskite Solar Cells. *J. Vac. Sci. Technol. A* **2023**, *41* (5), 052801. https://doi.org/10.1116/6.0002668.
(19) Shtein, M.; Gossenberger, H. F.; Benziger, J. B.; Forrest, S. R. Material Transport Regimes and Mechanisms for Growth of Molecular Organic Thin Films Using Low-Pressure Organic Vapor Phase Deposition. *J. Appl. Phys.* **2001**, *89* (2), 1470–1476. https://doi.org/10.1063/1.1332419.
(20) Hsu, W.-J.; Wassweiler, E. L.; Pettit, E. C.; Bulović, V.; Holmes, R. J. Numerical Design Considerations for Vapor Transport Deposition of Metal-Halide Perovskite Thin Films. *Appl. Phys. Lett.* **submitted**.
(21) Pettit, E. C.; Hsu, W.-J.; Garcia-Barriocanal, J.; Srinivasan, S.; Kadosh, T. Z.; Bulović, V.; Holmes, R. J. Controlling Preferred Grain Orientation in Vapor Deposited Metal-Halide Perovskite Films. *J. Phys. Chem. C* **submitted**.
(22) Lohmann, K. B.; Patel, J. B.; Rothmann, M. U.; Xia, C. Q.; Oliver, R. D. J.; Herz, L. M.; Snaith, H. J.; Johnston, M. B. Control over Crystal Size in Vapor Deposited Metal-Halide Perovskite Films. *ACS Energy Lett.* **2020**, *5* (3), 710–717. https://doi.org/10.1021/acsenergylett.0c00183.
(23) Plummer, J. D.; Deal, M.; Griffin, P. B. *Silicon VLSI Technology: Fundamentals, Practice and Modeling*, 1st ed.; Prentice Hall Inc, 2000.
(24) Euvrard, J.; Gunawan, O.; Mitzi, D. B. Impact of PbI_2 Passivation and Grain Size Engineering in $CH_3NH_3PbI_3$ Solar Absorbers as Revealed by Carrier-Resolved Photo-Hall Technique. *Adv. Energy Mater.* **2019**, *9* (47), 1902706. https://doi.org/10.1002/aenm.201902706.
(25) Roose, B.; Dey, K.; Chiang, Y.-H.; Friend, R. H.; Stranks, S. D. Critical Assessment of the Use of Excess Lead Iodide in Lead Halide Perovskite Solar Cells. *J. Phys. Chem. Lett.* **2020**, *11* (16), 6505–6512. https://doi.org/10.1021/acs.jpclett.0c01820.
(26) Momblona, C.; Malinkiewicz, O.; Roldán-Carmona, C.; Soriano, A.; Gil-Escrig, L.; Bandiello, E.; Scheepers, M.; Edri, E.; Bolink, H. J. Efficient Methylammonium Lead

Iodide Perovskite Solar Cells with Active Layers from 300 to 900 Nm. *APL Mater.* **2014**, *2* (8), 081504. https://doi.org/10.1063/1.4890056.
(27) Jacobsson, T. J.; Correa-Baena, J.-P.; Halvani Anaraki, E.; Philippe, B.; Stranks, S. D.; Bouduban, M. E. F.; Tress, W.; Schenk, K.; Teuscher, J.; Moser, J.-E.; Rensmo, H.; Hagfeldt, A. Unreacted PbI $_2$ as a Double-Edged Sword for Enhancing the Performance of Perovskite Solar Cells. *J. Am. Chem. Soc.* **2016**, *138* (32), 10331–10343. https://doi.org/10.1021/jacs.6b06320.
(28) Tumen-Ulzii, G.; Qin, C.; Klotz, D.; Leyden, M. R.; Wang, P.; Auffray, M.; Fujihara, T.; Matsushima, T.; Lee, J.; Lee, S.; Yang, Y.; Adachi, C. Detrimental Effect of Unreacted PbI_2 on the Long-Term Stability of Perovskite Solar Cells. *Adv. Mater.* **2020**, *32* (16), 1905035. https://doi.org/10.1002/adma.201905035.
(29) Nukunudompanich, M.; Budiutama, G.; Suzuki, K.; Hasegawa, K.; Ihara, M. Dominant Effect of the Grain Size of the MAPbI $_3$ Perovskite Controlled by the Surface Roughness of TiO $_2$ on the Performance of Perovskite Solar Cells. *CrystEngComm* **2020**, *22* (16), 2718–2727. https://doi.org/10.1039/D0CE00169D.
(30) Li, F.; Chen, C.; Tan, F.; Li, C.; Yue, G.; Shen, L.; Zhang, W. Semitransparent Inverted Polymer Solar Cells Employing a Sol-Gel-Derived TiO2 Electron-Selective Layer on FTO and MoO3/Ag/MoO3 Transparent Electrode. *Nanoscale Res. Lett.* **2014**, *9* (1), 579. https://doi.org/10.1186/1556-276X-9-579.
(31) Saive, R. S-Shaped Current–Voltage Characteristics in Solar Cells: A Review. *IEEE J. Photovolt.* **2019**, *9* (6), 1477–1484. https://doi.org/10.1109/JPHOTOV.2019.2930409.
(32) Guo, H.; Zhang, H.; Yang, J.; Chen, H.; Li, Y.; Wang, L.; Niu, X. TiO_2 /SnO_2 Nanocomposites as Electron Transporting Layer for Efficiency Enhancement in Planar CH_3 NH_3 PbI_3 -Based Perovskite Solar Cells. *ACS Appl. Energy Mater.* **2018**, *1* (12), 6936–6944. https://doi.org/10.1021/acsaem.8b01331.
(33) Chen, Q.; Zhou, H.; Song, T.-B.; Luo, S.; Hong, Z.; Duan, H.-S.; Dou, L.; Liu, Y.; Yang, Y. Controllable Self-Induced Passivation of Hybrid Lead Iodide Perovskites toward High Performance Solar Cells. *Nano Lett.* **2014**, *14* (7), 4158–4163. https://doi.org/10.1021/nl501838y.
(34) Cao, D. H.; Stoumpos, C. C.; Malliakas, C. D.; Katz, M. J.; Farha, O. K.; Hupp, J. T.; Kanatzidis, M. G. Remnant PbI2, an Unforeseen Necessity in High-Efficiency Hybrid Perovskite-Based Solar Cells? *APL Mater.* **2014**, *2* (9), 091101. https://doi.org/10.1063/1.4895038.
(35) Mercaldo, L. V.; Bobeico, E.; De Maria, A.; Della Noce, M.; Ferrara, M.; Lancellotti, L.; Romano, A.; Sannino, G. V.; Nasti, G.; Abate, A.; Delli Veneri, P. Procedure Based on External Quantum Efficiency for Reliable Characterization of Perovskite Solar Cells. *Energy Technol.* **2022**, *10* (10), 2200748. https://doi.org/10.1002/ente.202200748.
(36) Van Gompel, W. T. M.; Herckens, R.; Reekmans, G.; Ruttens, B.; D'Haen, J.; Adriaensens, P.; Lutsen, L.; Vanderzande, D. Degradation of the Formamidinium Cation and the Quantification of the Formamidinium–Methylammonium Ratio in Lead Iodide Hybrid Perovskites by Nuclear Magnetic Resonance Spectroscopy. *J. Phys. Chem. C* **2018**, *122* (8), 4117–4124. https://doi.org/10.1021/acs.jpcc.7b09805.

8. Significant Accomplishments and Conclusions:

This project sought to bring a systematic and quantitative analysis to the processing of metal-halide perovskites via VTD and demonstrate efficient PVs processed using this method. The project has been successful on both fronts, offering insight into the processing and design parameters that impact rate and uniformity in VTD, as well as the role of substrate and processing conditions in film morphology. In addition, this project was successful in demonstrating efficiency solar cells based on $MAPbI_3$ with efficiency comparable to solution-processed devices prepared in parallel. At the conclusion of BP1, a decision was made to revise the SOPO to shift focus away from defect passivation and instead on the realization of alternate perovskite chemistries. Specifically, the project demonstrated the ability to use VTD to successfully process FA-based, multi-cation perovskites, realizing promising device efficiencies. In parallel, the project has also demonstrated a hybrid processing approach using VTD to process the metal-halide and a reduced toxicity solution process to process the organo-halides to sequentially form the perovskites, also leading to high device efficiency. Taken together, the project has been successful in de-risking the use of VTD for future industrial processes by clearly demonstrating a path to the processing of quality material and devices.

9. Path Forward:

Future research in this area should focus on thoroughly understanding the stability of devices processed via VTD. In this project, emphasis was placed on engineering composition to demonstrate efficient devices, and there was insufficient opportunity to investigate stability. The impact, for example, of the organo-halide traveling through a furnace hot zone on device stability is important to assess. Separately, this project touched on the use of post-process treatments commonly applied to solution-processed devices on those processed using VTD however, there was again insufficient opportunity to pursue this question in detail. Understanding the potential portability of these treatments is important in order to establish the extent of new knowledge that could need to be developed to address defects in VTD processed films. These, combined with further increasing device efficiency via additional material compositions will help to enable commercialization of devices processed via VTD, and allow emphasis to shift on reactor design and best integration practices into existing fabrication facilities.

Additionally, further optimization and understanding of the device stack would likely be beneficial to improving device efficiency. The device architectures used in this work were based on solution processed architectures that led to high efficiency. However, given some of the unique features of VTD processed films, additional work should be done to confirm that the energy level alignment of the VTD processed perovskite with the transport layers selected is optimized for good charge carrier extraction. The fill factor of both VTD and hybrid processed devices is low compared to the literature, and this may be due to unoptimized contact between the perovskite active layer and the transport layers. Further study of the pixel-to-pixel and run-to-run variation observed mixed A-site

$FA_{(1-x)}MA_xPbI_3$ films would also be valuable, as preventing this phenomenon is key to scaling up the VTD technique.

10. Products:

To date, the project has led to five papers and one conference proceeding that are either published or under review. At least two additional manuscripts will be submitted after the conclusion of the project. The project has also led to 21 conference or meeting presentations for funded graduate students. In terms of awards, two students were selected to attend the DOE/NREL Hand-On PV Experience (HOPE) and one was selected to attend the ACS Green Chemistry Institute Summer School. In addition, one student was awarded a UMN Institute on the Environment Commercialization Fellowship. The project allowed deeper relationships to be built between the PIs and relevant companies (First Solar and Swift Solar) as well as with NREL. The following table details the specific products of this work:

Article Title	**Author(s)** (format: FirstName LastName)	**Journal Name**	**Volume and Page Number**	**Status** (planned, in development, submitted, accepted, published)
Design of a Custom Vapor Transport Co-Deposition System for Scalable Production of Perovskite Solar Cells	Ella Wassweiler, Anurag Panda, Tamar Kadosh, Thienan Nguyen, Wan-Ju Hsu, Emma Pettit, Russell J. Holmes, Harry Tuller, Vladimir Bulovic	*Journal of Vacuum Science and Technology A*	*41, 052801*	*published*
Efficient Metal-Halide Perovskite Photovoltaic Cells Deposited via Vapor Transport Deposition	Wan-Ju Hsu, Emma C. Pettit, Richard Swartwout, Tamar Kadosh, Shreyas Srinivasan. Ella Wassweiler, Vladimir Bulović, and Russell J. Holmes	*Solar RRL*	8, 2300758	*published*
Vapor transport deposition of metal-halide perovskites solar cells	Wan-Ju Hsu, Emma C Pettit, Richard Swartwout, Tamar Kadosh, Shreyas Srinivasan, Ella L Wassweiler, Vladimir Bulovic, Russell J Holmes	*Proc. SPIE, Organic, Hybrid, and Perovskite Photovoltaics XXIV*	Proceedings Volume 12660, 1266007	*published*
Influence of co-deposition on methylammonium iodide degradation during vapor transport deposition	Ella L. Wassweiler, Tamar Kadosh, Deepta Gupta, Thienan Nguyen, Wan-Ju Hsu, Emma Pettit, Russell J. Holmes, Harry Tuller, Vladimir Bulovic	*The Journal of Physical Chemistry C*	127, 24626-24632	*published*
Controlling Preferred Grain Orientation in Vapor Deposited Metal-Halide Perovskite Films	Emma C. Pettit, Wan-Ju Hsu, Javier Garcia-Barriocanal, Shreyas Srinivasan, Tamar Kadosh, Vladimir Bulovic, Russell J Holmes	*The Journal of Physical Chemistry C*		*In-revision*
Numerical Design Considerations for Vapor Transport Deposition of Metal-Halide Perovskite Thin Films	Wan-Ju Hsu, Ella L Wassweiler, Emma C Pettit, Vladimir Bulovic, Russell J Holmes	*Applied Physics Letters*		*In-revision*

Presentation, Paper Title	Author/Speaker	Conference Name	Conference Product Type	Conference Date
Vapor-Processing of Metal-Halide Perovskites for Photovoltaics and Optoelectronics	Wan-Ju Hsu	UMN Industrial Partnership for Research in Interfacial and Materials Engineering (IPRIME) Annual Meeting	presentation	8/4/2021
Vapor-Processing of Metal Halide Perovskite Thin Films and Solar Cells	Wan-Ju Hsu	American Vacuum Society MN Chapter Fall Symposium	presentation	9/15/2021
Modeling Vapor Transport Deposition of Metal-halide Perovskite Thin Films for Photovoltaic and Optoelectronic Devices	Wan-Ju Hsu	Minnesota Supercomputing Institute 2022 Research Exhibition	presentation	4/26/2022
Material Reservoir Design for Controlled Vacuum Deposition of High-Temperature and Reactive Precursor Materials	Ella Wassweiler	2022 Society of Vacuum Coaters Spring Conference	presentation	5/2/2022
Vapor Transport Deposition of Metal Halide Perovskites for Photovoltaics	Wan-Ju Hsu	12th DOE/NREL Hands-On PV Experience (HOPE)	presentation	7/18/2022
Vapor Transport Deposition of Metal Halide Perovskites for Photovoltaics	Emma Pettit	UMN Industrial Partnership for Research in Interfacial and Materials Engineering (IPRIME) Annual Meeting	presentation	6/1/2022
Vapor Transport Co-Deposition of Perovskite Photovoltaics	Tamar Kadosh Zhitomirsky	2022 Materials Research Society (MRS) Fall Meeting & Exhibit	presentation	11/28/2022
Vapor Transport Co-Deposition of Perovskite Photovoltaics	Tamar Kadosh Zhitomirsky	MARC2023 (Microsystems Annual Research Conference)	presentation	1/25/2023
Vapor Transport Deposition of Metal Halide Perovskites for Photovoltaics	Emma Pettit	American Physical Society March Meeting 2023	presentation	3/8/2023
Vapor Transport Deposition of Efficient Metal-Halide Perovskite Photovoltaic Cells	Emma Pettit	13th DOE/NREL Hands-On PV Experience (HOPE)	presentation	
Efficient Metal-Halide Perovskite Photovoltaic Cells Deposited via Vapor Transport Deposition	Wan-Ju Hsu	SPIE Optics + Photonics 2023	presentation	08/20/23-08/24/23
Directed Texturing of Metal-Halide Perovskite Films via Vapor Transport Deposition	Emma Pettit	American Physical Society March Meeting 2024	presentation	3/6/2024
Simulation of Vapor Transport Deposition for Metal-Halide Perovskite Thin Films	Wan-Ju Hsu	American Physical Society March Meeting 2024	presentation	3/5/2024
Variations in Carrier Mobility in Metal-Halide Perovskite	James Heyman	American Physical Society March Meeting 2024	presentation	03/03/24-03/08/24

Thin Fims with Film Stoichiometry				
Optimized Design of Vapor Transport Co-deposited Perovskite Photovoltaics	Tamar Kadosh Zhitomirsky	Microsystems Annual Research Conference	presentation	01/23/24-01/24/24
Realizing Diverse Materials Chemistries for Perovskite Photovoltaics through Vapor Processing	Emma Pettit	UMN Industrial Partnership for Research in Interfacial and Materials Engineering (IPRIME) Annual Meeting	presentation	5/29/2024
The Role of Processing on Preferred Orientation in Metal Halide Perovskite Films	Emma Pettit	UMN Industrial Partnership for Research in Interfacial and Materials Engineering (IPRIME) Annual Meeting	presentation	5/29/2024
Metal-halide Perovskite Photovoltaics and a Role for Vapor Processing	Wan-Ju Hsu	UMN Industrial Partnership for Research in Interfacial and Materials Engineering (IPRIME) Annual Meeting	presentation	5/29/2024
Formation of Phase-Pure α-FAPbI3 Perovskite via Vapor Transport Deposition	Wan-Ju Hsu	UMN Industrial Partnership for Research in Interfacial and Materials Engineering (IPRIME) Annual Meeting	presentation	5/29/2024
Vapor Transport Deposition of Efficient Metal-Halide Perovskite Photovoltaic Cells	Emma Pettit	ACS Green Chemistry Institute Summer School	presentation	6/22/2024
Vapor Based Process for Safe and Scalable Perovskite Photovoltaics Fabrication	Tamar Kadosh Zhitomirsky	2024 Materials Research Society (MRS) Fall Meeting & Exhibit	presentation	12/5/2024

11. Project Team and Roles:

The project team has consisted of researchers at both UMN and MIT. At UMN, graduate students Wan-Ju Hsu and Emma Pettit have been supervised by Prof. Russell J. Holmes (Project Lead). At MIT, Ella Wassweiler, Tamar Kadosh, and Shreyas Srinivasan have been supervised by Prof. Vladimir Bulović. Both Wan-Ju Hsu and Ella Wassweiler have graduated while supported by the project and now work at Lam Research and First Solar, respectively.